ISTANBUL TECHNICAL UNIVERSITY ★ GRADUATE SCHOOL

IMPROVING THE PERFORMANCE OF REMOTE SENSING-BASED WATER BUDGET COMPONENTS ACROSS MID- AND SMALL- SCALE BASINS

Ph.D. THESIS

Gökhan KAYAN

Department of Geomatics Engineering

Geomatics Engineering Programme

JULY 2022

ISTANBUL TECHNICAL UNIVERSITY ★ GRADUATE SCHOOL

IMPROVING THE PERFORMANCE OF REMOTE SENSING-BASED WATER BUDGET COMPONENTS ACROSS MID- AND SMALL- SCALE BASINS

Ph.D. THESIS

Gökhan KAYAN
(501152601)

Department of Geomatics Engineering

Geomatics Engineering Programme

Thesis Advisor: Assoc. Prof. Dr. Esra ERTEN
Eş Danışman: Prof. Dr. Umut TÜRKER

JULY 2022

İSTANBUL TEKNİK ÜNİVERSİTESİ ★ LİSANSÜSTÜ EĞİTİM ENSTİTÜSÜ

KÜÇÜK VE ORTA ÖLÇEKLİ HAVZALARDA UZAKTAN ALGILAMA TABANLI SU BÜTÇESİ DEĞİŞKENLERİNİN İYİLEŞTİRİLMESİ

DOKTORA TEZİ

Gökhan KAYAN
(501152601)

Geomatik Mühendisliği Anabilim Dalı

Geomatik Mühendisliği Programı

Tez Danışmanı: Assoc. Prof. Dr. Esra ERTEN
Eş Danışman: Prof. Dr. Umut TÜRKER

TEMMUZ 2022

Gökhan KAYAN, a Ph.D. student of ITU Graduate School student ID 501152601 successfully defended the thesis entitled “IMPROVING THE PERFORMANCE OF REMOTE SENSING-BASED WATER BUDGET COMPONENTS ACROSS MID- AND SMALL- SCALE BASINS”, which he prepared after fulfilling the requirements specified in the associated legislations, before the jury whose signatures are below.

Thesis Advisor :	**Assoc. Prof. Dr. Esra ERTEN** Istanbul Technical University	....
Co-advisor :	**Prof. Dr. Umut TÜRKER** Eastern Mediterranean University	....
Jury Members :	**Prof. Dr. Orhan AKYILMAZ** Istanbul Technical University	....
	Prof. Dr. Oral YAĞCI Istanbul Technical University	....
	Prof. Dr. Füsun BALIK ŞANLI Yıldız Technical University	....
	Prof. Dr. Ayşe Gül Tanık Istanbul Technical University	....
	Asst. Prof. Dr. Dilek Eren Akyüz Istanbul University - Cerrahpaşa	....

Date of Submission : **20 June 2022**
Date of Defense : **19 July 2022**

To my family and beloved dog,

FOREWORD

Patience is a key element of success. Despite being pessimistic at times when I did not achieve good results, I never gave up on this route with the help of my family and the encouragement of my supervisors.

First of all, I would like to express my deep sense of thanks and gratitude to my supervisor, Assoc. Prof. Dr. Esra ERTEN, and my co-supervisor, Prof. Dr. Umut TÜRKER for their unlimited support and guidance for my Ph.D. thesis. They always responded immediately to all of my questions, regardless of the time. I am grateful for the invaluable experience they have shared with me in helping me to draw my route to being an independent academician.

Besides my supervisors, I would like to thank my jury members: Prof. Dr. Orhan AKYILMAZ, Prof. Dr. Oral YAĞCI, and Prof. Dr. Füsun Balık ŞANLI for their significant contributions in advancing the thesis to end stage. Their valuable comments paved the way for my thesis work.

Also, I would like to thank the State Hydraulic Works of Turkey, the Turkish State Meteorological Service, the Norther Cyprus Meteorological Department, the Jet Propulsion Laboratory, the National Aeronautics and Space Administration, the Japan Aerospace Exploration Agency, the United States Geological Survey, the Climate Hazards Center, the Climate Prediction Center, and the University of California for providing data for this work.

Finally, I would like to thank my family for their invaluable support throughout my entire life.

June 2022

Gökhan KAYAN
(Civil Engineer)

TABLE OF CONTENTS

ABBREVIATIONS

BC	: Bias-corrected
CC	: Correlation Coefficient
CCD	: Cold Cloud Duration
CHIRPS	: Climate Hazards Group Infrared Precipitation with Station data
CKF	: Constrained Kalman Filter
CMORPH	: Climate Prediction Center Morphing
CN	: Curve Number
CPC	: Climate Prediction Center
CRU	: Climatic Research Unit
CSR	: Center for Space Research at University of Texas
DEM	: Digital Elevation Model
ERA	: ECMWF Re-Analysis
FLR	: Fuzzy Linear Regression
GFZ	: Geoforschungs Zentrum Potsdam
GIS	: Geographic Information Systems
GLDAS	: Global Land Data Assimilation System
GLEAM	: Global Land Evaporation Amsterdam Model
GPCC	: Global Precipitation Climatology Centre
GPCP	: Global Precipitation Climatology Project
GPM	: Global Precipitation Measurement
GRACE	: Gravity Recovery and Climate Experiment
GSMaP	: Global Satellite Mapping of Precipitation
GTCH	: Generalized Three-Cornered Hat
IDW	: Inverse Distance Weighted
IMERG	: Integrated Multi-Satellite Retrievals for GPM
IQR	: Interquartile Range
IR	: Infrared
JMF	: Joint Membership Function
JPL	: Jet Propulsion Laboratory
KGE	: Kling-Gupta Efficiency
LSM	: Land Surface Model
MASCON	: Mass Concentration
MAE	: Mean Absolute Error
MODIS	: Moderate Resolution Imaging Spectroradiometer
MON	: University of Montana
MPI	: Max Planck Institute
MSWEP	: Multi-Source Weighted-Ensemble Precipitation
MW	: Microwave

NDVI	:	Normalized Difference Vegetation Index
NOAH	:	Neural Optimization Applied Hydrology
NTSG	:	Numerical Terradynamic Simulation Group
PBIAS	:	Percent Bias
PERSIANN	:	Precipitation Estimation from Remotely Sensed Information using Artificial Neural Networks
PM	:	Penman-Monteith
PMW	:	Passive Microwave
PRI	:	Princeton University
PT	:	Priestly-Taylor
RMSD	:	Root Mean Square Deviation
RMSE	:	Root Mean Square Error
RS	:	Remote Sensing
SCS	:	Soil Conservation Service
SEBS	:	Surface Energy Balance System
SH	:	Spherical Harmonics
SWOT	:	Surface Water and Ocean Topography
TC	:	Triple Collocation
TRMM	:	Tropical Rainfall Measuring Mission
VIC	:	Variable Infiltration Capacity
UNESCO	:	United Nations Educational, Scientific and Cultural Organization
USA	:	University of California, Santa Barbara
USGS	:	United States Geological Survey
WB	:	Water Budget
WEAP-PGM	:	Water Evaluation and Planning System — Plant Growth Model
WM	:	Willmott–Matsuura

SYMBOLS

$\tilde{\boldsymbol{A}}_0$	: Fuzzy regression coefficients
C	: Error covariance matrix
$\mathbf{c_j}$	: Spread of the fuzzy coefficient
$\boldsymbol{d}_{iU}^{+}, \boldsymbol{d}_{iL}^{+}$	: Upper and lower value of estimated interval
$\boldsymbol{d}_{iU}^{-}, \boldsymbol{d}_{iL}^{-}$	: Upper and lower value of observed interval
h	: Degree of fitting index
ET	: Evapotranspiration
K	: Kalman gain
L	: Linear closure constraint
M, N	: Number of products
P	: Precipitation
Q	: Runoff
r	: Error residual
S, V	: Covariance matrix
$\boldsymbol{S}_i, \boldsymbol{s}_{\varepsilon_i}$	: Spread of the dependent variable
$\mathbf{S_R}$	: Potential maximum retention
t	: Time
T	: Transpose
$\boldsymbol{v}_{ij}$	: Covariance between individual noises
$\boldsymbol{w}_{i,m}$	: Merging weight
$\hat{\boldsymbol{x}}_k$	: State estimates
$\boldsymbol{y}_i$	: Center of the dependent variable
$\boldsymbol{y}_k$	: Measurement
$\boldsymbol{\alpha}_j$	: Center of the fuzzy coefficient
$\boldsymbol{\Delta S}$	: Change in terrestrial water storage
$\boldsymbol{\sigma}$	: Error variance
$\boldsymbol{\mu}_{\tilde{A}}(\boldsymbol{x})$	: Degree of membership
$\boldsymbol{\mu}_i, \boldsymbol{\omega}_i$	: Center and spread of estimated residual error
$\boldsymbol{\mu}_m$	: Long term monthly mean
$\boldsymbol{\varepsilon}_i$	: Observed residual error
$\boldsymbol{\vartheta}_i, \boldsymbol{\varphi}_i$	: Center and spread of observed residual error
$\boldsymbol{\eta}_i$	: True error

LIST OF TABLES

Page

LIST OF FIGURES

Page

IMPROVING THE PERFORMANCE OF REMOTE SENSING-BASED WATER BUDGET COMPONENTS ACROSS MID- AND SMALL- SCALE BASINS

SUMMARY

In the last few decades, many global basins have been threatened by rapid urban growth and global warming, resulting in changes in their climate regime. Climate change has increased the incidence of extreme weather events, uncertain water availability, water scarcity, and water pollution. Remote sensing (RS) has emerged as a powerful technique that provides estimations with high spatiotemporal resolution and broad spatial coverage. In recent years, the efficacy of RS products for water budget (WB) analysis has been widely tested and implemented in global and regional basins. Although RS products provide high temporal and spatial resolution images with a near-global coverage, uncertainty is still a significant problem. The main goal of this study is to utilize two different approaches to minimize the uncertainty of the products and to improve RS-based WB estimations in mid- and small- scale basins.

The first approach aims to improve the efficacy of water WB estimations from various hydrological data products in the Sakarya basin by; (1) Evaluating the uncertainties of hydrological data products, (2) Merging four precipitation (P) and six evapotranspiration (ET) products using the error variances, and (3) Employing the Constrained Kalman Filter (CKF) method to distribute residual errors (r) among WB components based on their relative uncertainties. The results showed that applying bias correction before the merging process improved estimations of P products with decreasing root mean square error (RMSE), except PERSIANN. VIC and bias-corrected CMORPH products outperformed other ET and bias-corrected P products, respectively, in terms of mean merging weights. The terrestrial water storage change (ΔS) is the primary reason for non-closure errors. This is mainly caused by the two facts. First, the Sakarya basin is a relatively small basin that GRACE can not simply resolve. Second, while P, ET, and Q mostly describe the surface water dynamics, ΔS includes both the surface water and ground water. It is well known that surface water and ground water have completely different dynamic behaviors. The change in surface water is much faster than the change in groundwater. The CKF results were insensitive to variations in uncertainties of runoff (Q). P derived from the CKF was the best output, with the highest correlation coefficient (CC) and the smallest root mean square deviation (RMSD).

In the second approach, the annual r in the WB equation arising from the uncertainties of the RS products was minimized by applying fuzzy correction coefficients to each WB component. For analysis, three different fuzzy linear regression (FLR) models with fourteen different sub-models were used in the two basins having different spatial characteristics, namely Sakarya and Cyprus basins. The performance of sub-models is better in the Sakarya basin than that in the Cyprus basin, which has a higher leakage

error due to across ocean/land boundary. Moreover, the Cyprus basin is too small for some low-resolution RS-based products to resolve. The Zeng and Hojati sub-models outperformed Tanaka sub-models in the Sakarya basin, whereas Zeng Case-I, Zeng Case-II, and Hojati (degree of fitting index (h) =0.9) sub-models showed the best performance in the Cyprus basin. The best fuzzy sub-models reduced the error up to 68% and 52% in terms of mean absolute error compared to non-fuzzy model in the Sakarya and Cyprus basins, respectively. Further evaluations showed that the best sub-model P well captured the temporal patterns of gauge observations in both basins. Moreover, they have the best consistency with gauge observations in terms of RMSE, Kling-Gupta efficiency (KGE), and percent bias (PBIAS) in the both basins. The results proved that the second approach will provide valuable insights into WB analysis in ungauged basins by incorporating the fuzzy logic approach into hydrological RS products.

In general, the FLR and CKF derived P, ET, and Q showed similar seasonal variation with peak and bottom values appeared in nearly the same years. In terms of CC, RMSE, and bias, fuzzy outputs show closest agreement with CKF outputs for Q, with slightly less agreement for P and ET, and much less agreement for ΔS. It can be concluded that the majority of the errors in the second approach are caused by fuzzy ΔS.

KÜÇÜK VE ORTA ÖLÇEKLİ HAVZALARDA UZAKTAN ALGILAMA TABANLI SU BÜTÇESİ DEĞİŞKENLERİNİN İYİLEŞTİRİLMESİ

ÖZET

Su, tüm canlıların yaşamlarını idame ettirebilmeleri için gerekli en önemli doğal kaynaktır. Son yıllarda, artan kentleşme ve küresel iklim değişikliğine bağlı karbon salımındaki artış gibi etkenler birçok global ölçekteki havzanın iklimlerinde değişikliklere neden olmaktadır. İklim değişikliği ise ekstrem hava olaylarının (sel, kuraklık), su kıtlığının ve su kirliliğinin görülme sıklığını artırarak havzalar üzerinde büyük bir tehdit olmaya başlamıştır. Bunun yanında aşırı yeraltı suyu çekimi nedeniyle birçok akifer tuzlanma nedeniyle kullanılamaz hale gelmiştir. Bu sebepler göz önünde bulundurulduğunda havza su bütçesi bileşenlerinin miktarını tahmin etmek, su kaynakları planlaması, sel ve kuraklık tahmini, atık su arıtma ve enerji temini için oldukça çok önemlidir. Su bütçesi bileşenleri, temel olarak, yağış (P), evapotranspirasyon (ET), akış (Q) ve karasal su depolamasındaki değişikliktir (ΔS).

Yersel gözlem istasyonları su bütçesi bileşenlerini izlemenin en doğru yöntemi olarak kabul edilmiştir. Bununla birlikte, gözlem istasyonlarının yüksek yapım ve bakım maliyetleri nedeniyle dünyanın birçok yerinde, özellikle gelişmekte olan ülkelerde, çok az hatta hiç gözlem istasyonu bulunmamaktadır. Öte yandan, su bütçesinin ET gibi bazı bileşenleri, bölgenin iklim koşullarını doğru bir şekilde tahmin etmek için, yoğun ölçü ağlarına ihtiyaç duymaktadır. Bitki örtüsü heterojenliği ET'yi doğrudan etkilediğinden, seyrek noktalardaki ölçüler büyük havzaların gerçek ET değerlerini yansıtamaz.

Son zamanlarda, su bütçesi çalışmaları gelişmiş uydu uzaktan algılama teknikleri ile yeni bir döneme girmiştir. Çeşitli uydu ürünleri kullanılarak Dünya üzerindeki uzak ve hatta erişilemeyen yerleri düzenli olarak izlemek artık mümkündür. Uydu gözlemlerinin güvenilirliği henüz yersel ölçümler kadar iyi olmasa da, uydu uzaktan algılama tekniği yersel istasyonlara göre daha az maliyetlidir ve politik durumlardan etkilenmeden dünyanın her yerinden veri toplayabilir. Uydu uzaktan algılama tekniği, neredeyse tüm dünya için yüksek zamansal ve mekansal çözünürlüğe sahip veriler sağlamaktadır. GRACE misyonunun başlatılmasından sonra, özellikle gelişmekte olan bölgelerde, uzaktan algılama tabanlı su bütçesi çalışmaları önemli ölçüde artmıştır. GRACE misyonu, 2002'den beri yüksek hassasiyetle aylık verileri sunmaktadır. GRACE misyonunda önce, P ve ET için birkaç uzaktan algılama ürünü halihazırda bulunmaktaydı (P için TRMM ve PERSIANN ve ET için MODIS). Günümüzde uydu uzaktan algılama ile sadece Q ölçülememektedir; ancak Surface Water and Ocean Topography (SWOT) misyonu, Kasım 2022'den itibaren büyük ölçekli havzaların Q verilerini sağlayarak bu talebi yerine getirecektir.

Uzaktan algılama ürünleri, küresel ölçekte yüksek zamansal ve mekansal çözünürlüklü görüntüler sağlasa da, uydu verilerindeki belirsizlik hala önemli bir sorundur. Bu çalışmanın temel amacı, orta ve küçük ölçekli havzalarda uzaktan algılama tabanlı su bütçesi tahminlerini iyileştirmek için iki farklı yaklaşımı kullanmaktır.

Birinci yaklaşım Sakarya havzasına uygulanmıştır ve bu yaklaşımda üç temel adım izlenmiştir. İlk olarak hidrolojik veri ürünlerinin belirsizlikleri değerlendirilmiştir. P verilerinin belirsizliklerinin hesaplanmasında yersel istasyon ölçüleri referans olarak kullanılırken, ET için yersel ölçü verileri bulunmadığından ET verilerinin belirsizliklerinin hesaplanmasında generalized three-cornered hat (GTCH) metodu kullanılmıştır. GTCH metodu, herhangi bir ön bilgi gerektirmeden çeşitli hidrometeorolojik veri ürünlerinin göreceli belirsizliğini tahmin etmede oldukça başarılı bir yöntemdir. ΔS için belirsizlik değerleri veri sağlayıcısından (Jet Propulsion Laboratory) temin edilmiştir. Q belirsizliği için herhangi bir ön bilgi bulunmamaktadır. Dolayısıyla büyük (42.8 %) ve küçük (6.2 %) belirsizlik değerlerinin sonuçlara etkisini anlamak için iki farklı belirsizlik değeri kullanılmıştır. Hidrolojik verilerin belirsizliklerinin değerlendirilmesinden sonra hata varyansları doğrultusunda dört P ve altı ET ürünü birleştirilmiştir. Son adımda ise Constrained Kalman Filter (CKF) yöntemi ile artık hataları su bütçesi bileşenleri arasında göreceli belirsizliklerine dağıtılmıştır. Sonuçlar, birleştirme işleminden önce bias düzeltmesi uygulanmasının, PERSIANN hariç, P ürünlerinin tahminlerini iyileştirdiğini (düşen RMSE ile) göstermiştir. Ortalama birleştirme ağırlıkları açısından VIC ve bias düzeltmeli CMORPH ürünleri sırasıyla diğer ET ve bias düzeltmeli P ürünlerinden daha iyi performans ortaya koymuştur. Sonuçlar ΔS'nin kapanmama hatalarının birincil nedeni olduğunu göstermiştir. Bu durum iki nedene bağlanabilir. Birincisi, Sakarya havzası, GRACE'in basitçe çözemeyeceği nispeten küçük bir havzadır. İkincisi, P, ET ve Q çoğunlukla yüzey suyu dinamiklerini yansıtırken, ΔS ise hem yüzey suyu hem de yeraltı suyu dinamiklerini yansıtmaktadır. Bilinmektedir ki, yüzey suyu ve yeraltı suyunun mekanizması birbirinden oldukça farklıdır. Yüzey suyundaki değişimler, yeraltı suyu değişimlere göre oldukça hızlıdır. CKF sonuçlarının, Q belirsizliklerindeki değişikliklere karşı duyarsız olduğu gözlemlenmiştir. Yapılan ileri değerlendirmelerde CKF'den türetilen P, en yüksek CC ve en düşük RMSD değerlerine (referans veriye göre) sahip olduğundan en iyi P çıktısı olarak kabul edilebilir.

İkinci yaklaşımda ise uzaktan algılama ürünlerinin belirsizliklerinden kaynaklanan su bütçesi denklemindeki yıllık hata, her bir su bütçesi bileşenine uygulanan bulanık düzeltme katsayıları ile minimize edilmiştir. İkinci yaklaşım Sakarya ve Kıbrıs havzalarına uygulanmıştır. Bu yaklaşımda on dört farklı alt modele sahip üç farklı bulanık doğrusal regresyon modeli kullanılmıştır. Kıbrıs'ın Sakarya havzasına kıyasla hem daha küçük olmasından hem de ada ülkesi olduğu için denizden kaynaklı sızma hatasına sahip olmasından dolayı, Kıbrıs havzası için alt modellerin performansı daha düşük çıkmıştır. Sakarya havzasında Zeng ve Hojati alt modelleri Tanaka alt modellerinden daha iyi performans gösterirken, Kıbrıs havzasında Zeng Case-I, Zeng Case-II ve Hojati (h=0,9) alt modelleri en iyi performansı göstermiştir. En iyi bulanık alt modeller, Sakarya ve Kıbrıs havzalarında bulanık olmayan modele göre ortalama mutlak hata açısından hatayı sırasıyla 67% ve 52%'ye kadar azaltmıştır. Daha sonraki değerlendirmeler ise, her iki havzadaki en iyi alt model P'nin yersel gözlemlerin zaman serisini iyi yakaladığını göstermiştir. Ayrıca, her iki havzada da bulanık P'nin RMSE, Kling-Gupta efficiency (KGE) ve yüzde sapma (PBIAS) açısından yersel istasyon gözlemleriyle en iyi tutarlılığa sahip olduğu gözlemlenmiştir. Sonuçlar, bulanık mantık yaklaşımının hidrolojik uzaktan algılama ürünlerine uygulanmasıyla, yersel istasyon ölçüsü yapılmayan havzalarda su bütçesi analizine ilişkin değerli bilgiler sağlayacağını göstermiştir.

Genel olarak, bulanık ve CKF'den türetilen yıllık P, ET ve Q değerlerinin benzer zaman serilerine sahip olduğu gözlemlenmiştir. CC, RMSE ve sapma açısından, bulanık çıktılar ile CKF çıktıları arasındaki en yakın ilişki Q için gözlemlenirken en uzak ilişki ise ΔS için gözlemlenmiştir. Bu durum bulanık yaklaşımda sıfırlanmayan artık hataların bulanık ΔS'den kaynaklandığını işaret etmektedir.

1. INTRODUCTION

Water is the most crucial natural resource for all living beings. Living beings can not survive without water, and it maintains the equilibrium of all living organisms on Earth with one another. Water covers most of the Earth's surface in the form of solid, liquid, and gas. However, among all, 97.5% is saltwater from the oceans and seas, and only 2.5% consists of fresh water from rivers and lakes. Furthermore, 75% of such low freshwater is trapped as glacial ice on mountains and at the polar regions. When these rates are considered, it is clear that the amount of freshwater that may be used is quite restricted.

In the last few decades, many global basins have been threatened by rapid urban growth and global warming, resulting in changes in their climate regime. Climate change has increased the incidence of extreme weather events, uncertain water availability, water scarcity, and water pollution. Water-related disasters accounted for about 74% of all-natural disasters in the previous 20 years, with a cumulative death toll of over 166,000 people killed by floods and droughts, affecting over three billion people and causing nearly $700 billion in damage [1]. According to the Global Water Institute, 700 million people globally might be relocated due to severe water scarcity by 2030 [2].

Considering the factors mentioned above, predicting the availability and pattern of terrestrial water budget (WB) components are crucial for water resources planning, flood and drought forecasting, wastewater treatment, and energy supply [3,4]. The WB is a continuity equation that quantifies the mass of water entering and leaving the system over time to illustrate water storage changes. The simplified form of the WB equation can be written as:

$$\Delta S = P - ET - Q \tag{1.1}$$

where ΔS is the change in terrestrial water storage (soil moisture, groundwater storage, snow, ice, lakes, etc.), P is precipitation, ET is evapotranspiration, and Q is runoff. All units within Equation (1.1) are [length]. Gauge measurements have traditionally been considered to be the most accurate method of monitoring WB components. However, most parts of the world, especially developing regions, have very few or even no gauge stations due to high construction and maintenance costs. On the other hand, some components of the WB, such as ET, need dense gauge networks to accurately forecast the region's climatic conditions. Since subsurface heterogeneity and vegetation type directly impact the ET, sparse point measurements can not reflect the actual ET of large basins [5,6].

Recently, WB studies have reached to a new era with advanced satellite remote sensing (RS) techniques. It is now possible to monitor remote or even inaccessible locations on Earth on a regular basis by using various RS products. Although satellite RS observations are less accurate than gauge measurements, they are also less expensive and may gather data from all around the world without being affected by political situations. RS products provide unprecedented temporal (up to sub-hourly) and spatial resolutions (up to 4 km) of WB components with a near-global coverage [7]. The remotely sensed WB studies have dramatically increased after the launch of the Gravity Recovery and Climate Experiment (GRACE) mission, especially in developing regions. The GRACE mission has provided monthly ΔS solutions with high precision since April 2002. Prior to the GRACE mission, several RS products were already available for P and ET (e.g., Tropical Rainfall Measuring Mission (TRMM) and Precipitation Estimation from Remotely Sensed Information using Artificial Neural Networks (PERSIANN) for P and Moderate Resolution Imaging Spectroradiometer (MODIS) for ET). Only Q can not be measured from satellite RS, but the prospective Surface Water and Ocean Topography (SWOT) mission will fulfill this demand by providing the first view of lakes and rivers from space after November 2022 [8].

1.1 Literature Review

1.1.1 Previous efforts to close the water budget (WB) equation

Although the researchers appreciate the contributions of satellite RS to basin hydrology, RS products face considerable uncertainty due to orbit shifting, sampling infrequency, retrieval algorithm imperfections, complex topography, and cloud top reflectance [6,9,10]. Several studies evaluated the degree of closure based on the deviation of Q estimated in Equation (1.1) from gauge Q data [11]–[16]. The lower the deviation from gauge Q data, the higher the degree of closure. Firstly, [11] attempted to close the WB equation using RS data over the Mississippi River basin. They validated RS products against reference data (in-situ measurements, land surface models (LSMs), reanalysis). It is found that the estimated Q overestimated gauge Q due to high positive bias in RS P, especially in the summer season. The WB non-closure was greatly decreased after bias removal RS P. Similarly, RS-based P was the leading cause of non-closure errors over the thirteen major US river basins in the [12] study. The authors compared RS-based P products with gauge observations, whereas the Variable Infiltration Capacity (VIC) model was used to determine uncertainties in RS-based ET and ΔS products due to the lack of in-situ measurements for ET and ΔS. The estimated Q overestimated gauge Q due to overestimation of P and underestimation of ET and ΔS. Then the sharp increase in the number of RS retrievals from different research centers let researchers select the best data combinations for each WB component. [13] used four different P and two different ET datasets in order to find the optimal combinations that minimized the WB non-closure. They found that the best agreement between estimated and gauge Q was within 1 mm/day when the Global Precipitation Climatology Project (GPCP) product for P and the University of Montana (MON) product for ET were used. [14] investigated the potential of purely RS products to achieve WB closure in the data-scarce Rufiji basin, Tanzania. There was low correlation between estimated and observed Q, and estimated Q generally underestimated observed Q. They also concluded that the long-term water resources assessment produce more consistent results than the short-term water resource assessment. [15] found that estimated Q greatly overestimated observed Q due to underestimation of RS-based ET. As reported in [11] and [12], [16] also demonstrated that RS-based P is the main contributor to WB errors in South America. The WB non-closure errors are lowest when the Multi-Source Weighted-Ensemble Precipitation (MSWEP) for P and the the Global Land Evaporation Amsterdam Model (GLEAM) for ET were used.

More recently, several studies merged different RS products that belong to the same WB component according to their merging weights, and a single "best estimate" for each component was obtained [17]–[23]. Error variances calculated with respect to reference data were used to assign a merging weight of each RS product. After merging process, the residual error (r) of the WB equation was calculated by,

$$r = P - ET - Q - \Delta S \tag{1.2}$$

and it was redistributed back into the WB components by dynamic modeling, namely Constrained Kalman Filter (CKF).

The key findings of various studies working on closing the WB with RS-based data are summarized in Table 1.1

Table 1.1 : Summary of RS-based studies testing WB closure.

Reference	Data products				Key findings	Study Area
	P	ET	Q	ΔS		
[11]	TRMM-CMORPH	PM	Gauge	GRACE	High positive bias in RS P, especially in the summer, was the leading cause of non-closure errors.	Mississippi river basin
[12]	TRMM-CMORPH- PERSIANN	MODIS	Gauge	GRACE-VIC	WB closure was not achieved due to the overestimation of P and underestimation of ET and ΔS	9 major US river basins
[20]	GPCP-TRMM-CMORPH-PERSIANN	PM-PT-SEBS	Gauge	GRACE	It was not possible to close the WB with errors of 5-25% of the average annual P. CKF technique was used to close the WB equation.	10 global river basins
[13]	GPCP-TRMM-CMORPH-PERSIANN	MON-PRI	Gauge	GRACE	The best spatiotemporal agreement between estimated and observed Q was within 1 mm/day when the GPCP product for P and MON for ET were used.	Amazon basin
[19]	CPC-CRU-WM-GPCC	SEBS-ERA-MPI-VIC	Gauge	GRACE-LSM	Error variances calculated with respect to reference data were used to assign a merging weight of each RS product. After the merging process, errors were redistributed back into the WB components by CKF.	32 global river basins
[24]	TRMM	MODIS	Gauge	GRACE	Estimated Q was overestimated primarily due to TRMM P overestimation.	3 largest Brazilian river basins
[6]	TRMM	MODIS	-	GRACE	GRACE-TWSC was significantly lower than P-ET where annual mean Q was below 10 mm/year.	Australia
[15]	TRMM	MODIS	Gauge	GRACE	Negative bias in RS ET was the main source of non-closure errors.	Upper Paraguay river basin

1.1.2 Fuzzy logic approach in remote sensing (RS) and hydrology

Several studies have used fuzzy logic in various topics of hydrology [25]–[31]. [31] combined the Inverse Distance Weighted (IDW) method with fuzzy logic to interpolate P in the Feitsui basin, Taiwan. Although they did not examine the impact of the distribution of the P stations on their method, the suggested method outperformed traditional interpolation tehniques (e.g., arithmetic mean, thiessen polygon, IDW) for estimating P. [25] tried to reduce annual WB r for the Azghand catchment, Iran, by applying fuzzy coefficients to the WB components derived from the gauge stations and empirical equations. Their model was able to reduce the mean absolute r by 79%. [28] suggested a neuro-fuzzy stacking approach to estimate Q from gauge P. The suggested method provided better Q estimations than other stacking models. In the field of RS, fuzzy logic was frequently used for image classification [32]–[34]. [32] evaluated the accuracy of land cover maps derived from fuzzy classification with respect to ground data. He demonstrated that fuzzy classification-based land cover maps are the most accurate representations compared to others. More recently, [34] tried to reduce the uncertainty in image classification resulting from the heterogeneity of similar ground objects. They utilized an interval type-2 fuzzy sets generation method, and their method was able to suppress heterogeneity of the similar objects at RS images, increasing the accuracy of image classification. their method was able to suppress heterogeneity of the similar objects at RS images, increasing the accuracy of image classification. In a different study, [26] merged elevation, slope, distance from the coast, aspect, and P data obtained from weather radar by using a fuzzy joint membership function (JMF) to get accurate P grids for the Mediterranean region. The results show that JMF P grids have a higher correlation with in-situ data than original radar grids. [27] delineated potential groundwater zones in the Shanxi region, China, with the help of fuzzy logic, RS, and Geographic Information Systems (GIS). The generated maps were extremely close to the ground-truth data.

1.1.3 Literature research on the study area

Two basins with different basin characteristics and climatic conditions were used in this study: i) Sakarya basin; ii) Cyprus basin.

The Sakarya basin is being studied for a variety of reasons. It has significant water potential and is well suited to the construction and operation of multifunctional hydraulic and water resources projects, such as hydroelectric power plants, water supply and diversion, and flood control. The water capacity of the Sakarya basin is sufficient to meet not just the region's domestic and industrial water requirements but also the water needs of neighboring basins through inter-basin water transfer projects, such as supplying a large portion of the mega city Istanbul's water demand. Recently, the basin has been suffering from water pollution due to increasing population and industry [35]–[37]. The water pollution in the Sakarya basin was found to be greater above the United Nations Educational, Scientific and Cultural Organization (UNESCO) standards in a research conducted by [35].

Unfortunately, despite its strategic importance, there is no comprehensive WB study in the Sakarya basin. Moreover, RS-based hydrological data products have never been evaluated in the basin. The majority of work done in the basin has mostly focused on the Q [38]–[42]. [39] showed that the Q in the Sakarya basin experienced a significant decreasing trend starting from 1970. Similar trends were also reported in [38,42]. Another study conducted by [43] tried to show how the spatial distribution of P in the Sakarya basin has changed over the years. He found that although the P was in an increasing trend in the coastal parts of the basin, it was in a decreasing trend in the inner parts. The study conducted by the [44] is the only one that employed all WB components simultaneously. They implemented the Water Evaluation and Planning System—Plant Growth Model (WEAP-PGM) to estimate WB components in the Sakarya basin at annual scale. The proposed model estimated Q as 4747 million m^3/year, ET as 23011 million m^3/year, and flow to groundwater as 3065 million m^3/year. They showed that the estimated Q was in good agreement with observed Q.

There are very few gauge stations available in the Cyprus basin. Several studies have used RS products to estimate WB components in the Cyprus basin [3,45]–[49]. [45] evaluated the ability of the Climate Hazards Group Infrared Precipitation with Station (CHIRPS) data to predict P extremes in the Cyprus. In terms of mean daily values, the CHIRPS data correlated well with the available station data; however, no correlation was found when estimating maximum values. [47] compared the TRMM 3B43 and the Integrated Multi-satellitE Retrievals for Global Precipitation Measurement (IMERG) products over the Cyprus. It was observed that IMERG captured the temporal pattern of gauge observations slightly better than TRMM 3B43. However, both products underestimated gauge P, especially in the winter. In Cyprus, RS-based ET studies have primarily focused on crop ET instead of actual ET [48,50]. By neglecting the Q in the Cyprus basin, [3] has attempted to estimate other WB components using various RS data and models. It was found that the peaks of GRACE ΔS estimations were about 2 months later than the peaks of P estimations. Another important finding was that the equivalent water height measured by GRACE experienced a strong downward trend, with average rate of -1.56 mm/year.

1.2 Novelity and Objective of Thesis

So far, WB studies have been mainly conducted in large-scale global basins due to the low spatial resolution of the GRACE satellite gravimetry mission. Several studies have shown that GRACE errors are inversely proportional to the size of the basin [16,51]–[55]. GRACE errors were found to reach up to 130% in basins with smaller than 100,000 km^2 [16]. [54] also mentioned that the GRACE ΔS estimations are likely to have large errors in basins with areas of less than 150,000 km^2. However, researchers need to improve WB outputs in small or mid-scale basins.

The early studies commented that ET is poorly observed from the ground in comparison to P and Q. Therefore, the uncertainty in RS-based ET was mainly evaluated using LSMs or simple empirical formulas [11,12,20,24]. However, both LSMs and the empirical techniques also hold substantial uncertainties for ET estimation [56]–[58]. The generalized three-cornered hat (GTCH) method is highly successful in estimating the relative uncertainty of various hydrometeorological data products without requiring any prior knowledge [6,59]–[64]. [65] indicated that the GTCH-integrated ET is closer to the FLUXNET ET observations than other techniques.

Additionally, there is still no method to improve the reliability of RS data for ungauged basins. Fuzzy logic, first suggested by [66], has emerged as a powerful technique to model various engineering problems that deal with vagueness and uncertainty [25,67,68]. The basic concept is to think of system parameters as fuzzy numbers rather than crisp (exact) numbers to capture the total uncertainty of the parameters, and each parameter is defined by its membership function. Although several studies have already used fuzzy logic in various topics of RS and hydrology (Section (1.1.2)), it has never been applied to RS-based hydrological data products containing a significant uncertainty level. Considering the uncertainty in RS products, incorporating fuzzy logic into RS can provide valuable outputs for the ungauged basins.

Considering the factors mentioned above, we followed two different approaches to improve WB estimations in two basins, namely Cyprus and Sakarya basins. In the first approach, we used rainfall gauge measurements and the GTCH method to determine error variances of each P and ET product, respectively. Error variances were used to merge P and ET products separately into a single best estimate. CKF was then applied to enforce WB closure. Due to the lack of Q observations in the Cyprus basin, the first approach was only applied to the Sakarya basin. In the second approach, Fuzzy linear regression was used to decrease WB closure errors in both the Cyprus and Sakarya basins without the need for gauge observations.

2. STUDY AREA AND DATASETS

2.1 Study Area

Two basins were used in this study to examine the feasibility and effectiveness of the RS-based fuzzy logic method in different scaled basins: *i*) mid-scaled Sakarya basin; *ii*) small-scaled Cyprus basin.

The Sakarya basin is located in northwest Anatolia, Turkey, between 37° 96' - 41° 20' North latitudes and 29° 26' - 33° 24' East longitudes (Figure 2.1(a)). Due to its geographic location, the Sakarya basin is of extreme importance for transportation, cultural, industrial and agricultural activities, and economic amenities. The basin features a diverse range of geographical formations. As a result, the basin can be evaluated geographically as a whole, considering all of the features of the territories it encompasses. The basin's drainage area is roughly 58160 km^2, encompassing approximately 7% of Turkey. It comprises 52% agricultural land, 45% forest and semi-natural terrain, and 2.2% urban territory, among other minor land-use types. Wetlands cover around 0.2% of the basin, whereas surface waters cover approximately 0.4% [69]. The majority of the basin has a typical continental climate, with a mean annual P of about 500 mm. The maximum long-term daily measured P in the basin is 127.7 mm, whereas the maximum evaporation is recorded as 60 mm. The Sakarya river potentially constitutes 3.4% of all rivers that originate in Turkey. The mean annual flow rate is 6400 million m^3/year. The long-term temperature fluctuations depict that -28°C can be measured in winter while up to 44° C can be felt in summer.

The Cyprus basin covers almost half of the Cyprus island, whose total geographical area is 9251 km^2. The study area is located in between 34° 54' - 35° 41' North latitudes and 32° 35' - 34° 35' East longitudes (Figure 2.1(b)). Cyprus is located in the eastern Mediterranean Sea and is one of the major basins under frequent droughts [70]. Due to its geographic location, it is of extreme importance for agricultural and cultural activities as well as the touristic amenities. Contrary to Sakarya Basin, water shortages are evident, and the problem is lately solved by an inter-basin water transfer project through the Mediterranean Sea from Turkey. Within the basin, the Kyrenia Range lays parallel to the Mediterranean Sea, generating significant spatial variations on climatic factors. The Cyprus basin consists of ephemeral rivers that have not been flowing in some winter seasons. The maximum altitude of the basin is 1981 m above mean sea level, and the maximum hydraulic flow length is estimated to be 68 kilometers with varying watershed slopes ranging from 2% to 56% [71]. The basin's drainage area is roughly 4990 km^2, encompassing approximately 54% of Cyprus. The majority of the basin has a typical Mediterranean climate, with a mean annual P of about 385.2 mm [72]. P in general increases from east to west. The mean temperature varies from 5 to 15°C in the winter months, whereas it reaches up to 40°C during summer.

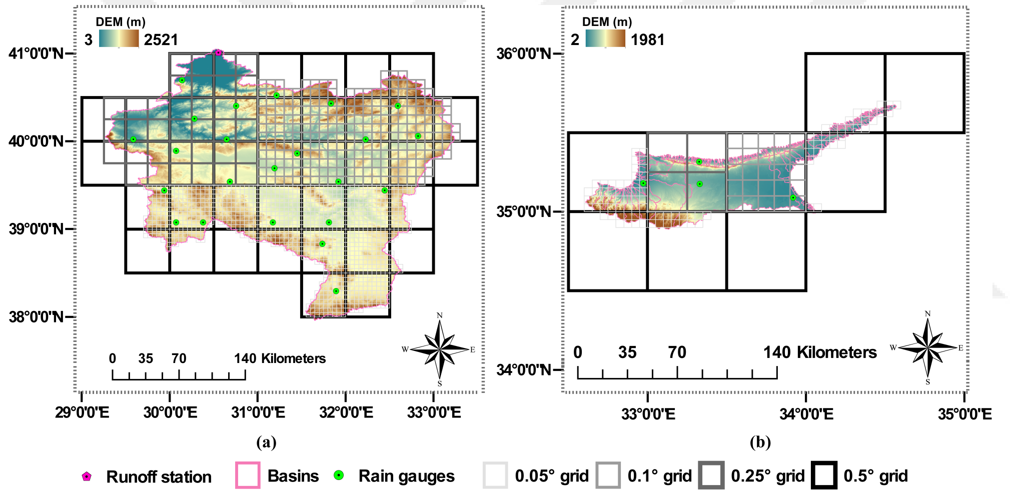

Figure 2.1 : The spatial resolution of RS products over (a) Sakarya and (b) Cyprus basins. The pink point represents the Adatepe Q station at the outlet of the Sakarya basin, and the green points indicate meteorological stations used in both basins. The color scale represents the topography of Sakarya basin and the Mediterranean island Cyprus.

2.2 Datasets

2.2.1 First approach

2.2.1.1 RS, land surface model (LSM), and reanalysis products

The first approach was applied to the Sakarya basin. For the first approach, we used four RS-based P products: PERSIANN, the CPC Morphing Technique

(CMORPH), TRMM, and GPCP. For ET, we considered six products, including the three RS-based ET, two Global Land Data Assimilation System (GLDAS) LSMs, and reanalysis. The three RS-based ET products are MODIS, GLEAM, and the Numerical Terradynamic Simulation Group (NTSG). The two GLDAS LSMs are the VIC and the Neural Optimization Applied Hydrology (NOAH). The only reanalysis product is the TERRACLIMATE. The Jet Propulsion Laboratory (JPL) provides raw Mass Concentration (MASCON) ΔS solutions. The land-grid-scaling has been applied to the MASCON ΔS solutions to decrease the noise caused by the sampling and post-processing of GRACE observations.

2.2.1.2 Gauge observations

We used monthly P data from 27 recording-type rainfall stations provided by the Turkish State Meteorological Service to determine the uncertainties of the each P product. The consistency of 27 rainfall stations was checked using the Double Mass Curve method. Consequently, no station was eliminated, and the mean monthly P of the Sakarya basin was calculated using the Kriging Interpolation Technique [73,74].

The daily long-term measured Q data at the outlet of the Sakarya basin were provided by the State Hydraulic Works of Turkey. There are no missing data during the study period. We aggregated daily Q measurements to the monthly temporal resolution to be consistent with the time interval of other products used in the first approach. The Q data is available at https://www.dsi.gov.tr/.

The temporal coverage of the first approach is from January 2005 to December 2011 at a monthly interval. Therefore, all products considered in this approach were aggregated to monthly temporal resolution and remapped to the basin scale by pixel averaging. The summary of the datasets used for the first approach is shown in Table 2.1.

2.2.2 Second approach

The second approach was used in both the Sakarya and Cyprus Basins. All of the products used in the second approach (except Q) are RS-based products. For ΔS, GRACE MASCON solutions were used in both basins. For the Sakarya basin, in-situ Q

Table 2.1 : Summary of the datasets used in the first approach.

Product	Source	Spatial and Temporal Resolution	Reference	Study period
		Precipitation (P)		
PERSIANN	Satellite	Monthly, 0.25°	[75]	2005-2011
CMORPH	Satellite	Monthly, 0.5°	[76]	
TRMM	Satellite	Daily, 0.25°	[77]	
GPCP	Satellite	Monthly, 0.5°	[78]	
Rainfall gauges	In-situ	Monthly, point scale	Turkish State Meteorological Service	
		Evapotranspiration (ET)		
MODIS	Satellite	Monthly, 0.05°	[79]	
GLEAM	Satellite	Monthly, 0.25°	[80]	
NTSG	Satellite	Monthly, 8 km	[81]	
NOAH	LSM	Monthly, 0.25°	[82]	
VIC	LSM	Monthly, 1°	[83]	
TERRACLIMATE	Reanalysis	Monthly, 0.05°	[84]	
		Water Storage Change (ΔS)		
JPL MASCON	Satellite	Monthly, 0.5°	[85]	
		Runoff (Q)		
Runoff gauge	In-situ	Daily, point scale	State Hydraulic Works of Turkey	

measurements were used. For the Cyprus basin, the Soil Conservation Service (SCS) Curve Number (CN) method based Q estimations were used as there are no in-situ Q observations. SCS-CN method combines watershed characteristics (soil type, land cover) with climatic events to derive CN of the watershed [86]. The higher the CN, the greater the Q capacity. SCS-CN based Q can be calculated by the following equation:

$$Q_{SCS} = \frac{(P_{sta} - 0.2S_R)^2}{(P_{sta} + 0.8S_R)} \tag{2.1}$$

where P_{sta} is the mean of the daily P from four gauge stations in the Cyprus basin (Figure 2.1(b)). S_R is the potential maximum retention, and it is calculated as:

$$S_R = \frac{1000}{CN} - 10 \tag{2.2}$$

For Q calculations, the Cyprus basin was divided into 366 sub-basins (Figure 2.3(a)) using a digital elevation model (DEM) (Figure 2.1(b)) with a spatial resolution of 12 meters [71]. DEM is integrated with the GIS technique to delineate watersheds and corresponding stream networks (Figure 2.3(b)) to create a database of sub-basin characteristics (e.g., slope, area, hydraulic flow length). Land cover data are obtained from the Copernicus Land Monitoring Service (https://land.copernicus.eu/)

and the soil map was taken from the Ministry of Agriculture and Natural Resources (http://tarim.gov.ct.tr/). The soil data are classified into four different hydrologic groups as A, B, C, and D based on their Q potential (Figure 2.2). The Q potential increases from A to D. The CN of each of the 366 sub-basins is then determined by overlapping the land cover map and the hydrologic soil map (Figure 2.3(c)). Q_{SCS} was calculated for 366 sub-basins separately and $(Q_{SCS})_{\text{mean}}$, the mean of the calculated Q_{SCS} values, was used for WB analysis in Cyprus basin.

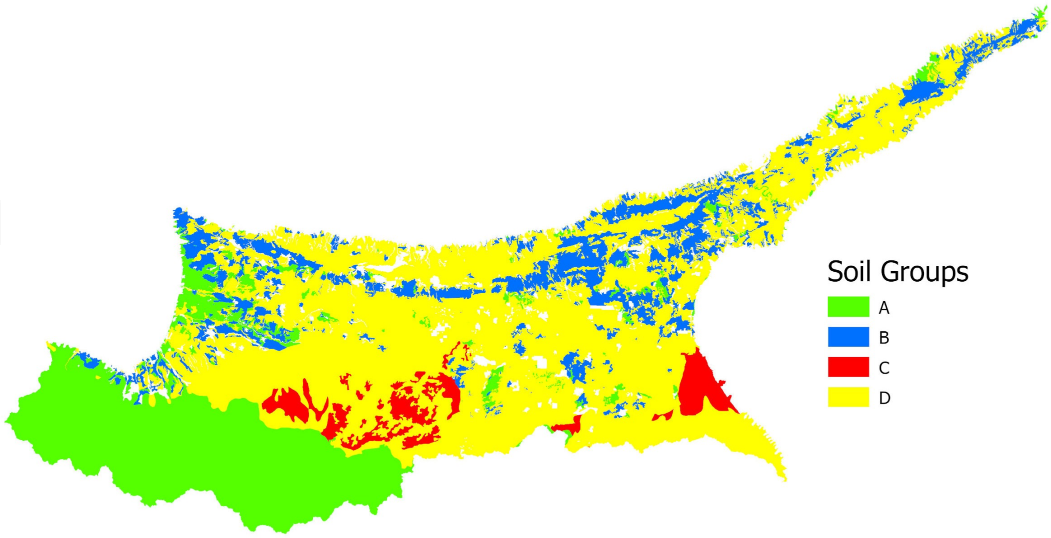

Figure 2.2 : The hydrologic soil groups in the Cyprus basin.

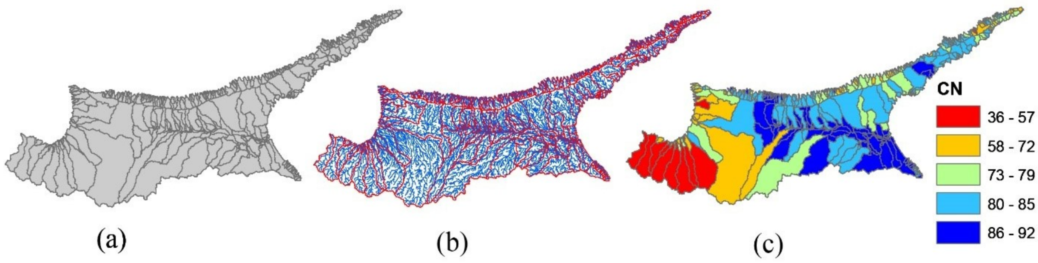

Figure 2.3 : Spatial distribution of all the (a) sub-basins; (b) stream-flows and (c) CN's in the Cyprus.

In total, five P products, three ET products, one ΔS product, and two Q data (in-situ measurements for the Sakarya basin and empirical estimations for the Cyprus basin) were considered in the second approach. Five P products contain CHIRPS, the Global Satellite Mapping of Precipitation (GSMaP), PERSIANN, CMORPH, and IMERG. Three ET products contain GLEAM, MODIS, and NOAH.

All products considered in the second approach were aggregated to annual temporal resolution and remapped to the basin scale by pixel averaging over 2003-2016 and 2019-2020. There is an 11-month data gap in GRACE data, from July 2017 to May 2018. Although some studies have used different approaches to fill the data gap [87,88], no centers have provided universally accepted solutions. Therefore, the years 2017 and 2018 were excluded from the analysis. Summary of the considered datasets for the second approach is presented in Table 2.2.

Details of all the datasets for each WB component are given in the Appendix A.

Table 2.2 : Summary of the datasets used in the second approach.

Product	Study basins	Spatial and Temporal Resolution	Reference	Study period
		Precipitation (P)		
CHIRPS	Sakarya, Cyprus	Annual, 0.05°	[89]	2003-2020
GSMaP	Sakarya, Cyprus	Monthly, 0.1°	[90]	
PERSIANN	Sakarya, Cyprus	Monthly, 0.25°	[75]	
CMORPH	Sakarya, Cyprus	Monthly, 0.5°	[76]	
IMERG	Sakarya, Cyprus	Monthly, 0.1°	[91]	
		Evapotranspiration (ET)		
GLEAM	Sakarya, Cyprus	Monthly, 0.25°	[80]	
MODIS	Sakarya, Cyprus	Annual, 500 m	[79]	
NOAH	Sakarya, Cyprus	Monthly, 0.25°	[82]	
		Water Storage Change (ΔS)		
JPL MASCON	Sakarya, Cyprus	Monthly, 0.5°	[85]	
		Runoff (Q)		
In-situ	Sakarya	Daily, basin scale	State Hydraulic Works of Turkey	
SCS-CN	Cyprus	Daily, basin scale	[86]	

3. METHODOLOGY

3.1 First Approach

The following three-step process was applied in this approach (Figure 3.1). First, we evaluated the uncertainties of different P and ET products. Rainfall gauge observations were used to calculate error variances of P products, whereas the GTCH method was used for ET products since there is no ground-truth data. Second, P and ET products were merged separately according to their estimated error variances. Finally, WB closure was performed using the CKF.

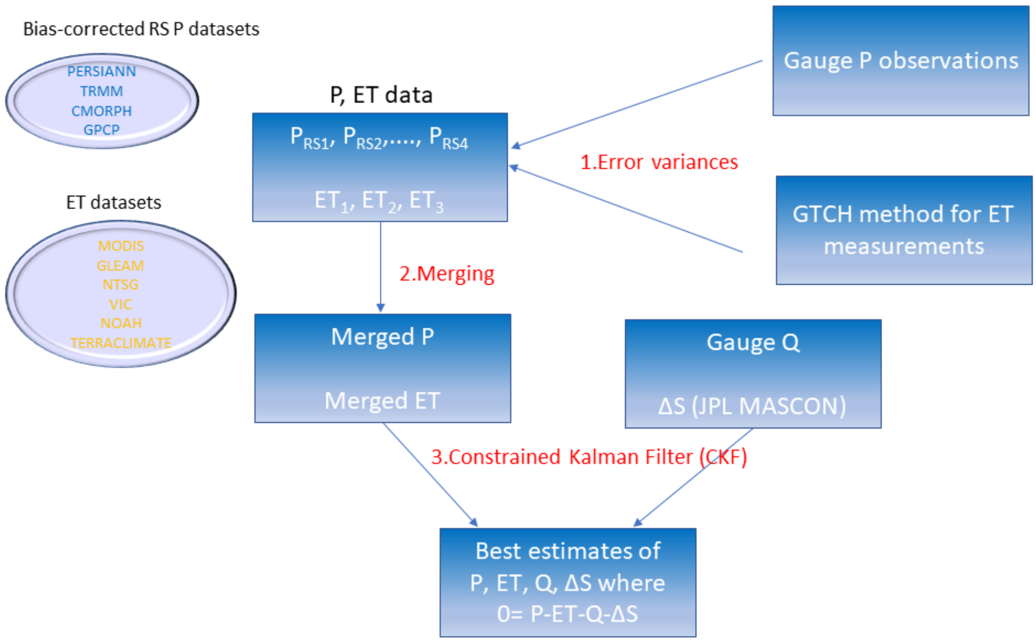

Figure 3.1 : A flow chart of the first approach.

3.1.1 Uncertainty analysis

3.1.1.1 Precipitation (P) uncertainty

Firstly, we applied a monthly bias correction on the raw RS-based P products for each month using the linear scaling bias correction method [92,93]. This method generates monthly correction values based on the ratio of observed and estimated values:

$$P^{*}_{est}(m) = P_{est}(m)\left(\frac{\mu_m\left(P_{obs}(m)\right)}{\mu_m\left(P_{est}(m)\right)}\right) \tag{3.1}$$

where $P^{*}_{est}(m)$ is the bias-corrected (BC) P at month m, $P_{est}(m)$ is the estimated P at month m, $\mu_m(P_{est}(m))$ is the long term monthly mean of estimated P, and $\mu_m(P_{obs}(m))$ is the long term monthly mean of observed P. After bias removal, error variances of each product were calculated against the best data (Considering that gauge observations indicate our best datasets, they were used to assess the uncertainties of each raw RS-based P product). Since the error of products may change from month to month, error variance calculations were carried out separately for each of the 12 months. Therefore, 12 different error variances were generated for each product.

Let's consider we have M products for the P, $\{P_i\}_{i=1,2,...,M}$. The error variance of the product i is then calculated by,

$$\sigma_i^2 = \frac{\sum_{k=1}^{t}\left(P_k - P_a\right)^2}{t}, \quad i = 1,2,\ldots,M \tag{3.2}$$

where σ_i^2 is the error variance of the ith product, P_k is the ith product estimation, P_a is the actual P, and t refers to the total number of observations.

3.1.1.2 Evapotranspiration (ET) uncertainty and GTCH method

Because there is no actual ET data in the Sakarya basin, we employed the GTCH method to quantify the uncertainties of ET products. GTCH method, first developed by [94], allows an estimation of the relative uncertainties of different products without a priori knowledge. This method considers cross-correlation across different products and does not need the products to be independent [94,95]. In the first approach, the GTCH method was applied to six ET products for separate months. The GTCH method divides N (6 in first approach) ET time series $\{ET_i\}_{i=1,2,...,N}$ into

$$ET_i = ET_A + \eta_i \tag{3.3}$$

where ET_A represents the actual ET and η_i is the true error of the ith product. Since the actual ET is not available, the differences between a reference ET product (TERRACLIMATE (ET_N) was chosen arbitrarily) and the remaining $N-1$ ET

products are calculated as follows:

$$Y_{i,t} = ET_i - ET_N = \eta_i - \eta_N, \quad i = 1, 2, \ldots, N-1 \tag{3.4}$$

where $Y_{i,t}$ is the $tx(N-1)$ differences matrix, and t denotes the time samples. It should be noted that the results are insensitive to the arbitrarily chosen reference data. The covariance matrix (S) of Y is shown by,

$$S = cov(Y) \tag{3.5}$$

The unknown NXN covariance matrix V of the individual noises is then described as,

$$V = \begin{bmatrix} v_{11} & v_{12} & \cdots & \cdots & v_{1N} \\ v_{21} & v_{22} & \cdots & \cdots & v_{2N} \\ \vdots & \vdots & \ddots & \cdots & \vdots \\ \vdots & \vdots & \vdots & \ddots & \vdots \\ v_{N1} & v_{N2} & \cdots & \cdots & v_{NN} \end{bmatrix} \tag{3.6}$$

where $v_{ij} = v_{ji}(i, j = 1, 2, \ldots, N)$ is the covariance between the individual noises ε_i and ε_j, and v_{ii} is the unknown error variance of the ith product. To compute unknown v_{ii} values, V is related to the S by,

$$S = J.V.J^T \tag{3.7}$$

where $(N-1)xN$ matrix J is defined as,

$$J = \begin{bmatrix} 1 & 0 & \cdots & 0 & -1 \\ 0 & 1 & \cdots & 0 & -1 \\ \vdots & \vdots & \vdots & \vdots & \vdots \\ 0 & 0 & \cdots & \cdots & -1 \end{bmatrix} \tag{3.8}$$

However, the unknown v_{ii} values can not be solved by Equation (3.7) since the number of equations is smaller than the number of unknowns. [96] proposed the following minimization problem based on the Kuhn–Tucker theorem to compute unknown elements. The aim is to minimize the objective function shown as,

$$F(v_{1N}, \ldots, v_{NN}) = \frac{1}{(\sqrt[n-1]{\det(S)})^2} \sum_{i<j}^{N} v_{ij}^2 \tag{3.9}$$

subject to

$$H(v_{1N}, \ldots, v_{NN}) = -\frac{\det(V)}{\det(S) \cdot \sqrt[n-1]{\det(S)}} < 0 \tag{3.10}$$

$$v_{iN}^{(0)} = 0, i < N \text{ and } \quad v_{NN}^{(0)} = \frac{1}{2 \cdot S^*}, \quad S^* = [1,\ldots,1] \cdot S^{-1} \cdot (1,\ldots,1)^T \tag{3.11}$$

where det($\bullet$) is the matrix determinant, and T is the transpose. Finally, the diagonal v_{ii} values (same as σ_i^2) are obtained by solving the minimization problem. The square root of the diagonal v_{ii} values represents the standard error of evaluated ET products.

3.1.1.3 Uncertainty of change in terrestrial water storage (ΔS) and runoff (Q)

The data producer, JPL, provides the pixel-based uncertainties of the MASCON ΔS solutions. The basin mean of the ΔS uncertainties was used for the calculations in the first approach. To the best of our knowledge, there is no uncertainty quantification for Q in the Sakarya basin. [11] assumed that gauge Q observations have 5% to 10% errors. The uncertainty of Q data was found to range from 6.2% to 42.8% in another study conducted by [97]. In order to test the impact of different Q error values on the CKF outputs, both Q uncertainty of 6.2% and 42.8% were considered in the first approach.

3.1.2 P, ET merging

Error variances of each P and ET product were calculated in Sections (3.1.1.1-3.1.1.2). Now, our objective is to find the best-merged estimate for each month, $m = 1, 2 \ldots, 12$

,

$$ME_{m,t} = \sum_{i=1}^{M,N} w_{i,m} * EST_{i,m} \tag{3.12}$$

in which $ME_{m,t}$ is the merged estimate for the mth month time series, $w_{i,m}$ is the merging weight of product i ($i = 1, 2, \ldots, M$ for P, and $i = 1, 2, \ldots, N$ for ET) in month m, and $EST_{i,m}$ is the ith product estimation in month m. Merging weight can be calculated by the following equation:

$$w_{i,m} = \frac{1/\sigma_{i,m}^2}{\sum_{j=1}^{M,N} 1/\sigma_{j,m}^2} \tag{3.13}$$

where $\sigma_{i,m}^2$ is the error variance of i th product for month m. $\sum w_{i,m}$ should be equal to 1. The error variance of the merged estimate in month m can then be calculated as

$$\sigma_m^2 = \frac{1}{\sum_{j=1}^{M,N} 1/\sigma_{j,m}^2} \tag{3.14}$$

It should be noted that the above equations are valid for uncorrelated Gaussian errors.

3.1.3 Constrained Kalman Filter (CKF) algorithm for WB closure

3.1.3.1 Closure residual

Suppose

$$X^T = \begin{bmatrix} P & ET & Q & \Delta S \end{bmatrix} \tag{3.15}$$

shows the vector of WB variables for any month. Symbol T refers to the transpose of the vector. As described before, closure is generally not possible due to the uncertainties of products. Therefore, the WB residual, r, may not be equal to 0:

$$r = P - ET - Q - \Delta S \neq 0 \tag{3.16}$$

However, the law of conservation of mass tells us that the water entering the basin must be equal to the sum of the water leaving the basin and the water stored in the basin unless there is a mass exchange between the neighboring basins. From this knowledge,

$$r = LX = 0 \tag{3.17}$$

must be satisfied and

$$L = \begin{bmatrix} 1 & -1 & -1 & -1 \end{bmatrix} \tag{3.18}$$

is the linear closure constraint.

3.1.3.2 Kalman filter

Kalman filter is an optimal estimation algorithm that predicts system states from inaccurate and uncertain measurements [98]. It consists of two processes: predict and update Figure 3.2. The prediction process uses the previous state estimation ($\hat{x}_{k-1}$) to generate the a priori state estimation ($\hat{x}_k{}^-$) and its error covariance ($P_k{}^-$). The second step of the algorithm uses the a priori state estimate calculated in the prediction step and update it to find the a posteriori state estimate and its error covariance. The a priori state estimate is subtracted from the corresponding measurement (y_k) and the resulting difference is then multiplied by the Kalman gain (K) to obtain the a posteriori state estimate. The Kalman gain is computed such that it minimizes the a posteriori error covariance (R). The Kalman filter has the advantage of being recursive, which means that it only uses the current measurements, the a priori state estimate, and its uncertainty matrix rather than storing all previous measurements.

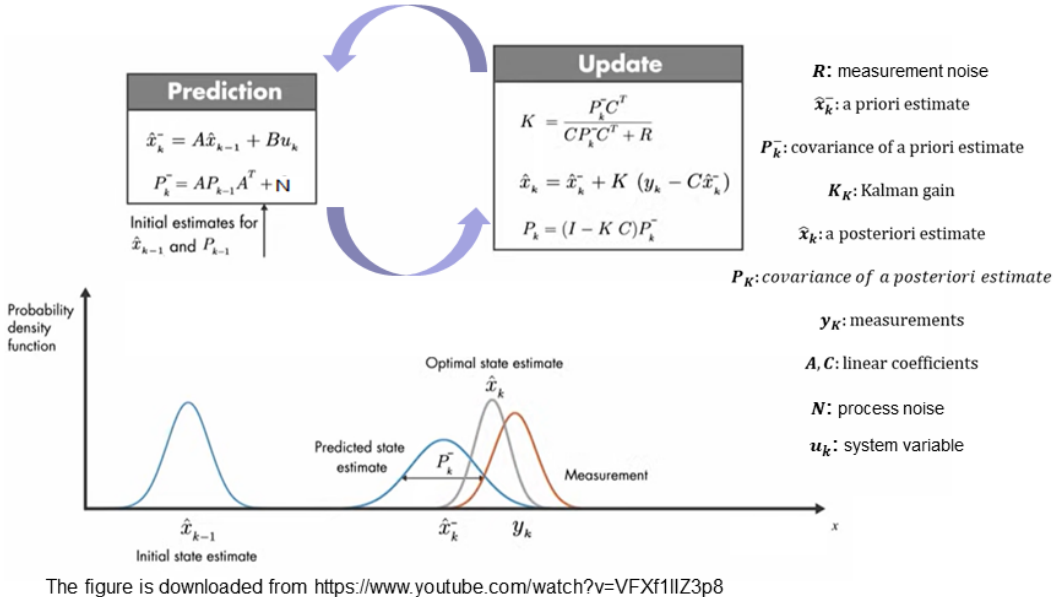

Figure 3.2 : Framework of the Kalman filter algorithm.

3.1.3.3 CKF

The data merging process merges variables according to their error variances without considering WB constraint. In the first approach, CKF was used after the merging step to enforce the closure. CKF is a type of Kalman filter that is used when the system constraints are known. The CKF algorithm may be described as follows. Let

$$X_{\text{merged}} = \left[\, P_{\text{merged}}\; ET_{\text{merged}}\; Q \quad \Delta S \,\right]^T \tag{3.19}$$

be the vector of WB variables at hand after merging step for any month. $r_{\text{merged}} = L.X_{\text{merged}}$ is not necessarily equal to zero, and new datasets are needed to make residual error zero. New closure-constrained estimates can be derived from

$$X_{CKF} = X_{\text{merged}} + K\left(0 - LX_{\text{merged}}\right) \tag{3.20}$$

in which $K = CL^T\left(LCL^T\right)^{-1}$ is the Kalman gain and C is the error covariance matrix. Here, the measured WB error and its error covariance are both equal to zero. Given $r_{\text{merged}} = L.X_{\text{merged}}$, Equation (3.20) can be rewritten as

$$X_{CKF} = X_{\text{merged}} - CL^T\left(LCL^T\right)^{-1} r_{\text{merged}} \tag{3.21}$$

X_{CKF} represents the "perfect" estimations that close the WB. The error covariance matrix is given by

$$C = \begin{bmatrix} \sigma^2_{m,P} & 0 & 0 & 0 \\ 0 & \sigma^2_{m,ET} & 0 & 0 \\ 0 & 0 & \sigma^2_{m,Q} & 0 \\ 0 & 0 & 0 & \sigma^2_{m,\Delta S} \end{bmatrix} \tag{3.22}$$

$\sigma^2_{m,P}$ and $\sigma^2_{m,ET}$ have already been derived from Section (3.1.2), and $\sigma^2_{m,\Delta S}$ was provided by the data producer. As previously described in Section (3.1.1.3), the uncertainty of 6.2% and 42.8% were considered for Q. Error covariances among different components were assumed to be 0.

3.2 Second Approach

3.2.1 Fuzzy logic approach

Fuzzy logic has been proven to work effectively against complex structures with uncertain and imprecise measurements [99]–[101]. It uses "degree of membership" rather than the classical "true or false" (1 or 0) approach to define system parameters. Therefore, crisp numbers are converted to fuzzy numbers with fuzzification in the sense that fuzzy number refers to a connected set of possible elements, each with its degree of membership between 0 and 1, rather than a single element. A degree of membership value closer to 1 means that an element is absolutely a member of the fuzzy set, while membership values closer to 0 show that the element is not a member of the fuzzy set. The degree to which a given element belongs to a fuzzy set is defined by the membership function. Various types of membership functions are available: triangular, trapezoidal, piecewise linear, Gaussian, etc. In this study, the triangular fuzzy membership function was selected as it is the most widely used. A triangular fuzzy membership function has the following formulation:

$$\mu_{\tilde{A}}(x) = \begin{cases} 0, & x \leq a \\ (x-a)/(m-a), & a < x \leq m \\ (b-x)/(b-m), & m < x < b \\ 0, & x \geq b \end{cases} \tag{3.23}$$

in which $\mu_{\tilde{A}}(x)$ is the degree of membership of the element x to the fuzzy set $\tilde{A}$. a, b, and m represent the lower value, upper value, and center of the triangular membership function on the x-axis, respectively. Figure 3.3 illustrates the graphical representation of the triangular membership function.

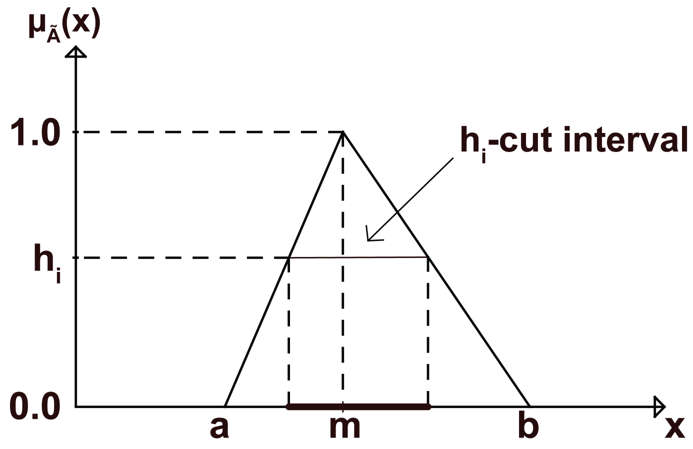

Figure 3.3 : A typical triangular membership function. Bold horizontal line represents the h_i-cut interval.

3.2.2 Symmetric triangular fuzzy linear regression

The fuzzy linear regression (FLR) model used to estimate the behavior of system output is one of the significant subjects of fuzzy logic. The FLR model is given by:

$$Y_i = \tilde{A}_0 x_{i0} + \tilde{A}_1 x_{i1} + \tilde{A}_2 x_{i2} + \ldots\ldots + \tilde{A}_m x_{im} \quad \mathrm{i} = 1,2,\ldots\ldots,\mathrm{n} \tag{3.24}$$

where n is the number of observations of m-dimensional independent variables $x_i = [x_{i0}, x_{i1}, \ldots, x_{im}]^T$, Y_i is the estimated one-dimensional dependent variable and $\tilde{A} = \left[\tilde{A}_0, \tilde{A}_1, \ldots, \tilde{A}_m\right]$ is a vector of the unknown fuzzy coefficients in the form of the symmetric triangular fuzzy number, denoted as $\tilde{A}_j = \left(\alpha_j, c_j\right), j = 0,1,\ldots,m$. Here, α_j and c_j are the center and spread values of the jth fuzzy coefficient, respectively (Figure 3.4(a)). FLR models can be divided into two categories depending on the type of input variables.

1. FLR with crisp independent variables (x_i) and crisp dependent variable (Y_i)

2. FLR with crisp independent variables (x_i) and fuzzy dependent variable ($\tilde{Y}_i$)

In Case-I, dependent variables (x_i) and dependent variable (Y_i) are both crisp numbers, and fuzziness is reflected by the fuzzy coefficients. In Case-II, in addition to fuzzy coefficients, output ($\tilde{Y}_i$) is also a symmetric triangular fuzzy number with center y_i and spread s_i (Figure 3.4(b)). Both cases were considered in the second approach.

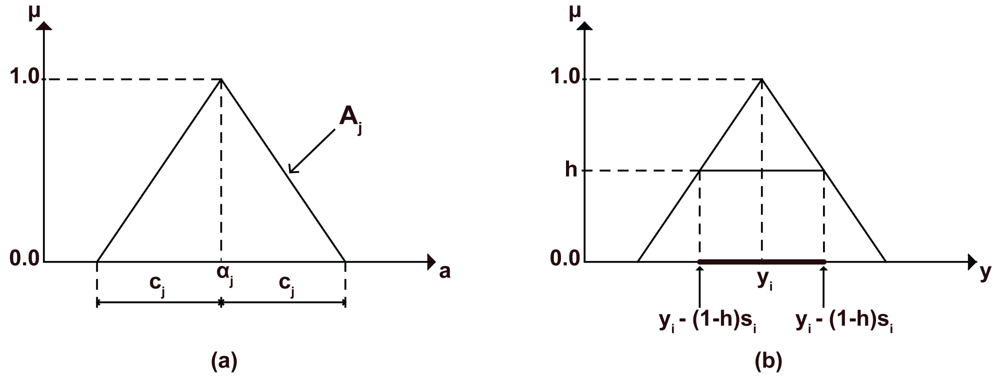

Figure 3.4 : The symmetric triangular fuzzy numbers showing, (a) the fuzzy regression coefficient; (b) the dependent variable. Bold horizontal line (b) represents the h-cut interval of y_i.

As there is no consensus in the literature on the exact value of h, h values (0.5, 0.7, and 0.9) previously offered by two hydrologic studies [25,102] were chosen for this study.

In the following, we described three FLR models that were used in this study.

3.2.2.1 Tanaka model

The first FLR model was developed by [103] to estimate fuzzy coefficients $\tilde{A}_j, j = 0, 1, \ldots, m$ by minimizing the total spread of the estimated intervals, as follows:

$$\min \sum_{i=1}^{n} \sum_{j=0}^{m} c_j \left| x_{ij} \right| \tag{3.25}$$

subject to

$$y_i + (1-h)s_i \leq \sum_{j=0}^{m} \alpha_j x_{ij} + (1-h) \sum_{j=0}^{m} c_j x_{ij} \tag{3.26}$$

$$y_i - (1-h)s_i \geq \sum_{j=0}^{m} \alpha_j x_{ij} - (1-h) \sum_{j=0}^{m} c_j x_{ij} \tag{3.27}$$

$$c_j \geq 0, \quad \alpha_j = \text{ free }, \quad \text{i} = 1, 2, \ldots\ldots, \text{n} \quad j = 0, 1, \ldots, m \tag{3.28}$$

The above conditions force the h-cut estimated intervals to capture the h-cut observed intervals (Figure 3.5(a)). It should be noted that s_i is zero for Case-I as output Y_i is assumed to be a crisp number.

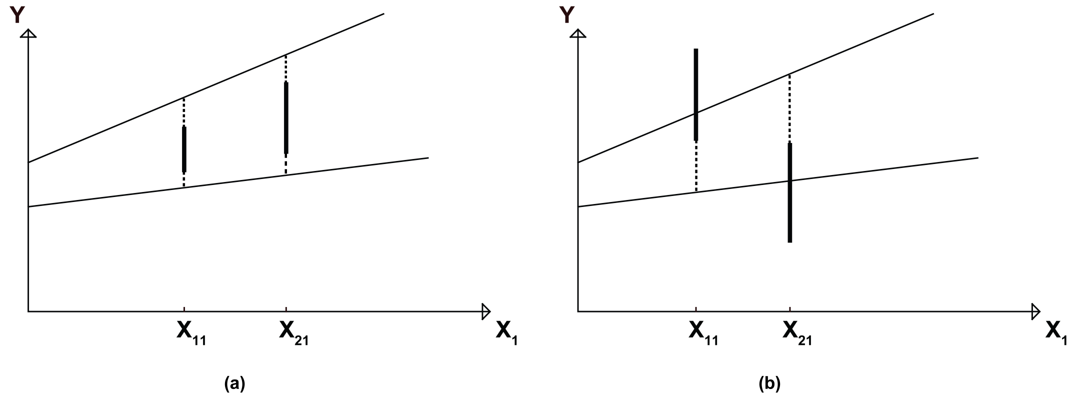

Figure 3.5 : Illustration of (a) Tanaka (b) Hojati FLR models. Bold vertical lines indicate h-cut observed interval. Dotted vertical lines represent the h-cut estimated interval.

3.2.2.2 Hojati model

[104] suggested a FLR model to estimate fuzzy coefficients $\tilde{A}_j, j = 0, 1, \ldots, m$ in such a way that the total distance between the upper value of h-cut estimated interval and the upper value of h-cut observed interval represented as $\left|d_{iU}^{+} - d_{iU}^{-}\right|$, and the distance between lower value of h-cut estimated interval and the lower value of h-cut observed interval shown as $\left|d_{iL}^{+} - d_{iL}^{-}\right|$ are minimized. Therefore, the objective function of the model is formulated as follows:

$$\min \sum_{i=1}^{n} \left(d_{iU}^{+} + d_{iU}^{-} + d_{iL}^{+} + d_{iL}^{-}\right) \tag{3.29}$$

subject to

$$y_i + (1-h)s_i = \sum_{j=0}^{m} \alpha_j x_{ij} + (1-h) \sum_{j=0}^{m} c_j x_{ij} + d_{iU}^{+} - d_{iU}^{-} \tag{3.30}$$

$$y_i - (1-h)s_i \geq \sum_{j=0}^{m} \alpha_j x_{ij} - (1-h) \sum_{j=0}^{m} c_j x_{ij} + d_{iL}^{+} - d_{iL}^{-} \tag{3.31}$$

$$\begin{gathered} c_j \geq 0, \quad d_{iU}^{+}, d_{iU}^{-}, d_{iL}^{+}, d_{iL}^{-} \geq 0, \quad \alpha_j = \text{ free} \\ \text{i} = 1, 2, \ldots\ldots, \text{n} \quad j = 0, 1, \ldots, m \end{gathered} \tag{3.32}$$

Note that for each i, at least one of d_{iU}^{+} and d_{iU}^{-} will be zero, and at least one of d_{iL}^{+} and d_{iL}^{-} will be zero. The estimated intervals can include points that aren't in the observed intervals according to the Hojati model (Figure 3.5(b)). For Case-I, s_i is expected to be zero because output Y_i is a crisp number.

3.2.2.3 Zeng model

[105] proposed a least absolute FLR model to predict fuzzy coefficients $\tilde{A}_j, j = 0, 1, \ldots, m$ by minimizing the overall least absolute distance between estimated values and corresponding observed ones, which is formulated as:

$$\min \sum_{i=1}^{n} (\mu_i + \vartheta_i + \omega_i + \varphi_i) \tag{3.33}$$

subject to

$$y_i = \sum_{j=0}^{m} \alpha_j x_{ij} + \mu_i - \vartheta_i \tag{3.34}$$

$$s_i = \sum_{j=0}^{m} c_j x_{ij} + \omega_i - \varphi_i \tag{3.35}$$

$$\begin{gathered} c_j \geq 0, \quad \mu_i, \vartheta_i, \omega_i, \varphi_i \geq 0, \quad \alpha_j = \text{ free} \\ \mathrm{i} = 1, 2, \ldots\ldots, \mathrm{n} \quad j = 0, 1, \ldots, m \end{gathered} \tag{3.36}$$

where $\mu_i - \vartheta_i$ is the distance between the center of the estimated fuzzy number and the center of the observed fuzzy number. $\omega_i - \varphi_i$ represents the distance between the spread of the estimated fuzzy number and the spread of the observed fuzzy number. The main aim is to minimize the sum of these two distances. h-cut intervals are not defined in the Zeng model. Similar to the other two models, the value of s_i is not taken into a consideration for Case-I as the dependent value is a crisp number.

3.2.3 Uncertainty in WB components

When there are no groundwater and surface water interactions between neighbor basins, the terrestrial WB equation of a basin is simply considered as Equation (1.1). The uncertainty in all WB components must be zero to achieve "perfect closure" (i.e., zero r), but it is highly unlikely for many cases as RS measurements suffer from a significant degree of uncertainty. Therefore, in the second approach, we applied fuzzy correction coefficients to each WB component in order to reduce the magnitude of r.

The following two-step process was used to obtain the correction coefficients: Firstly, annual percentage errors of each budget component for 12 years (2003-2014) were calculated to define the upper bounds error levels. Secondly, three above-mentioned FLR models were applied to estimate fuzzy correction coefficients (Figure 3.6).

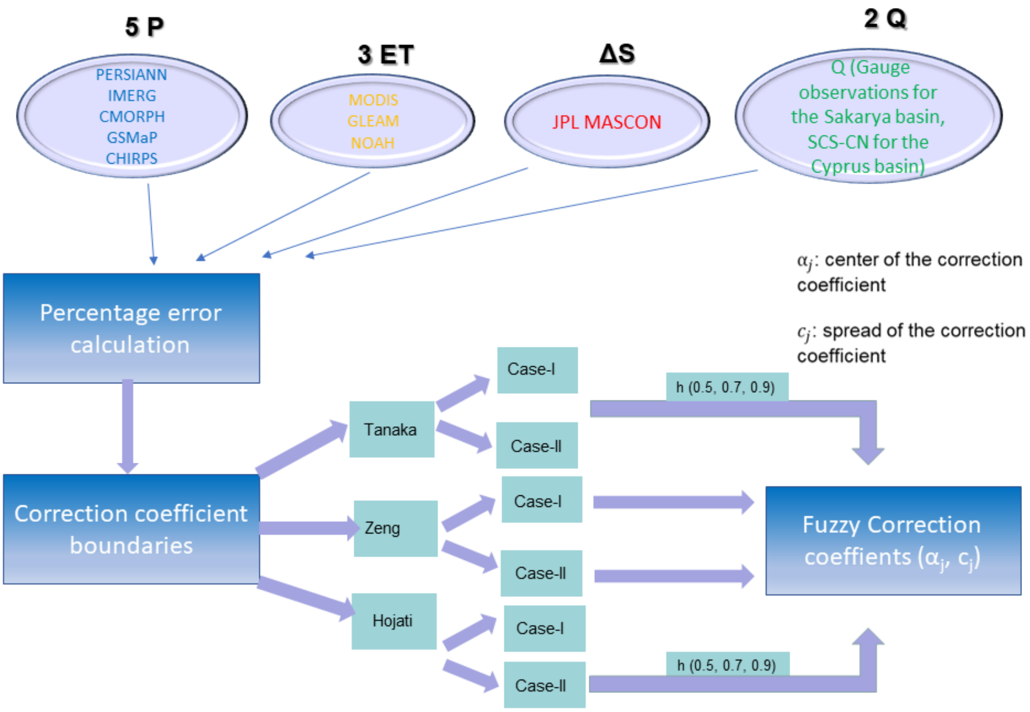

Figure 3.6 : A flow chart of the second approach.

3.2.3.1 Percentage error calculation

The first 12 years (2003-2014) of the annual observations were used in the calibration process to assign correction coefficients for each budget component. The remaining four years were used for validating and testing the model.

Since multiple products were chosen for *ET* and *P*, the same steps were followed for these components to calculate annual percentage errors. Let's consider we have n observations for the same budget component v,$\{v_i\}_i = 1, 2_{,...,n}$, the mean value of all the observations $(\bar{v})$ are:

$$\bar{v} = \frac{1}{n}\sum_{i=1}^{n} v_i \tag{3.37}$$

and the deviation of each observation, which is the absolute difference between corresponding observation and the mean value, is calculated as:

$$\ddot{v}_i = v_i - \bar{v} \tag{3.38}$$

Then, the mean deviation is obtained by:

$$\ddot{v}' = \frac{1}{n}\sum_{i=1}^{n} \ddot{v}_i \tag{3.39}$$

Finally, the percentage error of the budget component for the corresponding year is computed by:

$$P, ET\,\mathrm{error}(\%) = \frac{\ddot{v}'}{\bar{v}} * 100 \tag{3.40}$$

For ΔS, the uncertainty values of MASCON solutions are provided by the JPL. Therefore, the annual percentage errors were obtained by:

$$\Delta S\,\mathrm{error}(\%) = \frac{\mathrm{Uncertainty}}{\mathrm{Observation}} * 100 \tag{3.41}$$

In the second approach, we assumed an error of 10% for Q in the Sakarya basin. . For the Cyprus basin, the mean percentage error value of 25%, previously calculated for SCS-CN based Q by [106], was used.

Tables 3.1-3.2 show the annual WB components for the Sakarya and Cyprus basins, and their corresponding r for the 16 years period. For P and ET, mean values of the multiple RS products are given (monthly and annual time series of WB components averaged over the Sakarya and Cyprus basins are shown in Appendix B). Figure 3.7 shows the mean annual estimates of the P and ET products from 2003 to 2020 for Sakarya and Cyprus basins. The RS-based P estimates differ significantly for both basins, though the order of the P magnitudes in the two basins agrees well. IMERG P estimates are higher than the other P products for both basins. CMORPH has the lowest mean P in the Sakarya basin, and PERSIANN has the lowest mean P in the Cyprus basin. GLDAS estimates the highest ET over the Sakarya basin among the three ET products, whereas GLEAM estimates the highest ET over the Cyprus basin. MODIS has the lowest mean ET in both basins.

The annual percentage error values of the four WB components, and some key statistics are also presented in Tables 3.3-3.4 for two basins. It is clearly seen that the Cyprus basin has higher percentage error values than the Sakarya basin for all components, especially for ΔS. This could be because the Cyprus basin has relatively small spatial coverage and RS products with a smaller spatial resolution (0.5°, 0.25°) exceed the boundaries of the Cyprus basin (Figure 2.1(b)). The JPL MASCON solutions used

Table 3.1 : Estimated annual WB components of the Sakarya basin for 16 years.

Year	P (mm)	Q (mm)	ET (mm)	ΔS (mm)	r (mm)
2003	381.37	70.54	388.64	22.68	-100.49
2004	343.69	93.59	409.79	-80	-79.7
2005	417.06	68.97	447.89	40.83	-140.63
2006	389.23	76.79	417.11	-72.76	-31.91
2007	423.47	49.04	382.54	34.24	-42.34
2008	337.9	52.01	392.59	-29.66	-77.04
2009	473.18	84.76	445.13	95.34	-152.04
2010	542.1	99.4	451.09	-37.97	29.57
2011	403.09	86.17	460.35	6.77	-150.2
2012	425.18	92.65	420.9	42.02	-130.38
2013	356.69	74.68	419.08	-126.47	-10.6
2014	484.37	54.17	465.62	124.36	-159.78
2015	520.62	122	530.54	-104.19	-27.73
2016	424.53	78	455.96	4.61	-114.03
2019	455.47	78.04	478.37	-61.02	-39.93
2020	375.97	69.21	456.16	-88.82	-60.58

Table 3.2 : Estimated annual WB components of the Cyprus basin for 16 years.

Year	P (mm)	Q (mm)	ET (mm)	ΔS (mm)	r (mm)
2003	371.55	19.65	464.45	24.05	-136.6
2004	411.82	35.43	406.63	-67.1	36.86
2005	278.52	9.51	411.03	-4.41	-137.6
2006	285.95	16.96	410.45	29.83	-171.3
2007	376.96	39.17	404.8	8.18	-75.2
2008	198.5	4.87	338.27	-35.16	-109.48
2009	436.47	13.07	424.45	108.64	-109.69
2010	333.05	56.87	413	-33.54	-103.28
2011	360.65	10.85	448.01	-73.87	-24.33
2012	512.58	10.77	465.41	88.82	-52.42
2013	221.58	0.98	424.88	-39.69	-164.6
2014	303.01	6	397.5	-69.02	-31.47
2015	366.32	3.2	457.5	86.71	-181.09
2016	299.51	11.02	362.49	-43.1	-30.89
2019	520.5	21.99	476.24	-58.98	81.25
2020	388.25	9.34	428.19	53.13	-102.41

for ΔS have the lowest spatial resolution among others. Since there is no RS-based ΔS product with a higher spatial resolution, the largest errors were observed for ΔS in the Cyprus basin. Also, ΔS estimations face leakage error due to across ocean/land boundary.

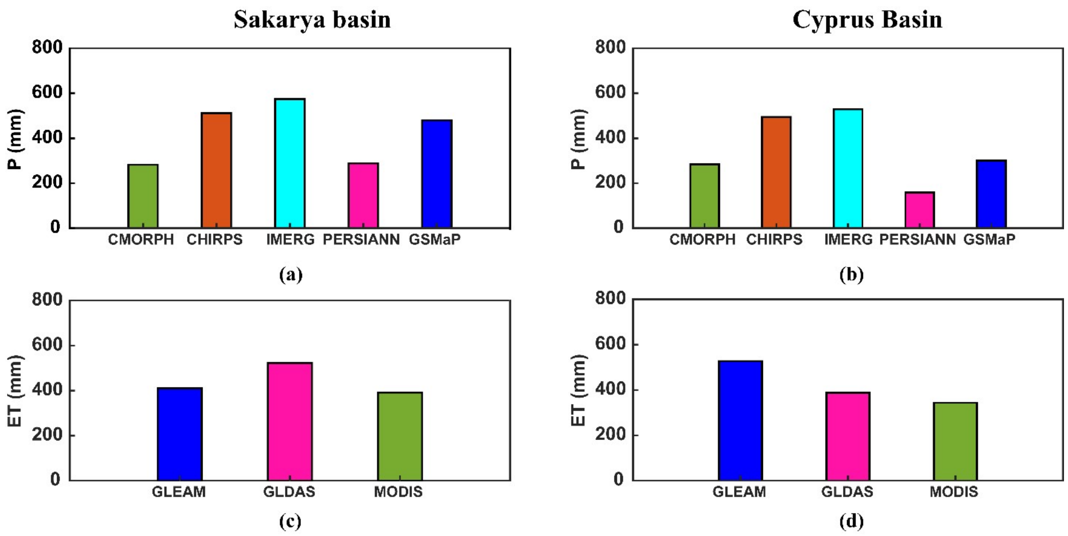

Figure 3.7 : Mean annual P and ET estimates in Sakarya and Cyprus basins.

Table 3.3 : Percentage error values of WB components in the Sakarya basin at annual scale.

Year	$P(\%)$	$Q(\%)$	$ET(\%)$	$\Delta S(\%)$
2003	34.89	10	9.17	47.66
2004	31.44	10	13.93	32.81
2005	39.03	10	10.97	49.38
2006	26.95	10	10.6	48.88
2007	14.57	10	13.24	43.05
2008	26.9	10	15.65	42.84
2009	28.31	10	13.04	55.43
2010	24.16	10	13.52	41.54
2011	27.17	10	7.72	42.45
2012	39.53	10	12.88	35.86
2013	17.32	10	14.2	30.45
2014	26.24	10	16.75	53.49
Mean	28.04	10	12.64	43.29
St.dev (σ)	7.56	0	2.6	8.08
0	Percentage error (%)			60

3.2.3.2 Correction coefficient criteria and error boundaries

If the WB components have "perfect" measurements, the correction coefficient would be "one" for each component. As this is not possible for many cases, the primary goal of this study is applying fuzzy correction coefficients, $\tilde{A}_{j,j=P,Q,ET,\Delta S} = (\alpha_j, c_j)$, to each component of the WB equation to minimize r in Sakarya and Cyprus basins. α_j represents the center of the fuzzy correction coefficient numbers assigned to WB

Table 3.4 : Percentage error values of WB components in the Cyprus basin at annual scale.

Year	$P(\%)$	$Q(\%)$	$ET(\%)$	$\Delta S(\%)$
2003	40.86	25	18.01	125.06
2004	47.25	25	15.83	145.42
2005	40.86	25	18.25	214.97
2006	38.62	25	18.87	103.54
2007	23.65	25	16.45	110.83
2008	36.1	25	15.67	93.3
2009	38.19	25	16.12	106.02
2010	41.51	25	16.48	58.76
2011	40.76	25	17.48	103.14
2012	31.62	25	19.22	112.15
2013	44.27	25	17.43	92.16
2014	36.61	25	21.46	109.74
Mean	38.36	25	17.61	113.64
St.dev (σ)	6.12	1.69	39.32	8.08
0	Percentage error (%)			240

components. c_j represents the spread of the fuzzy correction coefficient numbers assigned to WB components. Therefore, Equation (1.1) can be rewritten as

$$\tilde{A}_P P - \tilde{A}_Q Q - \tilde{A}_{ET} ET - \tilde{A}_{\Delta S} \Delta S = \hat{r} \tag{3.42}$$

where $\hat{r}$ is the revised WB error after FLR.

Constraint boundaries in the three FLR models should be well defined, and there are several criteria to determine the boundaries of the Equations (3.28),(3.32), and (3.36). Two important statistics (mean and standard deviation) of the percentage errors illustrated in Tables 3.3-3.4 were used as decision criteria to define constraint boundaries for both basins. The mean of the percentage errors plus one standard deviation was considered to indicate the deviation of α_j from "one" and the mean of the percentage errors plus three times the standard deviations was considered to indicate the minimum boundary of c_j [25]. From a statistical point of view, 68.3% and 99.7% of the normally distributed data fall within one and three standard deviations of the mean, respectively. Table 3.5 shows the considered boundaries for α_j and c_j fuzzy coefficients of each WB component for the Sakarya and Cyprus basins. s_ε is the standard deviation of the estimated r values, given in Tables 3.1-3.2, between 2003 and

2014 for both basins. As the Cyprus basin has higher percentage error values than the Sakarya basin for all components (Tables 3.3-3.4), constraint boundaries considered for the Cyprus basin are wider than those of the Sakarya basin. The minimum boundary of the $\alpha_{\Delta S}$ was computed negative in the Cyprus basin since there are large percentage error values for ΔS. However, negative $\alpha_{\Delta S}$ is not possible, so the negative value was readjusted to zero.

Table 3.5 : Considered boundaries for α_j and c_j fuzzy coefficients of each WB component in both basins.

Fuzzy coefficient	P	Q	ET	ΔS
Sakarya basin				
α_j	$0.644 \leq \alpha_P \leq 1.356$	$0.900 \leq \alpha_Q \leq 1.100$	$0.848 \leq \alpha_{ET} \leq 1.152$	$0.486 \leq \alpha_{\Delta S} \leq 1.514$
c_j	$c_P \geq 0.507$	$c_Q \geq 0.100$	$c_{ET} \geq 0.205$	$c_{\Delta S} \geq 0.675$
s_ε=62.57 mm				
Cyprus basin				
α_j	$0.555 \leq \alpha_P \leq 1.445$	$0.750 \leq \alpha_Q \leq 1.250$	$0.807 \leq \alpha_{ET} \leq 1.193$	$0 \leq \alpha_{\Delta S} \leq 2.530$
c_j	$c_P \geq 0.567$	$c_Q \geq 0.250$	$c_{ET} \geq 0.227$	$c_{\Delta S} \geq 2.316$
s_ε=62.54 mm				

3.2.3.3 Adapting FLR models to the WB equation

Three FLR models with two cases were chosen for this study, as described in Section (3.2.2). Also, three different h-cut values, 0.5, 0.7, 0.9, were considered for Tanaka and Hojati FLR models.

Referring to the Equations (3.25-3.28), Tanaka FLR model for WB of the Sakarya and Cyprus basins is formulated as:

$$\min \sum_{i=1}^{12} c_P\left|P_i\right| + c_Q\left|Q_i\right| + c_{ET}\left|ET_i\right| + c_{\Delta S}\left|\Delta S_i\right| \tag{3.43}$$

subject to

$$\begin{aligned} &\varepsilon_i + (1-h)s_{\varepsilon_i} \leq \left[\alpha_P\left(P_i\right) - \alpha_Q\left(Q_i\right) - \alpha_{ET}\left(ET_i\right) - \alpha_{\Delta S}\left(\Delta S_i\right)\right] + \\ &(1-h)\left[c_P\left(P_i\right) - c_Q\left(Q_i\right) - c_{ET}\left(ET_i\right) - c_{\Delta S}\left(\Delta S_i\right)\right] \end{aligned} \tag{3.44}$$

$$\begin{aligned} &\varepsilon_i - (1-h)s_{\varepsilon_i} \geq \left[\alpha_P\left(P_i\right) - \alpha_Q\left(Q_i\right) - \alpha_{ET}\left(ET_i\right) - \alpha_{\Delta S}\left(\Delta S_i\right)\right] - \\ &(1-h)\left[c_P\left(P_i\right) - c_Q\left(Q_i\right) - c_{ET}\left(ET_i\right) - c_{\Delta S}\left(\Delta S_i\right)\right] \end{aligned} \tag{3.45}$$

$$\text{i} = 1, 2, \ldots\ldots, 12$$

where ε_i is the observed r for the corresponding year. ε_i is considered as symmetric triangular fuzzy number with center zero and spread s_{ε_i}. For Case-I, s_{ε_i} is zero since ε_i

is a crisp number. For Case-II, s_{ε_i} is considered equal to s_ε (Table 3.5). Boundaries of α_j and c_j are taken from Table 3.5 for both basins.

Referring to the Equations (3.29-3.32), Hojati FLR model for WB of the Sakarya and Cyprus basins can be expressed as follows:

$$\min \sum_{i=1}^{12} \left(d_{iU}^{+} + d_{iU}^{-} + d_{iL}^{+} + d_{iL}^{-}\right) \tag{3.46}$$

subject to

$$\begin{aligned} &\varepsilon_i + (1-h)s_{\varepsilon_i} = \left[\alpha_P\left(P_i\right) - \alpha_Q\left(Q_i\right) - \alpha_{ET}\left(ET_i\right) - \alpha_{\Delta S}\left(\Delta S_i\right)\right] + \\ &(1-h)\left[c_P\left(P_i\right) - c_Q\left(Q_i\right) - c_{ET}\left(ET_i\right) - c_{\Delta S}\left(\Delta S_i\right)\right] + d_{iU}^{+} - d_{iU}^{-} \end{aligned} \tag{3.47}$$

$$\begin{aligned} &\varepsilon_i - (1-h)s_{\varepsilon_i} = \left[\alpha_P\left(P_i\right) - \alpha_Q\left(Q_i\right) - \alpha_{ET}\left(ET_i\right) - \alpha_{\Delta S}\left(\Delta S_i\right)\right] - \\ &(1-h)\left[c_P\left(P_i\right) - c_Q\left(Q_i\right) - c_{ET}\left(ET_i\right) - c_{\Delta S}\left(\Delta S_i\right)\right] + d_{iL}^{+} - d_{iL}^{-} \end{aligned} \tag{3.48}$$

$$d_{iU}^{+}, d_{iU}^{-}, d_{iL}^{+}, d_{iL}^{-} \geq 0, \quad \mathrm{i} = 1, 2, \ldots\ldots, 12 \tag{3.49}$$

in which $\left|d_{iU}^{+} - d_{iU}^{-}\right|$ is the distance between the upper value of h-cut estimated WB r interval and the upper value of h-cut observed r interval. Similarly, $\left|d_{iL}^{+} - d_{iL}^{-}\right|$ is the distance between the lower value of h-cut estimated WB r interval and the upper value of h-cut observed r interval. The definitions of the variables used in Case-I and Case-II are the same as those used in the Tanaka WB model.

Referring to the Equations (3.33-3.36), the following Zeng FLR formulation can be written for WB of the Sakarya and Cyprus basins.

$$\min \sum_{i=1}^{n} \left(\mu_i + \vartheta_i + \omega_i + \varphi_i\right) \tag{3.50}$$

$$\varepsilon_i = \left[\alpha_P\left(P_i\right) - \alpha_Q\left(Q_i\right) - \alpha_{ET}\left(ET_i\right) - \alpha_{\Delta S}\left(\Delta S_i\right)\right] + \mu_i - \vartheta_i \tag{3.51}$$

$$s_{\varepsilon_i} = \left[c_P\left(P_i\right) - c_Q\left(Q_i\right) - c_{ET}\left(ET_i\right) - c_{\Delta S}\left(\Delta S_i\right)\right] + \omega_i - \varphi_i \tag{3.52}$$

$$s_{\varepsilon_i} = 56.22 \text{ mm}, \quad \mu_i, \vartheta_i, \omega_i, \varphi_i \geq 0, \quad \mathrm{i} = 1, 2, \ldots\ldots, 12 \tag{3.53}$$

where $|\mu_i - \vartheta_i|$ is the distance between the center of estimated WB r and the center of observed WB r. $|\omega_i - \varphi_i|$ is the distance between the spread of estimated WB r and the spread of observed WB r. The definitions of the variables used in Case-I and Case-II are the same as those used in Tanaka and Hojati models. However, the Zeng model does not include h-cut intervals.

3.3 Comparison and Evaluation Metrics

Six performance metrics were used, namely the mean absolute error (MAE), the root mean square error (RMSE), the Kling-Gupta efficiency (KGE), the bias, the percent bias (PBIAS), and the correlation coefficient (CC). The equations of each metric are as follows:

$$MAE = \frac{\sum_{i=1}^{n} \mid \left(V_{est,i} - V_{obs,i} \mid\right.}{n} \tag{3.54}$$

$$RMSE = \sqrt{\frac{\sum_{i=1}^{n} \left(V_{est,i} - V_{obs,i}\right)^2}{n}} \tag{3.55}$$

$$KGE = 1 - \sqrt{(1-CC)^2 + (1-\beta)^2 + (1-\alpha)^2} \text{ where } \alpha = \frac{\sigma_{est}}{\sigma_{obs}}, \beta = \frac{\mu_{est}}{\mu_{obs}} \tag{3.56}$$

$$\text{bias} = \frac{\sum_{i=1}^{n} \left(V_{est,i} - V_{obs,i}\right)}{n} \tag{3.57}$$

$$PBIAS = \frac{\sum_{i=1}^{n} \left(V_{est,i} - V_{obs,i}\right)}{\sum_{i=1}^{n} \left(V_{obs,i}\right)} X100 \tag{3.58}$$

$$CC = \frac{\sum_{i=1}^{n} \left(V_{est,i} - \overline{V_{est}}\right)\left(V_{obs,i} - \overline{V_{obs}}\right)}{\sqrt{\sum_{i=1}^{n} \left(V_{est,i} - \overline{V_{est}}\right)^2 \sum_{i=1}^{n} \left(V_{obs,i} - \overline{V_{obs}}\right)^2}} \tag{3.59}$$

where $V_{est,i}$ and $V_{obs,i}$ are the estimated and observed data, respectively. n is the total number of years during the study period. μ_{obs} and μ_{est} are the mean of the observations and estimations, respectively. σ_{obs} and σ_{est} are the standard deviation of the observations and estimations, respectively. The optimal values of the five performance metrics, namely MAE, RMSE, KGE, bias, PBIAS, and CC, are 0, 0, 1, 0, 0%, and 1, respectively.

In the first approach, bias, RMSE, and CC were used to compare RS-based P estimations, while MAE, RMSE, KGE, PBIAS, and CC were used to compare FLR outputs in the second approach.

4. RESULTS

4.1 First Approach

4.1.1 Uncertainty assessment of data products

4.1.1.1 Uncertainties in *P* products

The time series of the *P* derived from four RS-based *P* products and product error metrics over the Sakarya basin during the study period were shown in Figure 4.1. *P* products followed a similar temporal pattern; however, they performed reasonably better in the July-December period than in the January-June. High monthly *P* occurs in winter, and low monthly *P* occurs in summer. The annual mean *P* is 730.0 mm for TRMM, 472.7 mm for GPCP, 286.9 mm for PERSIANN, 283.1 mm for CMORPH, and 427.2 mm for gauge measurements. TRMM (Bias = 25.2 mm/month) and GPCP (Bias = 3.8 mm/month) overestimated gauge *P*, whereas PERSIANN (Bias= -11.7 mm/month) and CMORPH (Bias = -12.0 mm/month) showed underestimation. [67] showed that PERSIANN and CMORPH underestimated *P* with a bias value of 0.12 mm/day and 0.07 mm/day for the Meichuan basin in China, respectively. The underestimation of P by PERSIANN and CMORPH were also reported in [107]. TRMM has the highest RMSE with a value of 39.22 mm/month, followed by the GPCP (26.16 mm/month), CMORPH (25.16 mm/month), and PERSIANN (23.67 mm/month). This shows that PERSIANN outperformed other products in capturing the *P* magnitude during the study period. However, it should be mentioned that bias has a significant impact on RMSE. The TRMM's poor RMSE performance was mainly due to high bias. Additionally, TRMM has the highest CC value of 0.68, indicating the best linear agreement with the gauge *P*. The CC values of GPCP, PERSIANN, and CMORPH are 0.49, 0.56, and 0.48, respectively.

Bias removal decreased the RMSE of four RS-based products, except PERSIANN. The RMSE of BC-TRMM, BC-CMORPH, BC-GPCP, and BC-PERSIANN was calculated as 14.05 mm/month, 15.32 mm/month, 16.98 mm/month, and 24.15 mm/month, respectively. The boxplots of the four BC *P* products over the Sakarya basin (Figure 4.2) indicate all BC product medians being close to each other. The median *P* is lowest for the BC-PERSIANN (25.71 mm/month), whereas BC-TRMM has the highest median *P* (35.90 mm/month). BC-GPCP median *P* (31.79 mm/month) is closest to the Gauge *P* median (31.55 mm/month). The range of *P* is greatest in BC-PERSIANN and smallest in BC-TRMM. This indicates that BC-PERSIANN has high variability of *P*, whereas BC-TRMM has less variability of *P* over the Sakarya basin.

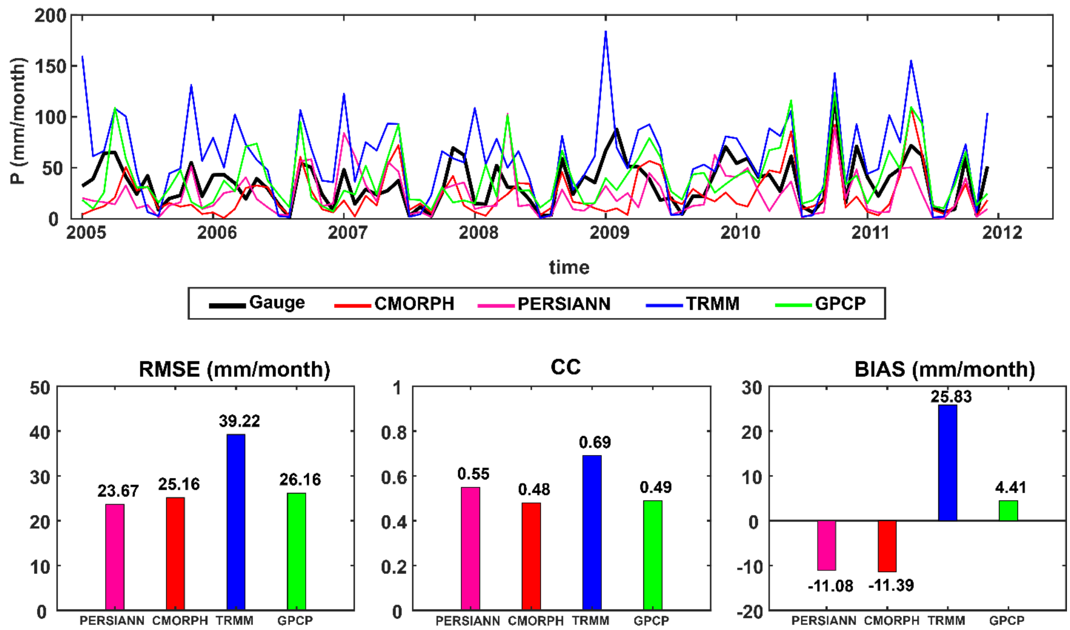

Figure 4.1 : Time series of the *P* derived from four RS-based *P* products and product error metrics over the Sakarya basin.

4.1.1.2 Uncertainties in *ET* products

The annual mean *ET* is 364.3 mm for MODIS, 391.2 mm for GLEAM, 487.0 mm for NTSG, 302.1 mm for VIC, 505.2 mm for NOAH, and 417.5 mm for TERRACLIMATE (Figure 4.3(a)). High monthly *ET* values were observed in hot seasons, while low monthly *ET* values were observed in cold seasons. The seasonal pattern of *ET* products, except TERRACLIMATE, is generally consistent with each other. Peak *ET* values for TERRACLIMATE were recorded in the spring, whereas peak *ET* for other products was observed in the summer. Figure 4.3(b) shows the boxplots of the

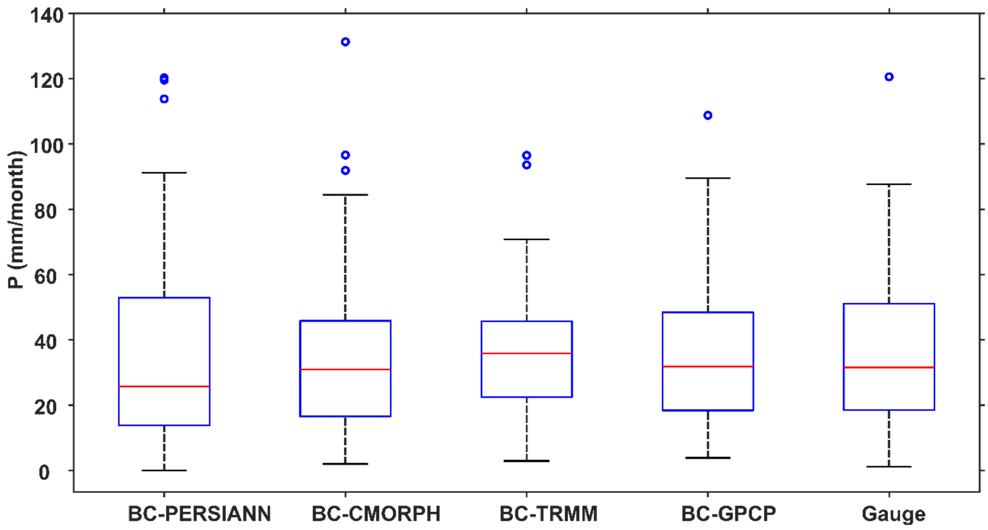

Figure 4.2 : The boxplots of the four BC P products over the Sakarya basin. The bottom and top edges of each box are the first (Q1) and third (Q3) quartiles, respectively. The range between the two quartiles is called the interquartile range (IQR). The horizontal red line in the box indicates the median, and the whiskers extend to the minimum and maximum range of data not considered outliers. The data points exceeding Q1-1.5×IQR or Q3+1.5×IQR indicate the outliers, shown by blue marks.

six ET products over the Sakarya basin. VIC has the lowest median ET with 18.89 mm/month, whereas NTSG has the highest median ET with 36.80 mm/month. The range of ET is smallest in MODIS, indicating that MODIS has less variability of ET over the Sakarya basin.

Table 4.1 shows the GTCH-based monthly uncertainties of ET products over the Sakarya basin. Most products generally perform better in cooler seasons (from November to February) than in hot seasons (from March to October). This might be because ET estimations have larger magnitudes in warmer months. Overall, the monthly uncertainties in ET products vary from 0.89 mm/month to 15.62 mm/month. The mean monthly ET uncertainties are lowest in LSMs (2.76–3.72 mm/month), moderate in RS-based products (3.27–4.67 mm/month), and highest in a reanalysis product (9.28 mm/month). VIC LSM has the lowest mean monthly ET uncertainty (2.76 mm/month). In contrast, TERRACLIMATE reanalysis product has the highest mean monthly ET uncertainty (9.28 mm/month).

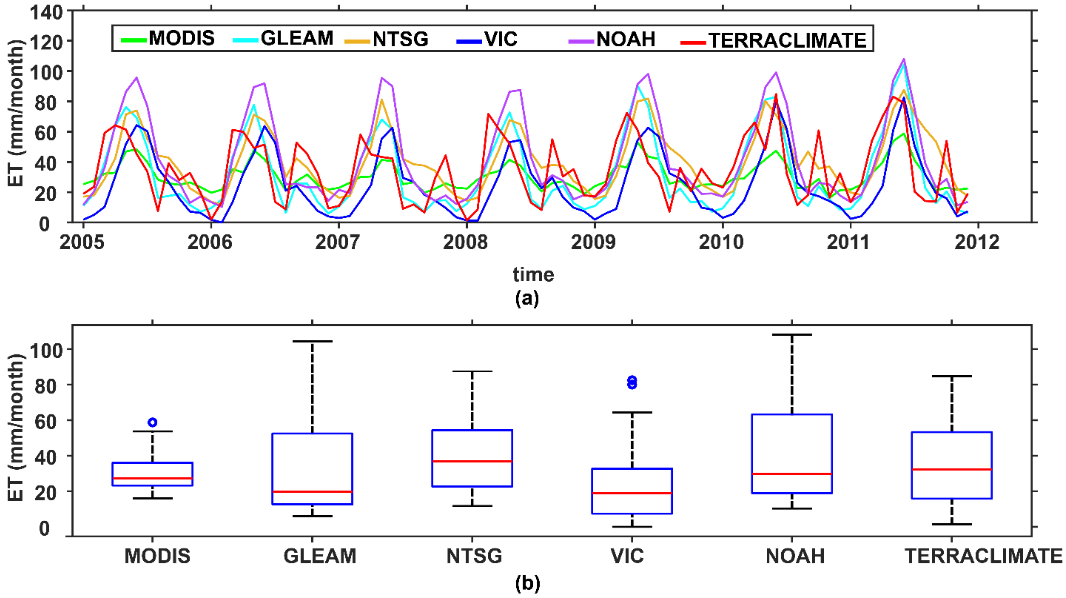

Figure 4.3 : (a) Time series of the six ET products during the study period, (b) Boxplot distributions of the six ET products.

Table 4.1 : The uncertainties of six ET products with the GTCH method.

	MODIS	GLEAM	NTSG	VIC	NOAH	TERRACLI MATE
January	1.42	1.71	1.47	1.14	3.41	7.66
February	1.62	2.79	1.33	1.64	3.33	7.87
March	4.98	2.24	2.44	1.28	2.43	5.38
April	2.97	2.32	4.32	3.2	4.87	7.39
May	2.69	5.29	6.33	4.14	4.52	10.67
June	4.51	9.76	7.46	3.75	4	13.56
July	5.79	8.39	6.35	4.98	5.17	6.15
August	2.47	2.14	7.23	2.5	4.59	4.97
September	3.12	3.96	9.09	2.31	2.87	15.62
October	2.09	1.97	3.14	4.8	4.1	13.93
November	4.31	1.37	4.74	2.43	3.92	12.13
December	3.29	1.88	2.18	0.89	1.39	6.07
	0	Uncertainty (mm/month)				16

4.1.1.3 Uncertainties in JPL ΔS

Figure 4.4 shows the monthly variations of JPL ΔS and its uncertainties over the Sakarya basin. The distinct seasonality was observed for JPL ΔS, in which negative values occurred in summer and positive values occurred in winter. Overall, the monthly JPL ΔS ranges from -80.98 mm/month to 79.45 mm/month. There is no seasonality in product uncertainty, and the level of uncertainty is nearly constant during the study period. The mean monthly uncertainty was calculated as 26.78 mm/month.

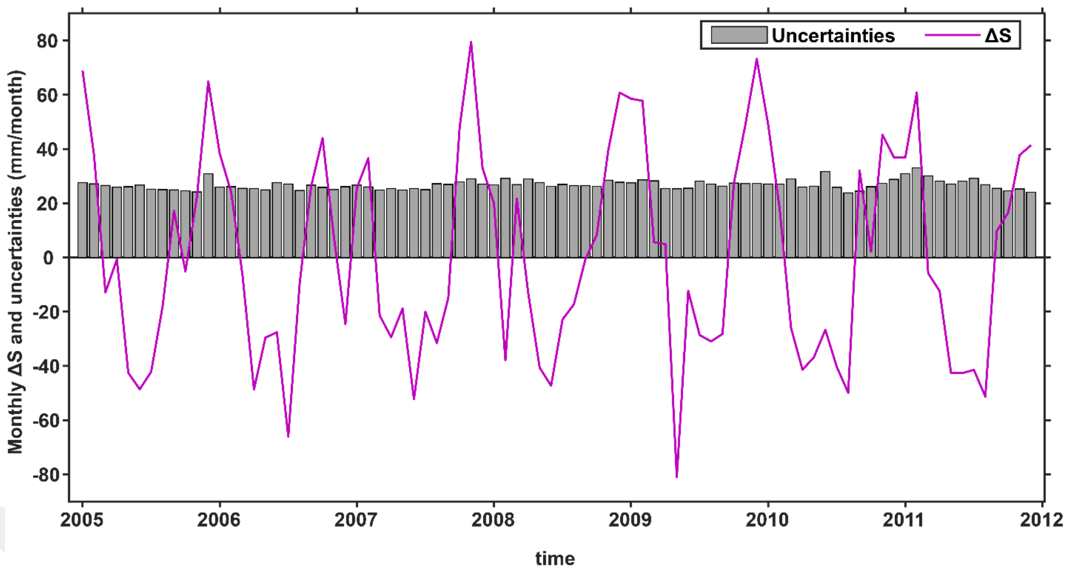

Figure 4.4 : The monthly variations of JPL ΔS and its uncertainties over the Sakarya basin.

4.1.2 Merging of P and ET estimations

For P, the mean monthly merging weights of BC-CMORPH, BC-TRMM, BC-GPCP, and BC-PERSIANN are 32%, 31%, 25%, and 12%, respectively (Figure 4.5(a)). The monthly merging weights of BC-TRMM range from 16% to 59%. BC-TRMM performed better than the other P products in the summer and spring seasons. The monthly merging weights of BC-CMORPH range from 15% to 44%, and it has the best performance in autumn with a mean merging weight of 43%. BC-GPCP has the highest merging weight in winter (34%). The overall performance of BC-PERSIANN is worse than other products, indicating that it has a higher deviation from the gauge data than other P products. The merged P remarkably captures the seasonal cycle of the gauge observations (Figure 4.6(c)). Compared to RS-based P products, merged P has the best consistency with the gauge observations, with the lowest RMSE (10.48 mm/month) and the highest CC (0.89).

As described in Section 4.1.2, VIC and TERRACLIMATE are the least and most uncertain ET products over the Sakarya basin, respectively (Figure 4.5(b)). Therefore, VIC has the greatest mean monthly merging weight, while TERRACLIMATE has the lowest. The mean monthly merging weights of the six ET products, namely MODIS, GLEAM, NTSG, VIC, NOAH, and TERRACLIMATE, are 20%, 22%, 12%, 29%, 14%, and 3%, respectively. The distinct seasonality was observed for merged ET, in which high ET values occurred in summer and low ET values occurred in winter (Figure 4.6(d)).

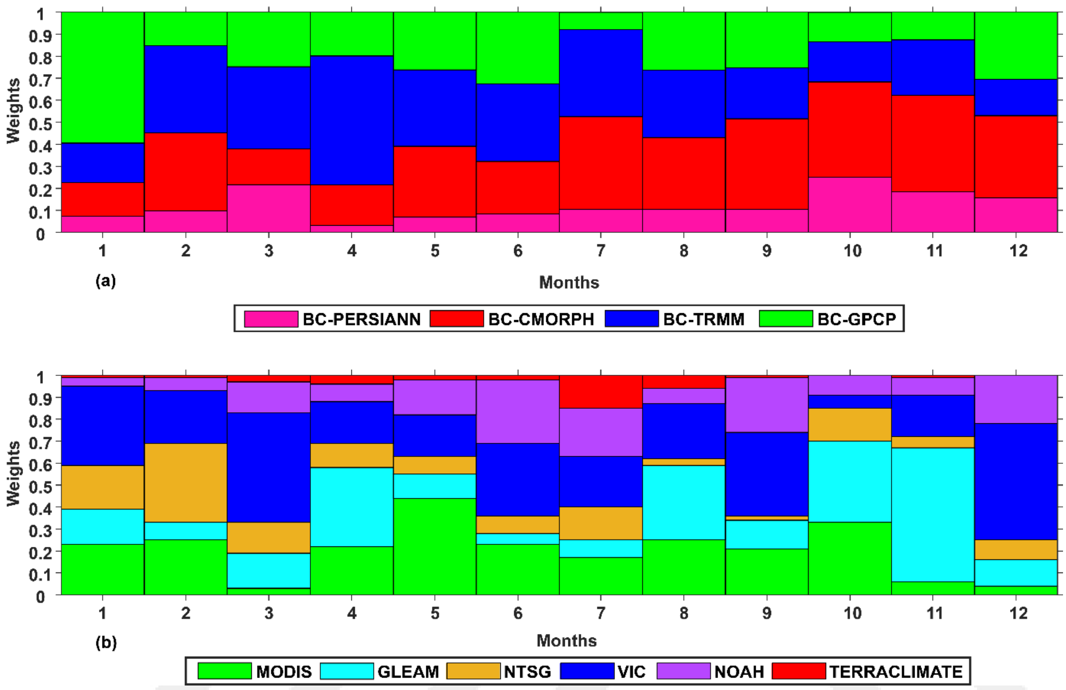

Figure 4.5 : Merging weights, assigned to four P and six ET products.

4.1.3 Residual error and CKF

The estimated monthly values of WB components and residual errors for the unconstrained system are shown in the left column of Figures 4.7-4.8. The unconstrained WB components are merged P and ET products, JPL ΔS , and gauge Q data. Q is relatively small compared to other components. The unconstrained system residual error values vary between -65 and 78 mm/month. These residual error values were then distributed among WB components based on their relative uncertainties using CKF. As a result, the "perfect" WB estimates were obtained, zeroing the residual errors.

The CKF was applied to WB components using two different uncertainty values of Q (6.2% and 42.8%). The results of the constrained system with a Q uncertainty value of 6.2% are presented in the right column of Figure 4.7. When CKF estimates are

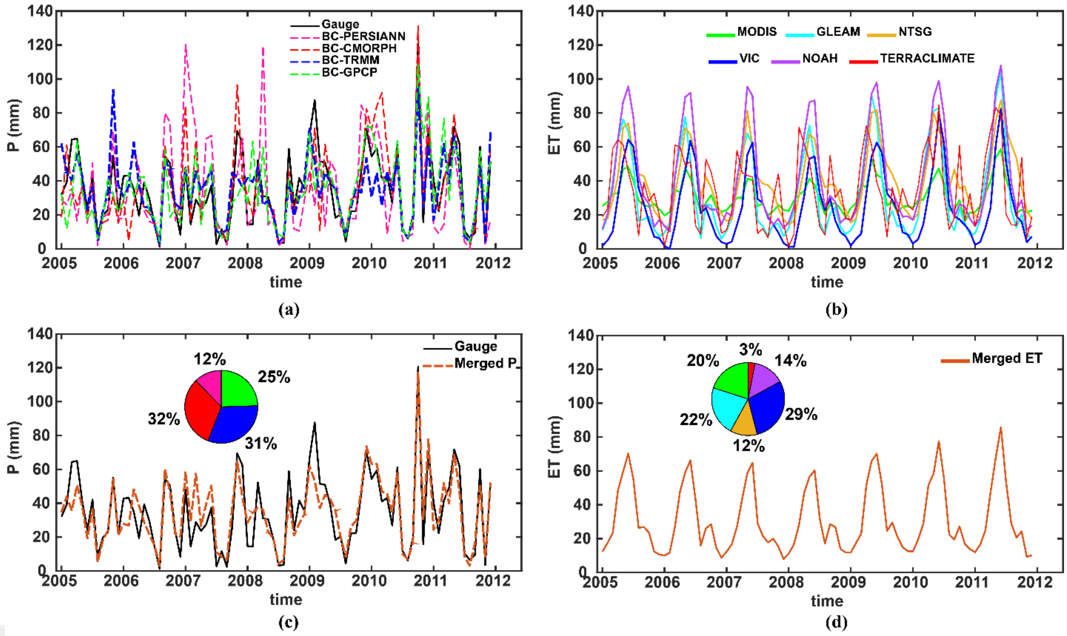

Figure 4.6 : The first row (a,b) shows the time series of P and ET products during the study period. The second row (c,d) shows the merged estimations. Pie charts indicate the mean merging weights of each product.

compared to unconstrained ones, ΔS is the most altered WB component, as shown in Figure 4.7(b,d). Although the magnitudes of ΔS changed significantly after CKF, the seasonal pattern was conserved. The pie chart in Figure 4.7(f) shows that ΔS has the largest non-closure error attribution with a mean error attribution of 93%, followed by P (7%). This is mainly caused by the two facts. First, the Sakarya basin is a relatively small basin that GRACE can not simply resolve. Second, while P, ET, and Q mostly describe the surface water dynamics, ΔS incudes both the surface water and ground water. It is well known that surface water and ground water have completely different dynamic behaviours. The change in surface water is much faster than the change in groundwater.

The right column of Figure 4.8 shows the results of the constrained system with a Q uncertainty value of 42.8%. ΔS is again the most altered component of the WB (Figure 4.8 (b,d)). With a mean error attribution of 92% (Figure 4.8(f)), ΔS has the highest non-closure error attribution, followed by P (7%) and Q (1%). Comparing the two CKF estimates in Figures 4.7-4.8, it was found that the change in Q uncertainty had only a negligible impact on results. It can be concluded that the CKF estimates are insensitive to the different levels of Q uncertainty values.

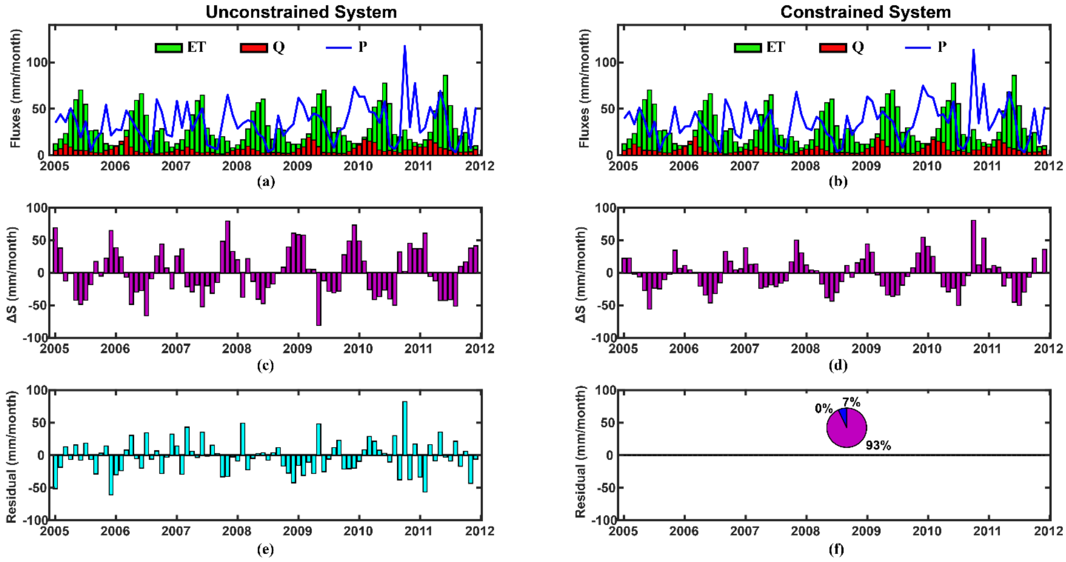

Figure 4.7 : The unconstrained (a, c, e) and constrained (b, d, f) systems. The first two row shows the time series of water budget variables in unconstrained and constrained systems. The last row indicates the residual error values of the two systems. Q uncertainty of 6.2% was considered for the constrained system.

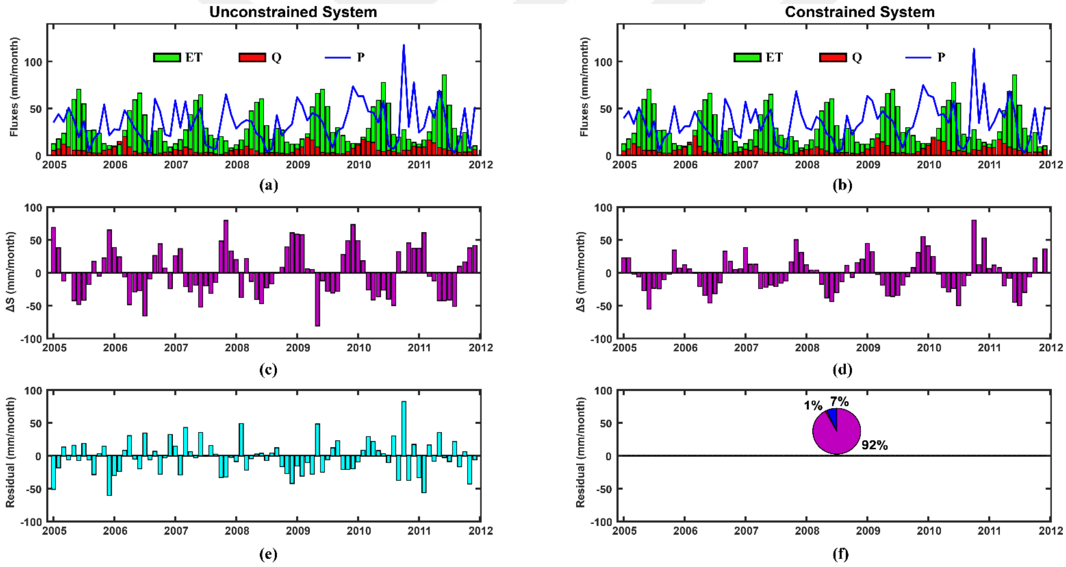

Figure 4.8 : The unconstrained (a, c, e) and constrained (b, d, f) systems. The first two row shows the time series of water budget variables in unconstrained and constrained systems. The last row indicates the residual errors of the two systems. Q uncertainty of 42.8% was considered for the constrained system.

We further compared CKF P output (CKF-P) with various P estimates. The CKF-P output, which is assumed to have 6.2% Q uncertainty, was used for comparison since the CKF outputs generated using different Q uncertainty values are nearly the same. Figure 4.9 shows the comparison of monthly CKF-P, the ensemble mean, merged

P, and the four BC-P products with gauge observations using the Taylor diagram. Compared to other P estimates, CKF-P is closer to the gauge observations. The CKF-P output has higher CC and lower root mean square deviation (RMSD) than other products. The RMSD of CKF-P output is 9.95 mm/month, which is 5.06% lower than the RMSD of 10.48 mm/month from the merged P, and 29.18% lower than the RMSD of 14.05 mm/month from the ensemble mean.

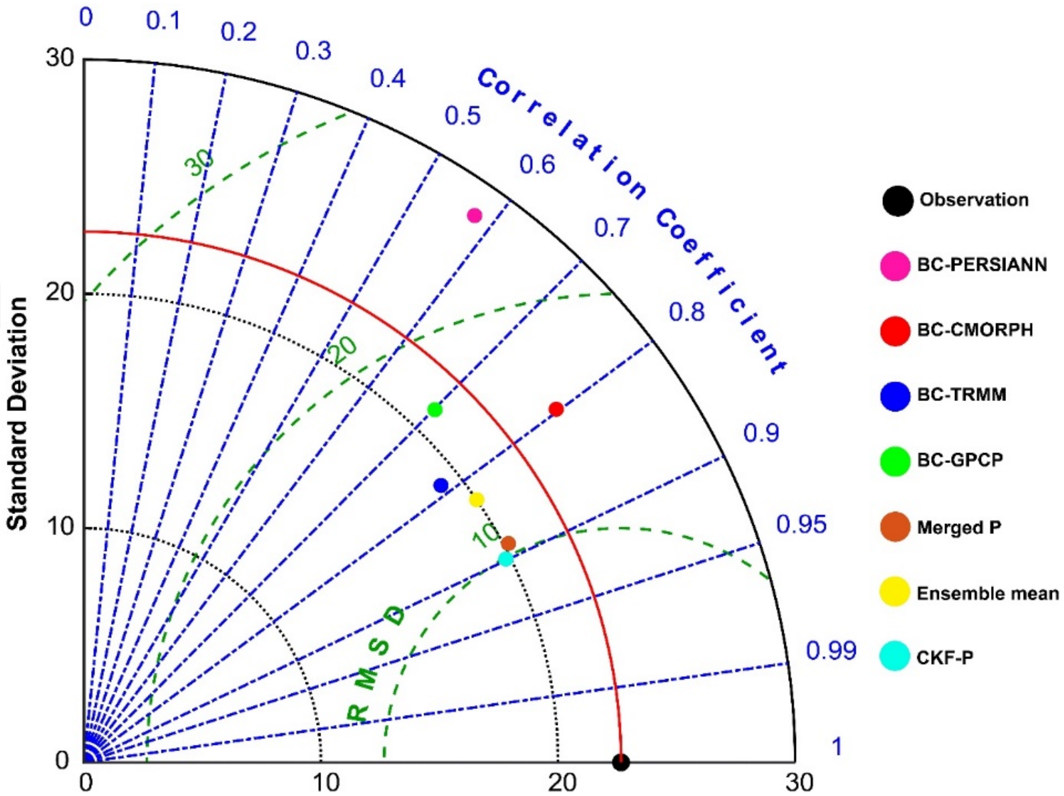

Figure 4.9 : The comparison of monthly CKF-P, the ensemble mean, merged P, and the four BC-P products with gauge observations using the Taylor diagram.

4.2 Second Approach

4.2.1 Fuzzy correction coefficients

The fuzzy correction coefficients obtained from three FLR models with fourteen different sub-models are given in Tables 4.2-4.3 for the two basins.

For the Sakarya basin, the α_P obtained from the Tanaka and Zeng models is sensitive to changes in the h value and type of cases (Table 4.2). It is seen that α_P slightly decreases with increasing h in both Case-I and Case-II in the Tanaka model. Overall, it is almost equal to one for all FLR sub-models. This indicates that mean of the five RS-based

P products accurately estimates P in the Sakarya basin. All the FLR sub-models calculated α_Q as 0.90. 0.90 value depicted that gauge estimations overestimated Q in the Sakarya basin. The α_{ET} and $\alpha_{\Delta S}$ values were calculated as 0.848 and 0.486 in all FLR sub-models, respectively. It can be inferred that RS-based ET (mean of the three ET products) and ΔS products overestimated ET and ΔS, respectively, in the Sakarya basin. Compared to the α values, c values are more sensitive to different cases and h values. In terms of spreads, c_P has the highest magnitude for most FLR sub-models, which means P is the most uncertain component among others in the Sakarya basin. The least uncertain component varies depending on the model type.

For the Cyprus basin, α_P was calculated above one in all Tanaka sub-models, while it was below one in Hojati (except Case-I (h =0.5) and Case-II (h =0.5) sub-models) and Zeng sub-models (Table 4.3). It was observed that α_P decreased with increasing h in the Tanaka and Hojati models. Moreover, α_P of the Hojati model approaches the α_P calculated in the Zeng model (α_P=0.958) when h increases. For α_Q, two values, 0.750 and 1.250, were obtained in the FLR sub-models. α_{ET} was calculated as 0.807 in all FLR sub-models. It indicates that mean of the three RS-based ET products overestimates ET in the Cyprus basin. The $\alpha_{\Delta S}$ ranges between 0.604-1.403, and it is the most sensitive parameter in the Cyprus basin, in terms of centers. Additionally, the spread of the correction coefficients indicates that ET is the least uncertain component for the Cyprus basin.

4.2.2 FLR outputs

Tables 4.4-4.6 compare the $\hat{r}$ values generated from three FLR models with fourteen different sub-models (for different $h$values) in the Sakarya basin. Compared to the non-fuzzy model, FLR sub-models provide more accurate results, in terms of MAE and RMSE. Moreover, the $\hat{r}$ values obtained from FLR sub-models are in good agreement with each other. Although the Zeng and Hojati sub-models have a slightly smaller MAE (27.57 mm) than Tanaka sub-models, Tanaka Case-I (h =0.7) sub-model slightly outperformed other models, in terms of RMSE (37.63 mm). Since RMSE is highly sensitive to the outlier values, MAE is better suited for comparison in this study [108]. Therefore, the Zeng and Hojati sub-models were selected as the best model for the

Table 4.2 : Fuzzy correction coefficients obtained from three FLR models with fourteen different sub-models in the Sakarya basin.

Model		h	P		Q		ET		ΔS	
			α_P	c_P	α_Q	c_Q	α_{ET}	c_{ET}	$\alpha_{\Delta S}$	$c_{\Delta S}$
Tanaka	Case-I	0.5	1.034	0.537	0.9	0.1	0.848	0.205	0.486	0.675
		0.7	1.022	0.758	0.9	0.1	0.848	0.205	0.486	0.675
		0.9	1.009	1.866	0.9	0.1	0.848	0.205	0.486	0.675
	Case-II	0.5	1.044	0.672	0.9	0.1	0.848	0.205	0.486	0.675
		0.7	1.028	0.894	0.9	0.1	0.848	0.205	0.486	0.675
		0.9	1.011	2.002	0.9	0.1	0.848	0.205	0.486	0.675
Hojati	Case-I	0.5	1.057	1.504	0.9	1.401	0.848	1.188	0.486	0.675
		0.7	1.057	1.363	0.9	1.662	0.848	0.988	0.486	0.675
		0.9	1.057	5.425	0.9	1.479	0.848	4.859	0.486	2.927
	Case-II	0.5	1.057	1.318	0.9	1.26	0.848	0.876	0.486	0.675
		0.7	1.057	1.095	0.9	1.496	0.848	0.594	0.486	0.675
		0.9	1.057	4.17	0.9	0.666	0.848	3.642	0.486	2.448
Zeng	Case-I		1.057	0.731	0.9	0.706	0.848	0.498	0.486	0.675
	Case-II		1.057	0.971	0.9	0.875	0.848	0.594	0.486	0.675

Table 4.3 : Fuzzy correction coefficients obtained from three FLR models with fourteen different sub-models in the Cyprus basin.

Model		h	P		Q		ET		ΔS	
			α_P	c_P	α_Q	c_Q	α_{ET}	c_{ET}	$\alpha_{\Delta S}$	$c_{\Delta S}$
Tanaka	Case-I	0.5	1.168	0.952	0.75	0.25	0.807	0.227	1.443	2.316
		0.7	1.128	1.529	0.75	0.25	0.807	0.227	0.955	2.316
		0.9	1.1	2.885	1.25	0.25	0.807	0.227	0.793	3.71
	Case-II	0.5	1.186	1.126	0.75	0.25	0.807	0.227	1.398	2.316
		0.7	1.121	1.413	0.75	0.25	0.807	0.227	0.973	2.316
		0.9	1.105	3.075	1.25	0.25	0.807	0.227	0.8	3.867
Hojati	Case-I	0.5	1.098	2.195	1.25	2.499	0.807	1.614	1.158	2.316
		0.7	0.98	3.266	0.75	2.499	0.807	2.689	0.695	2.316
		0.9	0.958	4.464	0.75	1.709	0.807	3.945	0.604	2.316
	Case-II	0.5	1.099	2.161	1.25	2.512	0.807	1.433	1.144	2.316
		0.7	0.985	3.15	0.75	2.545	0.807	2.421	0.713	2.316
		0.9	0.958	4.424	0.75	1.66	0.807	3.758	0.604	2.316
Zeng	Case-I		0.958	1.122	0.75	4.976	0.807	0.408	0.604	2.316
	Case-II		0.958	1.122	0.75	4.976	0.807	0.408	0.604	2.316

Sakarya basin. Given that model evaluation is possible only with gauge observations, we compared best Fuzzy P (the Zeng and Hojati sub-models) data with gauge P data to show the reliability of the estimated sub-model. Firstly, the Thiessen polygon method was applied to annual P measurements of the homogeneously distributed 23 gauge stations to derive the gauge-based areal mean P in the Sakarya basin. Then, a scatter plot was used to determine the relationship between Fuzzy P and gauge P (Figure 4.10(left column)). It should be noted that RS P is available for the years 2017 and

2018, so these years were also included in the evaluation. It is seen that Fuzzy P is in good agreement with gauge P, in terms of CC=0.921, KGE=0.881, and RMSE=29.52 mm.

Table 4.4 : Comparison of the $\hat{r}$ values obtained from three FLR models with fourteen different sub-models in the Sakarya basin (h=0.5).

Year	r before FLR model (mm)	$\hat{r}$ Tanaka Case-I	Tanaka Case-II	Hojati Case-I	Hojati Case-II	Zeng Case-I	Zeng Case-II
2003	-100.49	-9.7	-5.9	-1.02	-1.02	-1.02	-1.02
2004	-79.7	-37.45	-34.03	-29.63	-29.63	-29.63	-29.63
2005	-140.63	-30.44	-26.29	-20.95	-20.95	-20.96	-20.96
2006	-31.91	15.05	18.92	23.9	23.9	23.9	23.9
2007	-42.34	52.75	56.97	62.39	62.39	62.38	62.38
2008	-77.04	-15.88	-12.52	-8.19	-8.19	-8.2	-8.2
2009	-152.04	-10.76	-6.05	0	0	0	0
2010	29.57	107.06	112.45	119.39	119.39	119.39	119.39
2011	-150.2	-54.38	-50.37	-45.21	-45.21	-45.21	-45.21
2012	-130.38	-21.04	-16.81	-11.36	-11.36	-11.37	-11.37
2013	-10.6	7.73	11.28	15.84	15.84	15.84	15.84
2014	-162.388	-3.14	1.68	7.88	7.88	7.88	7.88
2015	-27.73	29.32	34.5	41.17	41.17	41.16	41.16
2016	-114.03	-20.08	-15.85	-10.42	-10.42	-10.42	-10.42
2019	-39.93	24.77	29.3	35.13	35.13	35.13	35.13
2020	-60.58	-17.15	-13.4	-8.59	-8.59	-8.59	-8.59
Total absolute error (mm)	1346.96	456.69	446.32	441.08	441.08	441.08	441.08
MAE (mm)	84.19	28.54	27.9	27.57	27.57	27.57	27.57
RMSE (mm)	97.85	37.83	38.53	40.08	40.08	40.08	40.08

160 80 0
Absolute error (mm)

For the Cyprus basin, the model outputs are shown in Tables 4.7-4.9. The MAE and RMSE of the non-fuzzy model are 96.78 mm and 109.23 mm, respectively. There are significant differences in the values of performance metrics among the various FLR sub-models, mainly due to the high uncertainty of RS products over the Cyprus basin. The MAE values range from 83.25 mm to 50.46 mm. The RMSE values range from 118.93 mm to 63.87 mm. Tanaka models have the worst performance, particularly for small h values. Zeng Case-I, Zeng Case-II, and Hojati (h =0.9) sub-models showed the best performance, given an MAE of 50.46 mm, and RMSE of 63.87mm. The CC, KGE, and RMSE of Fuzzy P were calculated as 0.885, 0.810, and 50.17 mm, respectively (Figure 4.10(right column)). This suggests that the Fuzzy P well captured the temporal pattern of gauge P in general.

Table 4.5 : Comparison of the $\hat{r}$ values obtained from three FLR models with fourteen different sub-models in the Sakarya basin (h=0.7).

Year	r before FLR model (mm)	$\hat{r}$					
		Tanaka		Hojati		Zeng	
		Case-I	Case-II	Case-I	Case-II	Case-I	Case-II
2003	-100.49	-14.47	-12.19	-1.02	-1.02	-1.02	-1.02
2004	-79.7	-41.75	-39.7	-29.63	-29.63	-29.63	-29.63
2005	-140.63	-35.66	-33.17	-20.95	-20.95	-20.96	-20.96
2006	-31.91	10.17	12.5	23.9	23.9	23.9	23.9
2007	-42.34	47.45	49.98	62.39	62.39	62.38	62.38
2008	-77.04	-20.11	-18.09	-8.19	-8.19	-8.2	-8.2
2009	-152.04	-16.69	-13.86	0	0	0	0
2010	29.57	100.27	103.51	119.39	119.39	119.39	119.39
2011	-150.2	-59.43	-57.02	-45.21	-45.21	-45.21	-45.21
2012	-130.38	-26.36	-23.82	-11.36	-11.36	-11.37	-11.37
2013	-10.6	3.26	5.39	15.84	15.84	15.84	15.84
2014	-162.388	-9.21	-6.31	7.88	7.88	7.88	7.88
2015	-27.73	22.8	25.91	41.17	41.17	41.16	41.16
2016	-114.03	-25.39	-22.86	-10.42	-10.42	-10.42	-10.42
2019	-39.93	19.06	21.78	35.13	35.13	35.13	35.13
2020	-60.58	-21.85	-19.61	-8.59	-8.59	-8.59	-8.59
Total absolute error (mm)	1346.96	473.95	465.72	441.08	441.08	441.08	441.08
MAE (mm)	84.19	29.62	29.11	27.57	27.57	27.57	27.57
RMSE (mm)	97.85	37.62	37.63	40.08	40.08	40.08	40.08

160 80 0

Absolute error (mm)

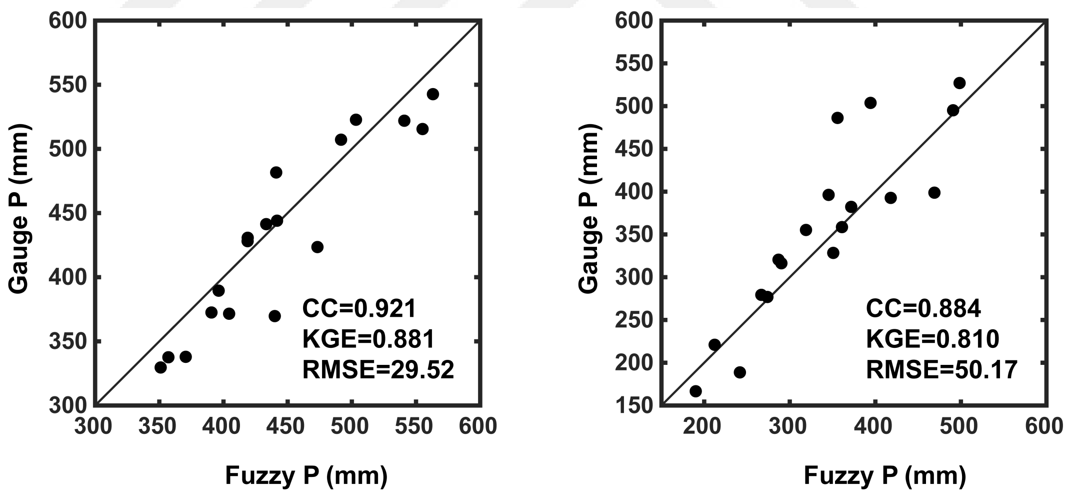

Figure 4.10 : Comparison of the best FLR model P against gauge P: (a) Sakarya basin, (b) Cyprus basin.

4.2.3 Sensitivity analysis

In the second approach, three h-cut values (0.5, 0.7, and 0.9) were considered for Tanaka and Hojati FLR models to understand the sensitivity of the results to different h values. In terms of α coefficients (Tables 4.2-4.3), the Tanaka model is more sensitive

Table 4.6 : Comparison of the $\hat{r}$ values obtained from three FLR models with fourteen different sub-models in the Sakarya basin (h=0.9).

Year	r before FLR model (mm)	$\hat{r}$					
		Tanaka		Hojati		Zeng	
		Case-I	Case-II	Case-I	Case-II	Case-I	Case-II
2003	-100.49	-19.24	-18.48	-1.02	-1.02	-1.02	-1.02
2004	-79.7	-46.05	-45.37	-29.63	-29.63	-29.63	-29.63
2005	-140.63	-40.88	-40.05	-20.95	-20.95	-20.96	-20.96
2006	-31.91	5.3	6.08	23.9	23.9	23.9	23.9
2007	-42.34	42.15	42.99	62.39	62.39	62.38	62.38
2008	-77.04	-24.34	-23.67	-8.19	-8.19	-8.2	-8.2
2009	-152.04	-22.61	-21.67	0	0	0	0
2010	29.57	93.49	94.57	119.39	119.39	119.39	119.39
2011	-150.2	-64.47	-63.67	-45.21	-45.21	-45.21	-45.21
2012	-130.38	-31.68	-30.84	-11.36	-11.36	-11.37	-11.37
2013	-10.6	-1.2	-0.49	15.84	15.84	15.84	15.84
2014	-162.388	-15.27	-14.3	7.88	7.88	7.88	7.88
2015	-27.73	16.29	17.33	41.17	41.17	41.16	41.16
2016	-114.03	-30.7	-29.86	-10.42	-10.42	-10.42	-10.42
2019	-39.93	13.36	14.27	35.13	35.13	35.13	35.13
2020	-60.58	-26.56	-25.81	-8.59	-8.59	-8.59	-8.59
Total absolute error (mm)	1346.96	493.6	489.44	441.08	441.08	441.08	441.08
MAE (mm)	84.19	30.85	30.59	27.57	27.57	27.57	27.57
RMSE (mm)	97.85	38.16	38.02	40.08	40.08	40.08	40.08

160 80 0
Absolute error (mm)

to different h values than the Hojati model in both basins. The result is consistent with study conducted by [25], which compared Tanaka and Hojati models over Azghand catchment, Iran. P and ΔS are the most sensitive parameters to different h values in both basins among the four WB components. This is mainly caused by the higher uncertainties of these two components (Tables 3.3-3.4). The higher the amount of uncertainty, the higher the degree of sensitivity. For the Cyprus basin, the fuzzy correction coefficients are highly sensitive to different h values and cases in Tanaka and Hojati models. Therefore, the FLR outputs in the Cyprus basin are more unstable than those in the Sakarya basin (Tables 4.4-4.9). This result is not surprising as the Cyprus basin is too small for some RS-based products, especially GRACE ΔS, to resolve. Several studies have shown that GRACE errors are inversely proportional to the size of the basin [16,51,54]. [16] found that ΔS errors can reach up to 130% in basins with areas of less than 100,000 km^2. In this study, the maximum ΔS error in the Cyprus basin was calculated as 214.97%.

Table 4.7 : Comparison of the $\hat{r}$ values obtained from three FLR models with fourteen different sub-models in the Cyprus basin (h=0.5).

Year	r before FLR model (mm)	$\hat{r}$ Tanaka Case-I	$\hat{r}$ Tanaka Case-II	$\hat{r}$ Hojati Case-I	$\hat{r}$ Hojati Case-II	$\hat{r}$ Zeng Case-I	$\hat{r}$ Zeng Case-II
2003	-136.6	9.85	17.61	-19.45	-18.57	-48.27	-48.27
2004	36.86	223.23	227.67	157.27	156.9	80.21	80.21
2005	-137.6	-7.06	-2.24	-32.79	-32.45	-69.44	-69.44
2006	-171.3	-52.92	-46.44	-73.16	-72.33	-88.15	-88.15
2007	-75.2	72.56	79.71	28.61	29.26	-0.01	-0.01
2008	-109.48	6	8.02	-20.49	-20.71	-65.3	-65.3
2009	-109.69	0.88	13.57	-5.66	-3.49	0	0
2010	-103.28	61.57	66.08	0	0	-36.73	-36.73
2011	-24.33	158.26	161.47	106.28	105.75	20.34	20.34
2012	-52.42	87.07	100.25	70.65	72.65	53.54	53.54
2013	-164.6	-27.48	-25.25	-54.95	-55.2	-107.44	-107.44
2014	-31.47	128.31	130.71	84.22	83.67	6.6	6.6
2015	-181.09	-68.71	-58.26	-71.59	-69.83	-73.19	-73.19
2016	-30.89	111.32	114.81	72.35	72.16	12.08	12.08
2019	81.25	292.4	299.16	227.76	227.67	133.28	133.28
2020	-102.41	24.41	33.76	7.35	8.67	-12.85	-12.85
Total absolute error (mm)	1548.48	1332.02	1384.99	1032.58	1029.31	807.42	807.42
MAE (mm)	96.78	83.25	86.56	64.54	64.33	50.46	50.46
RMSE (mm)	109.23	115.9	118.93	87.14	86.98	63.87	63.87

300 150 0

Absolute error (mm)

Table 4.8 : Comparison of the $\hat{r}$ values obtained from three FLR models with fourteen different sub-models in the Cyprus basin (h=0.7).

Year	r before FLR model (mm)	$\hat{r}$ Tanaka Case-I	$\hat{r}$ Tanaka Case-II	$\hat{r}$ Hojati Case-I	$\hat{r}$ Hojati Case-II	$\hat{r}$ Zeng Case-I	$\hat{r}$ Zeng Case-II
2003	-136.6	6.55	3.45	-42.06	-40.84	-48.27	-48.27
2004	36.86	173.9	172.12	95.6	98.63	80.21	80.21
2005	-137.6	-20.46	-22.39	-62.75	-61.43	-69.44	-69.44
2006	-171.3	-49.94	-52.53	-84.4	-83.66	-88.15	-88.15
2007	-75.2	61.31	58.45	7.77	9.3	-0.01	-0.01
2008	-109.48	-19.15	-19.96	-57.62	-56.11	-65.3	-65.3
2009	-109.69	36.17	31.1	0	0	0	0
2010	-103.28	31.76	29.96	-26.16	-24.08	-36.73	-36.73
2011	-24.33	107.69	106.4	35.19	38.11	20.34	20.34
2012	-52.42	109.63	104.36	57.05	57.75	53.54	53.54
2013	-164.6	-55.77	-56.66	-98.83	-97.14	-107.44	-107.44
2014	-31.47	82.44	81.48	19.71	22.29	6.6	6.6
2015	-181.09	-41.26	-45.44	-72.78	-72.71	-73.19	-73.19
2016	-30.89	78.22	76.83	22.76	24.87	12.08	12.08
2019	81.25	242.63	239.92	150.39	153.76	133.28	133.28
2020	-102.41	34.6	30.86	-8.9	-8.13	-12.85	-12.85
Total absolute error (mm)	1548.48	1151.48	1131.91	841.99	848.8	807.42	807.42
MAE (mm)	96.78	71.97	70.74	52.62	53.05	50.46	50.46
RMSE (mm)	109.23	93.89	92.57	65.76	66.29	63.87	63.87

250 125 0

Absolute error (mm)

Table 4.9 : Comparison of the $\hat{r}$ values obtained from three FLR models with fourteen different sub-models in the Cyprus basin (h=0.9).

Year	r before FLR model (mm)	$\hat{r}$					
		Tanaka		Hojati		Zeng	
		Case-I	Case-II	Case-I	Case-II	Case-I	Case-II
2003	-136.6	-9.92	-8.14	-48.27	-48.27	-48.27	-48.27
2004	36.86	133.59	136.2	80.21	80.21	80.21	80.21
2005	-137.6	-33.84	-32.36	-69.44	-69.44	-69.44	-69.44
2006	-171.3	-61.7	-60.4	-88.15	-88.15	-88.15	-88.15
2007	-75.2	32.35	34.27	-0.01	-0.01	-0.01	-0.01
2008	-109.48	-32.93	-31.65	-65.3	-65.3	-65.3	-65.3
2009	-109.69	34.88	36.43	0	0	0	0
2010	-103.28	-11.58	-9.61	-36.73	-36.73	-36.73	-36.73
2011	-24.33	80.03	82.42	20.34	20.34	20.34	20.34
2012	-52.42	104.11	106.19	53.54	53.54	53.54	53.54
2013	-164.6	-69	-67.57	-107.44	-107.44	-107.44	-107.44
2014	-31.47	59.62	61.67	6.6	6.6	6.6	6.6
2015	-181.09	-39.19	-37.86	-73.19	-73.19	-73.19	-73.19
2016	-30.89	57.21	59.07	12.08	12.08	12.08	12.08
2019	81.25	207.27	210.39	133.28	133.28	133.28	133.28
2020	-102.41	27.53	29.2	-12.85	-12.85	-12.85	-12.85
Total absolute error (mm)	1548.48	994.75	1003.43	807.42	807.42	807.42	807.42
MAE (mm)	96.78	62.17	62.71	50.46	50.46	50.46	50.46
RMSE (mm)	109.23	79.24	80.38	63.87	63.87	63.87	63.87
	210			105			0
				Absolute error (mm)			

4.2.4 The comparison of Fuzzy P with five RS-based products

In both basins, further work has been made to evaluate the precision and accuracy of the FLR method by comparing Fuzzy P with five RS-based P products. Figure 4.11 shows the time series of six P products, namely GSMaP, IMERG, CMORPH, PERSIANN, CHIRPS, and Fuzzy P in the Sakarya and Cyprus basins. The temporal variations of the P products are similar to that of the gauge observations in the two basins. However, there are significant differences in the magnitudes of annual P among the six P products. The values of the performance metrics for all the P products are shown in Table 4.10. PERSIANN performed the worst among the six products in both basins. Its average PBIAS and RMSE are -44.18% and 189.35 mm, respectively, indicating significant underestimation of the P in both basins. GSMaP scores the highest correlation (0.960) in the Sakarya basin, and IMERG scores the highest correlation (0.956) in the Cyprus basin. In both basins, Fuzzy P has the lowest RMSE (29.52 mm and 50.17 mm), the largest KGE (0.881 and 0.810), and the lowest

PBIAS (2.88% and -4.03%) value among the six P products. The results strongly indicated that Fuzzy P has the best consistency with gauge observations in both basins.

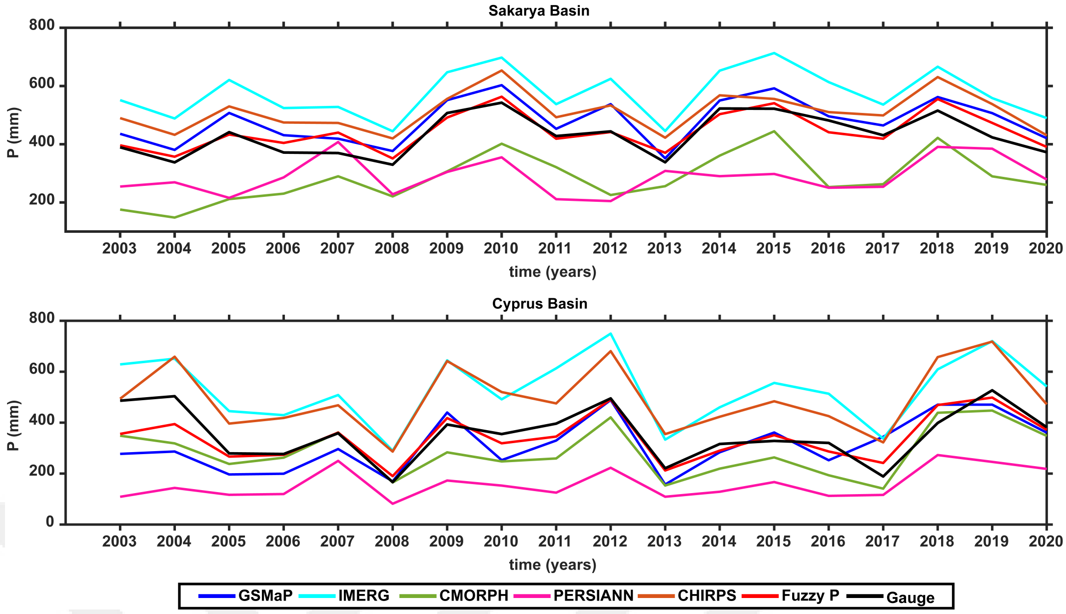

Figure 4.11 : The annual time series of the six P products in the Sakarya and Cyprus basins.

Table 4.10 : The performance metrics of the six P products in the Sakarya and Cyprus basins.

Product	Sakarya basin				Cyprus basin			
	CC	RMSE (mm)	KGE	PBIAS (%)	CC	RMSE (mm)	KGE	PBIAS (%)
GSMaP	0.96	52.75	0.869	11.21	0.635	96.75	0.616	-11.8
IMERG	0.954	145.14	0.708	33.11	0.956	178.92	0.452	48.97
CMORPH	0.762	158.27	0.403	-34.61	0.839	90.86	0.723	-20.07
PERSIANN	0.201	164.86	0.049	-33.17	0.558	213.83	0.161	-55.19
CHIRPS	0.92	84.52	0.815	18.55	0.889	150.62	0.541	39.18
Fuzzy P	0.921	29.52	0.881	2.88	0.885	50.17	0.81	-4.03

4.3 Comparison of the Results from the First and Second Approaches for the Sakarya Basin

The time series of the fuzzy and CKF derived WB outputs at the annual scale from 2005 to 2011 over the Sakarya basin are presented in Figure 4.12 (Since CKF eliminates the r, CKF-derived data is accepted as a reference in calculations). The P, ET, and Q values of the both approaches showed similar seasonal variation with peak and bottom values appeared in nearly the same years. In terms of CC, RMSE, and bias, fuzzy outputs show closest agreement with CKF outputs for Q (CC=0.996, RMSE=8.18 mm/year, bias=-7.70 mm/year) , with slightly less agreement for P (CC=0.984, RMSE=32.23 mm/year, bias=26.69 mm/year) and ET (CC=0.974, RMSE=13.80 mm/year, bias=-12.52 mm/year), and much less agreement for ΔS (CC=0.300, RMSE=62.82 mm/year, bias=28.14 mm/year). In terms of PBIAS, ET (PBIAS=-3.33%) outperforms other WB components followed by P (PBIAS=6.29%), Q (PBIAS=-10.3%) and ΔS (PBIAS=-109.98%). It is worth noting that although the bias between the fuzzy and the CKF-derived ΔS is close to that for P (26.69 mm/year for P and 28.14 mm/year for ΔS), we computed high PBIAS for ΔS as a result of a low mean ΔS. According to these performance measures, it can be concluded that the majority of the errors in the second approach are caused by fuzzy ΔS.

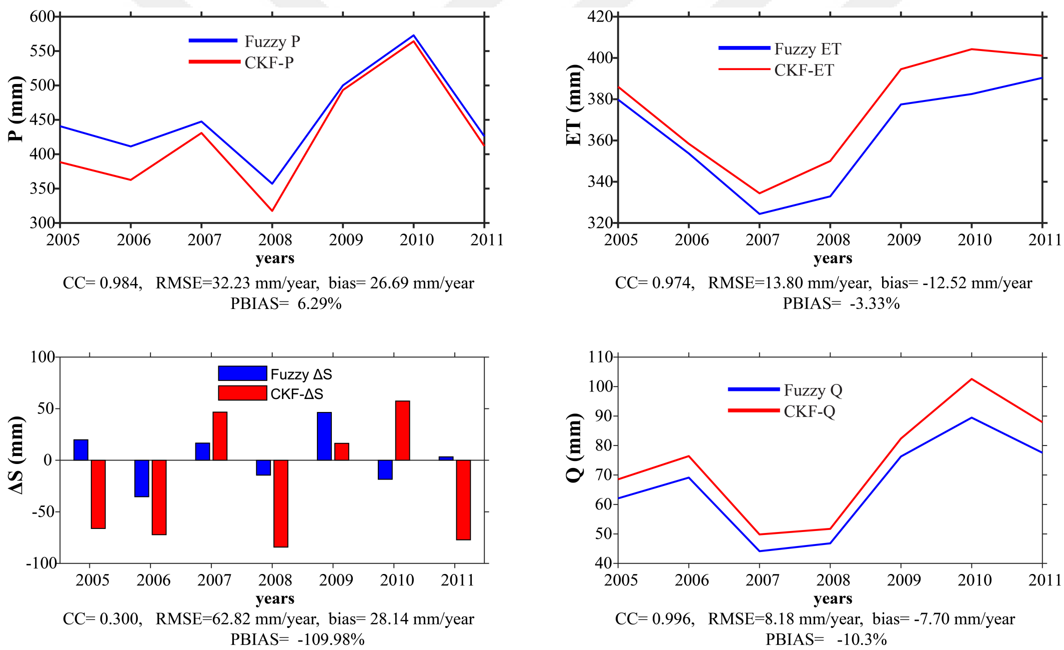

Figure 4.12 : The time series of the fuzzy and CKF derived WB outputs at the annual scale from 2005 to 2011 over the Sakarya basin.

5. DISCUSSIONS AND RECOMMENDATIONS

This study aims to improve WB estimations in two smaller scale basins using two different approaches. The first approach enforces the WB components to close the WB equation. In other words, the r was distributed among the WB components in accordance with their error variances, and the r was zeroed. On the other hand, there is no such necessity in the second approach. The main goal of the second approach is to reduce the magnitude of residual errors on an annual scale by applying fuzzy correction coefficients to each WB component.

5.1 Comprehensive Evaluation of the Hydrological Data Products

It should be noted that the estimated coefficients are basin-specific as the performance of products is highly affected by basin characteristics (e.g., slope, elevation, land cover). For instance, [109] stated that, probably as a result of orographic cloud dynamics, TRMM tends to underestimate P in mountainous regions. In contrast, TRMM greatly overestimated gauge P in the Sakarya basin, especially in rainy seasons. It has the highest bias (25.83 mm/month) and RMSE (39.22 mm/month) compared to other RS-based products (Figure 4.2). This is mainly because the TRMM version (TRMM-3B42RT V7) used in this study was not gauge-corrected. It includes purely RS observations. Despite having the greatest RMSE and bias levels, TRMM improved the most after bias correction. This is because TRMM has the best CC (0.69) with gauge observations. The CC is concerned with linear connections between variables and, the bias correction method used in this study is also linear. Although TRMM's general tendency was to overestimate gauge P in rainy seasons, it underestimated P in summer. The relatively high positive bias in TRMM estimations during the rainy seasons is compatible with other reports [110,111]. The underestimation of TRMM during the summer season can be attributed to the rainfall intensity during the summer months. The rainfall duration is shorter, and the rainfall intensity is higher in the Sakarya basin during the summer. [112] pointed out that TRMM can overestimate total *P* for mild and moderate rainfall intensities and underestimate for high rainfall intensities.

For both approaches, PERSIANN has the poorest performance among RS products. The weak performance of PERSIANN might be due to the fact that it primarily uses infrared (IR) data rather than passive microwave (PMW) data. In general, PMW has a stronger ability in detecting *P* than IR data [67,113]. IR technique tries to estimate *P* using the temperature and brightness of the cloud top, however complex mechanisms exist to transform cloud information into *P*, particularly in places with dense cloudiness and heavy rainfall [114]. The newer generation *P* product, GSMaP, outperformed other RS-based *P* products in terms of CC, RMSE, KGE, and PBIAS, especially in the Sakarya basin (Table 4.10). This could be due to its ability to combine *P* estimates from multiple satellites, as well as gauge analyses [115,116]. Additionally, the high spatial resolution of GSMaP may have made it possible to more efficiently capture the temporal variations of *P*. The performance of GSMaP in the Cyprus basin is poorer than in the Sakarya basin. The Sakarya basin has a more complex and mountainous surface compared to the Cyprus basin. [117] stated that the performance of GSMaP is comparatively better at higher altitudes due to the inclusion of the terrain correction algorithm. Similar to TRMM, newer generation *P* product, IMERG, greatly overestimated *P* in both basins. However, it has a very strong linear correlation with gauge observations, indicating that the IMERG estimations can be better enhanced by using the linear scaling bias correction method.

For ET, TERRACLIMATE reanalysis product showed the worst performance (Table 4.1) among all ET products which is likely due to the inability of TERRACLIMATE to represent actual surface vegetation [118]. The accuracy of TERRACLIMATE ET has not been rigorously verified in global basins. [119] reported that the performance of TERRACLIMATE ET was inferior to that of other TERRACLIMATE products. Although both LSM products (VIC and NOAH) and RS products (MODIS, GLEAM, and NTSG) perform reasonably well in the Sakarya basin, LSM products has generally lower uncertainty than RS products. The lower uncertainty in LSM ET is most likely because LSM ET is constrained by meteorological forcing inputs and soil water budget balance. On the contrary, without taking into account the soil water budget balance, the key parameter influencing ET in RS is net radiation. Similar to the GTCH method, the triple collocation (TC) method is also used to determine the relative uncertainty of three products when there is no actual observations [120]–[122]. The GTCH approach allows for simultaneous evaluation of all products, whereas the TC method only allows for comparison of up to three products. Several studies showed that the TC method is superior to GTCH method when products include multiplicative bias [123]–[125]. TC method can also be applied to ET products. However, the error variances of the products must be uncorrelated in the TC method. As the RS products generally use similar algorithms, the error variances of these products are likely correlated. Therefore, users should employ TC method with caution. Using products with different types of algorithms (one RS, one LSM, one reanalysis) will produce more reliable results.

It is found that CKF estimates are insensitive to the different levels of Q uncertainty in the Sakarya basin (Figures 4.7-4.8). In CKF, the redistribution of the WB r among WB components is proportional to component magnitude. The Q in Sakarya basin is quite low compared to other WB components (Figure 5.1). Therefore, in basins with high Q potential, changes in Q uncertainty may impact CKF outcomes.

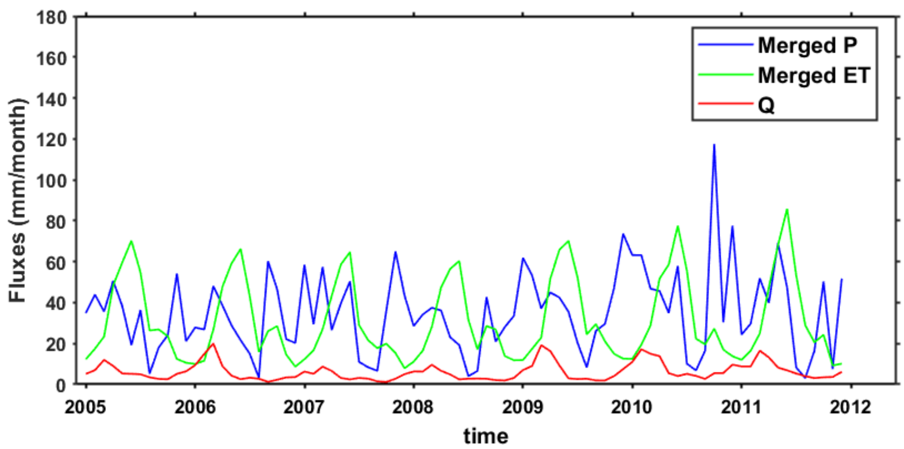

Figure 5.1 : Comparison of the fluxes of WB components.

The results point out that ΔS is the most uncertain component in the WB equation. However, this outcome contradicts the other WB studies, which indicate P as the most uncertain component [11,12,20]. This is mainly because the previous WB studies were conducted in large basins where GRACE products can sufficiently capture the basin geometry. The Sakarya basin, however, is a relatively small basin that GRACE cannot simply resolve. In light of this information, large errors in ΔS estimations in smaller basins like Sakarya are unavoidable, as previously reported by [16,53,54]. The planned high-resolution satellite gravity missions, such as Next Generation Gravity Mission, may provide improved ΔS estimates in smaller scale basins for future studies.

5.2 Potential causes of large errors in the FLR outputs

Overall, Tanaka sub-models performed the worst among the FLR models. This is mainly because the Tanaka model forces the h-cut estimated intervals to capture the h-cut observed intervals (Figure 3.5(a)). Due to this forcing, the Tanaka model is susceptible to outliers in data. The best fuzzy sub-models reduced the error up to 68% and 52% in terms of mean absolute error compared to non-fuzzy model in the Sakarya and Cyprus basins, respectively.

For the Sakarya basin, the highest annual $\hat{r}$ was observed in 2010 (ranging from 93.49 mm to 119.39 mm in all sub-models). While gauge P was 542.65 mm in 2010, Fuzzy P was 563.21 mm (Figure 4.11). This indicates that Fuzzy P has a low contribution to $\hat{r}$. For the Cyprus basin, the highest annual $\hat{r}$ was observed in 2019 (compared to the non-fuzzy model). Gauge P was 527.00 mm in 2019. On the other hand, the Fuzzy P was 498.46 mm in 2019. This implies that the contribution of Fuzzy P to $\hat{r}$ was low in 2019.

Interestingly, high r was observed in the years when peak P occurred in both basins. [25] also found that the largest $\hat{r}$ occurred in the wettest year. This might be because the impact of P on ΔS appeared later, as ΔS includes groundwater storage. [3,49] also stated that there are 2 months lag between P and ΔS.

6. CONCLUSIONS

WB estimations are essential for determining the amount of water flowing into and out of a basin. Recently, RS has provided unprecedented estimations with high spatiotemporal resolution and broad spatial coverage. However, significant uncertainties are inevitable in RS products due to sampling infrequency, retrieval algorithm imperfections, orbit shifting, complex topography, and cloud top reflectance. This study evaluated the potential of the two approaches to minimize r in the WB equation. In the first approach, we assessed the uncertainty of various P and ET products using rainfall gauge observations and the GTCH method. Following that, the P and ET products were merged independently based on their error variances. Finally, we employed the CKF method to obtain reliable water budget estimations, zeroing the residual error. The first approach was performed at the Sakarya basin. In the second approach, two main steps were followed. First, the uncertainty of RS products was quantified using a percentage error approach. Second, fuzzy correction coefficients obtained from three FLR models were assigned to each WB component to minimize r.

The main conclusions of this study can be summarized as follows.

First approach:

1. The performance of RS-based P products, except PERSIANN, was significantly improved after bias removal. Bias removal reduced the RMSE of TRMM up to 64% (39.22 mm/month to 14.05 mm/month). The RMSE of PERSIANN was calculated as 23.67 mm/month and 24.15 mm/month, respectively, before and after bias correction.

2. In terms of mean monthly merging weights, CMORPH performed the best among the four RS-based P products. Since the performance of PERSIANN did not improve after bias adjustment, it received the lowest weight.

3. The uncertainties from the GTCH method show that VIC ET has the lowest uncertainty (2.76mm/month) compared to other ET products. On the other hand, TERRACLIMATE ET has the highest uncertainty (9.28 mm/month), which may be caused by the inability of TERRACLIMATE to represent actual surface vegetation.

4. The results show that CKF estimates are insensitive to the different levels of Q uncertainty values. Compared to other WB components, ΔS has the highest non-closure error attribution. This is mainly caused by the fact that GRACE estimations are likely to have high inaccuracies in small basins due to coarse spatial resolution.

5. For the validation of CKF-P, the Taylor diagram was analyzed. It was found that CKF-P is closer to the gauge observations than other products, indicating that CKF-P is the most reliable product among the seven P products.

Second approach:

1. All sub-models impressively reduced the errors in the Sakarya basin, but the Zeng and Hojati sub-models performed better than the Tanaka sub-models. The annual MAE and RMSE were reduced from 84.19 mm and 97.85 mm from the non-fuzzy model to 27.57 mm and 39.82 mm with the Zeng Case-I sub-model.

2. Fuzzy correction coefficients calculated for each WB component in the Sakarya basin showed that mean of the five RS-based P products accurately estimated P. On the other hand, Q, ET, and ΔS are overestimated.

3. Tanaka and Hojati models are sensitive to different h values in the Cyprus basin. The error metrics of these models decrease with increasing h value. Zeng Case-I, Zeng Case-II, and Hojati (h =0.9) sub-models performed the best, in terms of MAE and RMSE.

4. Fuzzy correction coefficients calculated for the Cyprus basin vary significantly among the different sub-models. This is due to the fact that the Cyprus basin is too small for some low-resolution RS-based products to resolve.

5. Fuzzy P outperforms other P products in both basins, in terms of RMSE, KGE, and PBIAS.

The P, ET , and Q values of the both approaches are in agreement with each other. In terms of CC, RMSE, and bias, fuzzy outputs show closest agreement with CKF outputs for Q, with slightly less agreement for P and ET, and much less agreement for ΔS. Therefore, it can be said that ΔS has made the largest contribution to the errors in the fuzzy approach.

In summary, the outcomes of this study suggest that two approaches can be applied to hydrological RS products for obtaining improved estimations of WB components, especially in small and ungauged basins. It should be noted that the error covariances of the P products are assumed to be zero in this study. However, error covariances might exist as products often use similar techniques like the same radiative transfer model or retrieval algorithms. If such complex error knowledge is provided, this prior information can also be considered in the P merging process. The planned high-resolution satellite gravity missions, such as Next Generation Gravity Mission, may provide improved S estimates in small basins for future studies. In regions with data scarcity, P products can also be integrated with the GTCH method as an alternative solution to replace observed rainfall data.

REFERENCES

[1] **Water, U.** (2020). World Water Development Report: Water and Climate Change, *Houille Blanche*, *2020*.

[2] **Steduto, P.**, **Faurès, J.M.**, **Hoogeveen, J.**, **Winpenny, J. and Burke, J.** (2012). Coping with water scarcity: an action framework for agriculture and food security, *Rome: Food and Agriculture Organization of the United Nations*.

[3] **Kayan, G.**, **Erten, E.**, **Mercan, H. and Ozcan, O.** (2017). Understanding of Cyprus total water storage under climate change, *2017 IEEE international geoscience and remote sensing symposium (IGARSS)*, IEEE, pp.5591–5594.

[4] **Luo, Z.**, **Shao, Q.**, **Wan, W.**, **Li, H.**, **Chen, X.**, **Zhu, S. and Ding, X.** (2021). A new method for assessing satellite-based hydrological data products using water budget closure, *Journal of Hydrology*, *594*, 125927.

[5] **Atchley, A.L. and Maxwell, R.M.** (2011). Influences of subsurface heterogeneity and vegetation cover on soil moisture, surface temperature and evapotranspiration at hillslope scales, *Hydrogeology Journal*, *19*(2), 289–305.

[6] **Wang, H.**, **Guan, H.**, **Gutiérrez-Jurado, H.A. and Simmons, C.T.** (2014). Examination of water budget using satellite products over Australia, *Journal of Hydrology*, *511*, 546–554.

[7] **Wang, Q.**, **Xia, J.**, **She, D.**, **Zhang, X.**, **Liu, J. and Zhang, Y.** (2021). Assessment of four latest long-term satellite-based precipitation products in capturing the extreme precipitation and streamflow across a humid region of southern China, *Atmospheric Research*, *257*, 105554.

[8] **Wongchuig-Correa, S.**, **de Paiva, R.C.D.**, **Biancamaria, S. and Collischonn, W.** (2020). Assimilation of future SWOT-based river elevations, surface extent observations and discharge estimations into uncertain global hydrological models, *Journal of Hydrology*, *590*, 125473.

[9] **Allen, R.G.**, **Pereira, L.S.**, **Howell, T.A. and Jensen, M.E.** (2011). Evapotranspiration information reporting: I. Factors governing measurement accuracy, *Agricultural Water Management*, *98*(6), 899–920.

[10] **Lv, M.**, **Ma, Z.**, **Yuan, X.**, **Lv, M.**, **Li, M. and Zheng, Z.** (2017). Water budget closure based on GRACE measurements and reconstructed

evapotranspiration using GLDAS and water use data for two large densely-populated mid-latitude basins, *Journal of Hydrology*, *547*, 585–599.

[11] **Sheffield, J.**, **Ferguson, C.R.**, **Troy, T.J.**, **Wood, E.F. and McCabe, M.F.** (2009). Closing the terrestrial water budget from satellite remote sensing, *Geophysical Research Letters*, *36*(7).

[12] **Gao, H.**, **Tang, Q.**, **Ferguson, C.R.**, **Wood, E.F. and Lettenmaier, D.P.** (2010). Estimating the water budget of major US river basins via remote sensing, *International Journal of Remote Sensing*, *31*(14), 3955–3978.

[13] **Azarderakhsh, M.**, **Rossow, W.B.**, **Papa, F.**, **Norouzi, H. and Khanbilvardi, R.** (2011). Diagnosing water variations within the Amazon basin using satellite data, *Journal of Geophysical Research: Atmospheres*, *116*(D24).

[14] **Armanios, D.E. and Fisher, J.B.** (2014). Measuring water availability with limited ground data: assessing the feasibility of an entirely remote-sensing-based hydrologic budget of the Rufiji Basin, Tanzania, using TRMM, GRACE, MODIS, SRB, and AIRS, *Hydrological Processes*, *28*(3), 853–867.

[15] **Penatti, N.C.**, **de Almeida, T.I.R.**, **Ferreira, L.G.**, **Arantes, A.E. and Coe, M.T.** (2015). Satellite-based hydrological dynamics of the world's largest continuous wetland, *Remote Sensing of Environment*, *170*, 1–13.

[16] **Moreira, A.A.**, **Ruhoff, A.L.**, **Roberti, D.R.**, **de Arruda Souza, V.**, **da Rocha, H.R. and de Paiva, R.C.D.** (2019). *Journal of Hydrology*, *575*, 131–147.

[17] **Abolafia-Rosenzweig, R.**, **Pan, M.**, **Zeng, J. and Livneh, B.** (2021). Remotely sensed ensembles of the terrestrial water budget over major global river basins: An assessment of three closure techniques, *Remote Sensing of Environment*, *252*, 112191.

[18] **Aires, F.** (2014). Combining datasets of satellite-retrieved products. Part I: Methodology and water budget closure, *Journal of Hydrometeorology*, *15*(4), 1677–1691.

[19] **Pan, M.**, **Sahoo, A.K.**, **Troy, T.J.**, **Vinukollu, R.K.**, **Sheffield, J. and Wood, E.F.** (2012). Multisource estimation of long-term terrestrial water budget for major global river basins, *Journal of Climate*, *25*(9), 3191–3206.

[20] **Sahoo, A.K.**, **Pan, M.**, **Troy, T.J.**, **Vinukollu, R.K.**, **Sheffield, J. and Wood, E.F.** (2011). Reconciling the global terrestrial water budget using satellite remote sensing, *Remote Sensing of Environment*, *115*(8), 1850–1865.

[21] **Zhang, Y.**, **Pan, M.**, **Sheffield, J.**, **Siemann, A.L.**, **Fisher, C.K.**, **Liang, Miaoling, ... and Wood, E.F.** (2018). A Climate Data Record (CDR) for the global terrestrial water budget: 1984–2010, *Hydrology and Earth System Sciences*, *22*(1), 241–263.

[22] **Munier, S. and Aires, F.** (2018). A new global method of satellite dataset merging and quality characterization constrained by the terrestrial water budget, *Remote Sensing of Environment*, *205*, 119–130.

[23] **Zhang, Y.**, **Pan, M. and Wood, E.F.**, (2016). On creating global gridded terrestrial water budget estimates from satellite remote sensing, Remote sensing and water resources, Springer, pp.59–78.

[24] **Oliveira, P.T.S.**, **Nearing, M.A.**, **Moran, M.S.**, **Goodrich, D.C.**, **Wendland, E. and Gupta, H.V.** (2014). Trends in water balance components across the Brazilian Cerrado, *Water Resources Research*, *50*(9), 7100–7114.

[25] **Khazaei, B. and Hosseini, S.M.** (2015). Improving the performance of water balance equation using fuzzy logic approach, *Journal of Hydrology*, *524*, 538–548.

[26] **Silver, M.**, **Svoray, T.**, **Karnieli, A. and Fredj, E.** (2020). Improving weather radar precipitation maps: A fuzzy logic approach, *Atmospheric Research*, *234*, 104710.

[27] **Shao, Z.**, **Huq, M.E.**, **Cai, B.**, **Altan, O. and Li, Y.** (2020). Integrated remote sensing and GIS approach using Fuzzy-AHP to delineate and identify groundwater potential zones in semi-arid Shanxi Province, China, *Environmental Modelling & Software*, *134*, 104868.

[28] **Querales, M.**, **Salas, R.**, **Morales, Y.**, **Allende-Cid, H. and Rosas, H.** (2022). A stacking neuro-fuzzy framework to forecast runoff from distributed meteorological stations, *Applied Soft Computing*, *118*, 108535.

[29] **Semeraro, T.**, **Mastroleo, G.**, **Pomes, A.**, **Luvisi, A.**, **Gissi, E. and Aretano, R.** (2019). Modelling fuzzy combination of remote sensing vegetation index for durum wheat crop analysis, *Computers and Electronics in Agriculture*, *156*, 684–692.

[30] **Cai, C.**, **Wang, J. and Li, Z.** (2019). Assessment and modelling of uncertainty in precipitation forecasts from TIGGE using fuzzy probability and Bayesian theory, *Journal of Hydrology*, *577*, 123995.

[31] **Chang, C.**, **Lo, S. and Yu, S.** (2005). Applying fuzzy theory and genetic algorithm to interpolate precipitation, *Journal of Hydrology*, *314*(1-4), 92–104.

[32] **Foody, G.M.** (1996). Approaches for the production and evaluation of fuzzy land cover classifications from remotely-sensed data, *International Journal of Remote Sensing*, *17*(7), 1317–1340.

[33] **Xu, J.**, **Feng, G.**, **Zhao, T.**, **Sun, X. and Zhu, M.** (2019). Remote sensing image classification based on semi-supervised adaptive interval type-2 fuzzy c-means algorithm, *Computers & geosciences*, *131*, 132–143.

[34] **Xing, H.**, **He, H.**, **Hu, D.**, **Jiang, T. and Yu, X.** (2019). An interval Type-2 fuzzy sets generation method for remote sensing imagery classification, *Computers & Geosciences*, *133*, 104287.

[35] **Balcıoğlu, E.B. and Öztürk, B.** (2009). Oil pollution in the surface water of Sakarya RiverSakarya Nehri yüzey suyu petrol kirliliği, *Journal of Black Sea/Mediterranean Environment*, *15*(2), 99–108.

[36] **Solak, C.N.**, **Peszek, Ł.**, **Yilmaz, E.**, **Ergül, H.A.**, **Kayal, M.**, **Ekmekçi, Fatih, ... and Ács, É.** (2020). Use of diatoms in monitoring the Sakarya river basin, Turkey, *Water*, *12*(3), 703.

[37] **Dündar, M.S. and Altundağ, H.** (2018). Determination of some major and trace elements in the lower Sakarya River water by ICP-MS., *Journal of Chemical Metrology*, *12*(2).

[38] **Kahya, E. and Kalaycı, S.** (2004). Trend analysis of streamflow in Turkey, *Journal of hydrology*, *289*(1-4), 128–144.

[39] **Partal, T.** (2010). Wavelet transform-based analysis of periodicities and trends of Sakarya basin (Turkey) streamflow data, *River Research and Applications*, *26*(6), 695–711.

[40] **Güner, H.T.**, **Köse, N. and Harley, G.L.** (2017). A 200-year reconstruction of Kocasu River (Sakarya River Basin, Turkey) streamflow derived from a tree-ring network, *International journal of biometeorology*, *61*(3), 427–437.

[41] **Kayan, G.** (2014). Sakarya ve Batı Karadeniz akarsu havzaları için taban akışı ayırma modeli. İstanbul Teknik Üniversitesi Fen Bilimleri Enstitüsü, İstanbul, *Fen Bilimleri Enstitüsü, Yüksek Lisans Tezi, s*, *113*.

[42] **ÇERİBAŞI, G. and DoĞan, E.** (2015). Trend analizi yöntemi kullanılarak Batı ve Doğu Karadeniz ile Sakarya havzası akım miktarlarının değerlendirilmesi, *Uluslararası Teknolojik Bilimler Dergisi*, *7*(2), 1–12.

[43] **Kale, M.** (2019). An investigation of the changing spatial distribution of precipitation in the Sakarya basin between 1940 and 2010, pp.254– 270.

[44] **Yaykiran, S.**, **Cuceloglu, G. and Ekdal, A.** (2019). Estimation of water budget components of the Sakarya River Basin by using the WEAP-PGM model, *Water*, *11*(2), 271.

[45] **Katsanos, D.**, **Retalis, A.**, **Tymvios, F. and Michaelides, S.** (2016). Analysis of precipitation extremes based on satellite (CHIRPS) and in situ dataset over Cyprus, *Natural Hazards*, *83*(1), 53–63.

[46] **Retalis, A.**, **Katsanos, D.**, **Tymvios, F. and Michaelides, S.** (2018). Validation of the first years of GPM operation over Cyprus, *Remote Sensing*, *10*(10), 1520.

[47] **Retalis, A.**, **Katsanos, D.**, **Tymvios, F. and Michaelides, S.** (2020). Comparison of GPM IMERG and TRMM 3B43 Products over Cyprus, *Remote Sensing*, *12*(19), 3212.

[48] **Papadavid, G.**, **Hadjimitsis, D.G.**, **Toulios, L. and Michaelides, S.** (2013). A modified SEBAL modeling approach for estimating crop evapotranspiration in semi-arid conditions, *Water resources management*, *27*(9), 3493–3506.

[49] **Mercan, H. and Özcan, O.** (2018). Total Water Storage in Small Islands Using Multi-satellite Products: The case of Cyprus, *Journal of the Indian Society of Remote Sensing*, *46*(11), 1815–1821.

[50] **Papadavid, G. and Hadjimitsis, D.G.** (2012). Adaptation of SEBAL for estimating groundnuts evapotranspiration, in Cyprus, *South-Eastern European Journal of Earth Observation and Geomatics*.

[51] **Landerer, F.W. and Swenson, S.** (2012). Accuracy of scaled GRACE terrestrial water storage estimates, *Water resources research*, *48*(4).

[52] **Scanlon, B.R.**, **Zhang, Z.**, **Save, H.**, **Wiese, D.N.**, **Landerer, F.W.**, **Long, Di, ... and Chen, J.** (2016). Global evaluation of new GRACE mascon products for hydrologic applications, *Water Resources Research*, *52*(12), 9412–9429.

[53] **Long, D.**, **Pan, Y.**, **Zhou, J.**, **Chen, Y.**, **Hou, X.**, **Hong, Yang, ... and Longuevergne, L.** (2017). Global analysis of spatiotemporal variability in merged total water storage changes using multiple GRACE products and global hydrological models, *Remote Sensing of Environment*, *192*, 198–216.

[54] **Bhanja, S.N.**, **Mukherjee, A. and Rodell, M.** (2020). Groundwater storage change detection from in situ and GRACE-based estimates in major river basins across India, *Hydrological Sciences Journal*, *65*(4), 650–659.

[55] **Uz, M.**, **Atman, K.G.**, **Akyilmaz, O.**, **Shum, C.**, **Keleş, M.**, **Ay, Tuğçe, ... and Mercan, H.** (2022). Bridging the gap between GRACE and GRACE-FO missions with deep learning aided water storage simulations, *Science of The Total Environment*, *830*, 154701.

[56] **Mo, K.C. and Lettenmaier, D.P.** (2014). Objective drought classification using multiple land surface models, *Journal of Hydrometeorology*, *15*(3), 990–1010.

[57] **Massari, C.**, **Brocca, L.**, **Tarpanelli, A. and Moramarco, T.** (2015). Data assimilation of satellite soil moisture into rainfall-runoff modelling: A complex recipe?, *Remote Sensing*, *7*(9), 11403–11433.

[58] **Zhou, J.**, **Wu, Z.**, **He, H.**, **Wang, F.**, **Xu, Z. and Wu, X.** (2019). Regional assimilation of in situ observed soil moisture into the VIC model

considering spatial variability, *Hydrological Sciences Journal*, *64*(16), 1982–1996.

[59] **Chen, H.**, **Zhang, W. and Jafari Shalamzari, M.** (2019). Remote detection of human-induced evapotranspiration in a regional system experiencing increased anthropogenic demands and extreme climatic variability, *International Journal of Remote Sensing*, *40*(5-6), 1887–1908.

[60] **Xu, T.**, **Guo, Z.**, **Xia, Y.**, **Ferreira, V.G.**, **Liu, S.**, **Wang, Kaicun, ... and Zhao, C.** (2019). Evaluation of twelve evapotranspiration products from machine learning, remote sensing and land surface models over conterminous United States, *Journal of Hydrology*, *578*, 124105.

[61] **Liu, Y.**, **Mo, X.**, **Hu, S.**, **Chen, X. and Liu, S.** (2020). Assessment of human-induced evapotranspiration with GRACE satellites in the Ziya-Daqing Basins, China, *Hydrological Sciences Journal*, *65*(15), 2577–2589.

[62] **Liu, J.**, **Chai, L.**, **Dong, J.**, **Zheng, D.**, **Wigneron, J.P.**, **Liu, Shaomin, ... and Lu, Z.** (2021). Uncertainty analysis of eleven multisource soil moisture products in the third pole environment based on the three-corned hat method, *Remote Sensing of Environment*, *255*, 112225.

[63] **Agutu, N.**, **Ndehedehe, C.**, **Awange, J.**, **Kirimi, F. and Mwaniki, M.** (2021). Understanding uncertainty of model-reanalysis soil moisture within Greater Horn of Africa (1982–2014), *Journal of Hydrology*, *603*, 127169.

[64] **Yan, X.**, **Zhang, B.**, **Yao, Y.**, **Yang, Y.**, **Li, J. and Ran, Q.** (2021). GRACE and land surface models reveal severe drought in eastern China in 2019, *Journal of Hydrology*, *601*, 126640.

[65] **He, X.**, **Xu, T.**, **Xia, Y.**, **Bateni, S.M.**, **Guo, Z.**, **Liu, Shaomin, ... and Zhao, J.** (2020). A Bayesian Three-Cornered Hat (BTCH) method: improving the terrestrial evapotranspiration estimation, *Remote Sensing*, *12*(5), 878.

[66] **Zadeh, L.** (1965). Zadeh, Fuzzy sets, *Inform Control*, *8*, 338–353.

[67] **Liu, J.**, **Duan, Z.**, **Jiang, J.**, **Zhu, A.** *et al.* (2015). Evaluation of three satellite precipitation products TRMM 3B42, CMORPH, and PERSIANN over a subtropical watershed in China, *Advances in Meteorology*, *2015*.

[68] **Morales, Y.**, **Querales, M.**, **Rosas, H.**, **Allende-Cid, H. and Salas, R.** (2021). A self-identification Neuro-Fuzzy inference framework for modeling rainfall-runoff in a Chilean watershed, *Journal of Hydrology*, *594*, 125910.

[69] **Kayan, G.**, **Türker, U. and Erten, E.** (2022). Uncertainty quantification of multi-source hydrological data products for the improvement of water budget estimations in small-scale Sakarya basin, Turkey, *Hydrological Sciences Journal*, 1011–1025, https://doi.org/10.1080/02626667.2022.2093642, https://doi.org/10.1080/02626667.2022.2093642.

[70] **Payab, A.H. and Türker, U.** (2019). Comparison of standardized meteorological indices for drought monitoring at northern part of Cyprus, *Environmental Earth Sciences*, *78*(10), 1–19.

[71] **Kayan, G.**, **Riazi, A.**, **Erten, E. and Türker, U.** (2021). Peak unit discharge estimation based on ungauged watershed parameters, *Environmental Earth Sciences*, *80*(1), 1–10.

[72] **Payab, A.H. and Türker, U.** (2018). Analyzing temporal–spatial characteristics of drought events in the northern part of Cyprus, *Environment, Development and Sustainability*, *20*(4), 1553–1574.

[73] **Delhomme, J.P.** (1978). Kriging in the hydrosciences, *Advances in water resources*, *1*(5), 251–266.

[74] **Bargaoui, Z.K. and Chebbi, A.** (2009). Comparison of two kriging interpolation methods applied to spatiotemporal rainfall, *Journal of Hydrology*, *365*(1-2), 56–73.

[75] **Sorooshian, S.**, **Hsu, K.L.**, **Gao, X.**, **Gupta, H.V.**, **Imam, B. and Braithwaite, D.** (2000). Evaluation of PERSIANN system satellite-based estimates of tropical rainfall, *Bulletin of the American Meteorological Society*, *81*(9), 2035–2046.

[76] **Joyce, R.J.**, **Janowiak, J.E.**, **Arkin, P.A. and Xie, P.** (2004). CMORPH: A method that produces global precipitation estimates from passive microwave and infrared data at high spatial and temporal resolution, *Journal of hydrometeorology*, *5*(3), 487–503.

[77] **Huffman, G.J.**, **Bolvin, D.T.**, **Nelkin, E.J.**, **Wolff, D.B.**, **Adler, R.F.**, **Gu, Guojun, ... and Stocker, E.F.** (2007). The TRMM multisatellite precipitation analysis (TMPA): Quasi-global, multiyear, combined-sensor precipitation estimates at fine scales, *Journal of hydrometeorology*, *8*(1), 38–55.

[78] **Huffman, G.J.**, **Adler, R.F.**, **Bolvin, D.T.**, **Hsu, K.**, **Kidd, C.**, **Nelkin, Eric J, ... and Xie, P.** (2019). Algorithm Theoretical Basis Document (ATBD) for global precipitation climatology project version 3.0 precipitation data, *Greenbelt, MD: MEaSUREs project*.

[79] **Mu, Q.**, **Heinsch, F.A.**, **Zhao, M. and Running, S.W.** (2007). Development of a global evapotranspiration algorithm based on MODIS and global meteorology data, *Remote sensing of Environment*, *111*(4), 519–536.

[80] **Miralles, D.G.**, **Holmes, T.**, **De Jeu, R.**, **Gash, J.**, **Meesters, A. and Dolman, A.** (2011). Global land-surface evaporation estimated from satellite-based observations, *Hydrology and Earth System Sciences*, *15*(2), 453–469.

[81] **Zhang, K.**, **Kimball, J.S.**, **Nemani, R.R. and Running, S.W.** (2010). A continuous satellite-derived global record of land surface evapotranspiration from 1983 to 2006, *Water Resources Research*, *46*(9).

[82] **Rodell, M., Houser, P., Jambor, U., Gottschalck, J., Mitchell, K., Meng, C-J, ... and Toll, D.** (2004). The global land data assimilation system, *Bulletin of the American Meteorological society*, *85*(3), 381–394.

[83] **Liang, X., Lettenmaier, D.P., Wood, E.F. and Burges, S.J.** (1994). A simple hydrologically based model of land surface water and energy fluxes for general circulation models, *Journal of Geophysical Research: Atmospheres*, *99*(D7), 14415–14428.

[84] **Abatzoglou, J.T., Dobrowski, S.Z., Parks, S.A. and Hegewisch, K.C.** (2018). TerraClimate, a high-resolution global dataset of monthly climate and climatic water balance from 1958–2015, *Scientific data*, *5*(1), 1–12.

[85] **Watkins, M.M., Wiese, D.N., Yuan, D.N., Boening, C. and Landerer, F.W.** (2015). Improved methods for observing Earth's time variable mass distribution with GRACE using spherical cap mascons, *Journal of Geophysical Research: Solid Earth*, *120*(4), 2648–2671.

[86] **Ponce, V.M. and Hawkins, R.H.** (1996). Runoff curve number: Has it reached maturity?, *Journal of hydrologic engineering*, *1*(1), 11–19.

[87] **Hasan, E. and Tarhule, A.** (2020). GRACE: Gravity Recovery and Climate Experiment long-term trend investigation over the Nile River Basin: Spatial variability drivers, *Journal of Hydrology*, *586*, 124870.

[88] **Meyer, U., Sosnica, K., Arnold, D., Dahle, C., Thaller, D., Dach, R. and Jäggi, A.** (2019). SLR, GRACE and SWARM gravity field determination and combination, *Remote sensing*, *11*(8), 956.

[89] **Funk, C., Peterson, P., Landsfeld, M., Pedreros, D., Verdin, J., Shukla, Shraddhanand, ... and Michaelsen, J.** (2015). The climate hazards infrared precipitation with stations—a new environmental record for monitoring extremes, *Scientific data*, *2*(1), 1–21.

[90] **Kubota, T., Shige, S., Hashizume, H., Aonashi, K., Takahashi, N., Seto, Shinta, ... and Okamoto, K.I.** (2007). Global precipitation map using satellite-borne microwave radiometers by the GSMaP project: Production and validation, *IEEE Transactions on Geoscience and Remote Sensing*, *45*(7), 2259–2275.

[91] **Huffman, G.J., Bolvin, D.T., Braithwaite, D., Hsu, K., Joyce, R., Xie, P. and Yoo, S.H.** (2015). NASA global precipitation measurement (GPM) integrated multi-satellite retrievals for GPM (IMERG), *Algorithm Theoretical Basis Document (ATBD) Version*, *4*, 26.

[92] **Teutschbein, C. and Seibert, J.** (2012). Bias correction of regional climate model simulations for hydrological climate-change impact studies: Review and evaluation of different methods, *Journal of hydrology*, *456*, 12–29.

[93] **Shrestha, S.**, **Shrestha, M.**, **Babel, M.** *et al.* (2016). Modelling the potential impacts of climate change on hydrology and water resources in the Indrawati River Basin, Nepal, *Environmental Earth Sciences*, *75*(4), 1–13.

[94] **Premoli, A. and Tavella, P.** (1993). A revisited three-cornered hat method for estimating frequency standard instability, *IEEE Transactions on instrumentation and measurement*, *42*(1), 7–13.

[95] **He, X.**, **Xu, T.**, **Bateni, S.M.**, **Ek, M.**, **Liu, S. and Chen, F.** (2020). Mapping regional evapotranspiration in cloudy skies via variational assimilation of all-weather land surface temperature observations, *Journal of Hydrology*, *585*, 124790.

[96] **Galindo, F.J. and Palacio, J.** (1999). Estimating the instabilities of N correlated clocks, *Proceedings of the 31th Annual Precise Time and Time Interval Systems and Applications Meeting*, pp.285–296.

[97] **Di Baldassarre, G. and Montanari, A.** (2009). Uncertainty in river discharge observations: a quantitative analysis, *Hydrology and Earth System Sciences*, *13*(6), 913–921.

[98] **Kalman, R.E.** (1960). A new approach to linear filtering and prediction problems.

[99] **Gharibi, H.**, **Mahvi, A.H.**, **Nabizadeh, R.**, **Arabalibeik, H.**, **Yunesian, M. and Sowlat, M.H.** (2012). A novel approach in water quality assessment based on fuzzy logic, *Journal of Environmental Management*, *112*, 87–95.

[100] **Janarthanan, R.**, **Balamurali, R.**, **Annapoorani, A. and Vimala, V.** (2021). Prediction of rainfall using fuzzy logic, *Materials Today: Proceedings*, *37*, 959–963.

[101] **Wang, N.**, **Reformat, M.**, **Yao, W.**, **Zhao, Y. and Chen, X.** (2020). Fuzzy Linear regression based on approximate Bayesian computation, *Applied Soft Computing*, *97*, 106763.

[102] **Bárdossy, A.** (1996). The use of fuzzy rules for the description of elements of the hydrological cycle, *Ecological modelling*, *85*(1), 59–65.

[103] **Asai, H.**, **Tanaka, S. and Uegima, K.** (1982). Linear regression analysis with fuzzy model, *IEEE Trans. Systems Man Cybern*, *12*, 903–907.

[104] **Hojati, M.**, **Bector, C. and Smimou, K.** (2005). A simple method for computation of fuzzy linear regression, *European Journal of Operational Research*, *166*(1), 172–184.

[105] **Zeng, W.**, **Feng, Q. and Li, J.** (2017). Fuzzy least absolute linear regression, *Applied Soft Computing*, *52*, 1009–1019.

[106] **Verma, S.**, **Singh, P.**, **Mishra, S.**, **Singh, V.**, **Singh, V. and Singh, A.** (2020). Activation soil moisture accounting (ASMA) for runoff estimation using soil conservation service curve number (SCS-CN) method, *Journal of Hydrology*, *589*, 125114.

[107] **Yumnam, K.**, **Guntu, R.K.**, **Rathinasamy, M. and Agarwal, A.** (2022). Quantile-based Bayesian Model Averaging approach towards merging of precipitation products, *Journal of Hydrology*, *604*, 127206.

[108] **Willmott, C.J. and Matsuura, K.** (2005). Advantages of the mean absolute error (MAE) over the root mean square error (RMSE) in assessing average model performance, *Climate research*, *30*(1), 79–82.

[109] **Milewski, A.**, **Elkadiri, R. and Durham, M.** (2015). Assessment and comparison of TMPA satellite precipitation products in varying climatic and topographic regimes in Morocco, *Remote Sensing*, *7*(5), 5697–5717.

[110] **Ochoa, A.**, **Pineda, L.**, **Crespo, P. and Willems, P.** (2014). Evaluation of TRMM 3B42 precipitation estimates and WRF retrospective precipitation simulation over the Pacific–Andean region of Ecuador and Peru, *Hydrology and Earth System Sciences*, *18*(8), 3179–3193.

[111] **Mohd Zad, S.N.**, **Zulkafli, Z. and Muharram, F.M.** (2018). Satellite rainfall (TRMM 3B42-V7) performance assessment and adjustment over Pahang River Basin, Malaysia, *Remote sensing*, *10*(3), 388.

[112] **Guo, R. and Liu, Y.** (2016). Evaluation of satellite precipitation products with rain gauge data at different scales: Implications for hydrological applications, *Water*, *8*(7), 281.

[113] **Hu, Q.**, **Yang, D.**, **Li, Z.**, **Mishra, A.K.**, **Wang, Y. and Yang, H.** (2014). Multi-scale evaluation of six high-resolution satellite monthly rainfall estimates over a humid region in China with dense rain gauges, *International Journal of Remote Sensing*, *35*(4), 1272–1294.

[114] **Zhao, Y.**, **Lu, Z. and Wei, Y.** (2019). An assessment of global precipitation and evapotranspiration products for regional applications, *Remote Sensing*, *11*(9), 1077.

[115] **Satgé, F.**, **Hussain, Y.**, **Bonnet, M.P.**, **Hussain, B.M.**, **Martinez-Carvajal, H.**, **Akhter, G. and Uagoda, R.** (2018). Benefits of the successive GPM based satellite precipitation estimates IMERG–V03,–V04,–V05 and GSMaP–V06,–V07 over diverse geomorphic and meteorological regions of Pakistan, *Remote Sensing*, *10*(9), 1373.

[116] **Li, X.**, **Chen, S.**, **Liang, Z.**, **Huang, C.**, **Li, Z. and Hu, B.** (2021). Performance assessment of GSMaP and GPM IMERG products during Typhoon Mangkhut, *Atmosphere*, *12*(2), 134.

[117] **Liu, C.Y.**, **Aryastana, P.**, **Liu, G.R. and Huang, W.R.** (2020). Assessment of satellite precipitation product estimates over Bali Island, *Atmospheric Research*, *244*, 105032.

[118] **Ahamed, A.**, **Knight, R.**, **Alam, S.**, **Pauloo, R. and Melton, F.** (2022). Assessing the utility of remote sensing data to accurately estimate changes in groundwater storage, *Science of The Total Environment*, *807*, 150635.

[119] **Spellman, P.**, **Pritt, A. and Salazar, N.** (2021). Tracking changing water budgets across the Bahamian archipelago, *Journal of Hydrology*, *598*, 126178.

[120] **Hu, F.**, **Wei, Z.**, **Yang, X.**, **Xie, W.**, **Li, Y.**, **Cui, Changlu, ... and Meng, L.** (2022). Assessment of SMAP and SMOS soil moisture products using triple collocation method over Inner Mongolia, *Journal of Hydrology: Regional Studies*, *40*, 101027.

[121] **Li, C.**, **Tang, G. and Hong, Y.** (2018). Cross-evaluation of ground-based, multi-satellite and reanalysis precipitation products: Applicability of the Triple Collocation method across Mainland China, *Journal of Hydrology*, *562*, 71–83.

[122] **Khan, M.S.**, **Liaqat, U.W.**, **Baik, J. and Choi, M.** (2018). Stand-alone uncertainty characterization of GLEAM, GLDAS and MOD16 evapotranspiration products using an extended triple collocation approach, *Agricultural and Forest Meteorology*, *252*, 256–268.

[123] **Sjoberg, J.P.**, **Anthes, R.A. and Rieckh, T.** (2021). The three-cornered hat method for estimating error variances of three or more atmospheric datasets. Part I: overview and evaluation, *Journal of Atmospheric and Oceanic Technology*, *38*(3), 555–572.

[124] **Gruber, A.**, **Su, C.H.**, **Zwieback, S.**, **Crow, W.**, **Dorigo, W. and Wagner, W.** (2016). Recent advances in (soil moisture) triple collocation analysis, *International Journal of Applied Earth Observation and Geoinformation*, *45*, 200–211.

[125] **Loew, A. and Schlenz, F.** (2011). A dynamic approach for evaluating coarse scale satellite soil moisture products, *Hydrology and Earth System Sciences*, *15*(1), 75–90.

[126] **Save, H.**, **Bettadpur, S. and Tapley, B.D.** (2016). High-resolution CSR GRACE RL05 mascons, *Journal of Geophysical Research: Solid Earth*, *121*(10), 7547–7569.

APPENDICES

APPENDIX A : Datasets
APPENDIX B : Monthly and annual time series of WB components averaged over the Sakarya and Cyprus basins

APPENDIX A : Datasets

Appendix A.1. *Precipitation*

Appendix A.1.1. *PERSIANN*

PERSIANN was developed by the University of California. It uses infrared (IR) brightness temperature estimates from global geostationary satellites as the primary source of *P*. These estimates are then calibrated against low-orbit satellites using an artificial neural network [75]. PERSIANN provides monthly *P* at a spatial resolution of 0.25° with a quasi-global overage of 60°S-60°N. The data is available at https://chrsdata.eng.uci.edu/.

Appendix A.1.2. *CMORPH*

CMORPH, developed by the National Oceanic and Atmospheric Administration (NOAA) Climate Prediction Center (CPC), uses microwave (MW) data from low orbit satellites to derive *P* [76]. Then, it merges the retrieval accuracy of MW data with IR data which presents higher temporal resolution. We used monthly CMORPH V1 estimates with a spatial resolution of 0.5°. The data can be downloaded from the website https://climexp.knmi.nl/select.cgi?field=cmorph_monthly.

Appendix A.1.3. *TRMM*

TRMM, launched in 1997, was initially designed to monitor tropical and subtropical rainfall [77]. The TRMM dataset was created by blending the passive MW data from low earth orbit satellites with IR data collected by geostationary satellites. TRMM provides estimations with a high temporal resolution, including three hourly, daily, and monthly. In this study, TRMM-3B42RT V7 was used, with a spatial resolution of 0.25° at monthly time scale. It is available at https://giovanni.gsfc.nasa.gov.

Appendix A.1.4. *GPCP*

GPCP, a global dataset with a spatial resolution of 0.5° and monthly temporal resolution, consists of three inputs: MW, IR, and in-situ observations [78]. GPCP V3 was selected for this study. The dataset is freely available on the website https://disc.gsfc.nasa.gov/.

Appendix A.1.5. *CHIRPS*

CHIRPS product was initially created by the United States Geological Survey (USGS) and Climate Hazards Group (CHG) for trend analysis and drought monitoring with a quasi-global coverage (50°S-50°N, 180°E-180°W). CHIRPS combines *P* data estimates from high-resolution infrared cold cloud duration (CCD) calibrated using TRMM and in-situ observations [89]. 0.05° annual CHIRPS V2.0 estimates were chosen for this study, downloaded from the University of California, Santa Barbara (USA) website https://www.chc.ucsb.edu/data/chirps.

Appendix A.1.6. *GSMaP*

GSMaP, developed by the Japan Science and Technology Agency, is a quasi-global (60°S-60°N, 180°E-180°W) *P* dataset with a spatial resolution of 0.1° [90]. GSMaP dataset was generated blending passive microwave (PMW) retrievals from low-Earth orbit satellite with infrared IR retrievals from geostationary-Earth orbit satellite. GSMaP data is available from 2000 to the near-present, and monthly estimations were acquired through the website ftp://rainmap:Niskur+1404@hokusai.eorc.jaxa.jp/.

Appendix A.1.7. *IMERG*

As the successor of the TRMM, Global Precipitation Measurement (GPM) mission was launched in 2014 [91]. The GPM has some significant improvements over TRMM. First, GPM has wider spatial coverage from 65°S to 65°N, whereas TRMM has coverage from 50°S to 50°N. Second, GPM can detect light and solid *P* more accurately with the help of high-frequency PMW sensors. The Integrated Multi-satellitE Retrievals for GPM (IMERG) V06, one of GPM's products, which has 0.1° spatial resolution and monthly temporal resolution, were used in this study. IMERG V06 data can be downloaded from the website https://disc.gsfc.nasa.gov/.

Appendix A.2. *Evapotranspiration*

Appendix A.2.1. *MODIS*

MODIS is based on the Penman-Monteith (PM) equation. The PM algorithm calculates the daily sum of evaporation from the wet soil and canopy surfaces, along with vegetation transpiration, to provide 8-day, monthly and annual solutions [79]. Monthly MODIS MOD16 estimations with a spatial resolution of 0.05° were used in this study. The data can be downloaded from the website https://modis.gsfc.nasa.gov/data/dataprod/mod16.php.

Appendix A.2.2. *GLEAM*

GLEAM is based on the Priestly-Taylor (PT) equation. GLEAM differentiates the terrestrial components of *ET* into the soil and open-water evaporation, snow sublimation, canopy transpiration, and interception losses [80]. All components, except interception losses, are calculated using the PT equation. Interception losses are computed using Gash analytical model. A monthly GLEAM V5.a dataset with a spatial resolution of 0.25° was used in this study. The product is available at https://www.gleam.eu/.

Appendix A.2.3. *NTSG*

NTSG combines both PM and PT approaches [81]. Soil evaporation and canopy transpiration is calculated using the PM algorithm. The stomatal conductance required for the PM equation is derived from the satellite-based normalized difference vegetation index (NDVI). On the other hand, open-water evaporation is quantified using the PT equation. NTSG product provides monthly *ET* solutions with a spatial resolution of 8 km. The data was obtained from the https://www.ntsg.umt.edu/project/global-et.php.

Appendix A.2.4. *NOAH*

NOAH simulates *ET* using a PM approach by forcing with the Global Land Data Assimilation System (GLDAS) [82]. GLDAS NOAH V2.1 with a spatial resolution of 0.25° and temporal resolution of monthly was used in this study. The data was obtained from the https://disc.sci.gsfc.nasa.gov/.

Appendix A.2.5. *VIC*

GLDAS VIC was simulated using the VIC LSM. VIC is a semi-distributed, physically-based, macro-scale LSM that solves water and surface energy balances to estimate the *ET* [83]. GLDAS VIC provides global *ET* on 3-hour and monthly temporal scales. GLDAS VIC V2.1 was used in this study. The spatial and temporal resolution of the dataset is 1° and monthly, respectively, and available on the website https://disc.sci.gsfc.nasa.gov/.

Appendix A.2.6. *TERRACLIMATE*

TERRACLIMATE utilizes the Thornthwaite-Mather climatic water-balance model to estimate monthly *ET* from 1958-2015 [84]. It makes the assumption that there is a reference grass surface everywhere across the earth. TERRACLIMATE provides the global ET at 0.05° spatial resolution and monthly temporal resolution. The data is available at https://earlywarning.usgs.gov/fews/product/460.

Appendix A.3. *Terrestrial water storage change*

Appendix A.3.1. *JPL MASCON*

Since the launch of the mission in March 2002, GRACE data have been widely used to estimate monthly global ΔS, including groundwater, soil moisture content, surface water, and ice, by monitoring the distance between twin satellites. GRACE data mainly consist of two solutions obtained from three research centers (Jet Propulsion Laboratory (JPL), Center for Space Research at University of Texas (CSR), Geoforschungs Zentrum Potsdam (GFZ)): spherical harmonics (SH) and MASCON. The SH solutions, which were the backbone of the GRACE observations during the first decade of the GRACE mission, utilize global spherical harmonics to map Earth's gravity field. The MASCON solutions are more recent form of GRACE produced by using regional MASCON functions [85,126]. The key advantages to MASCON solutions over SH solutions are that MASCON solutions have lower leakage errors, and they need fewer post-processing filters. In addition, they provide better spatial resolution images compared to SH solutions. GRACE data has been missing for some months due to battery issues, and its mission was completed in June 2017. After the great success of the GRACE mission, GRACE Follow-On (GRACE-FO) has been in operation since May 2018. In this study, monthly JPL MASCON RL06_v02 solutions downloaded from https://grace.jpl.nasa.gov, with a spatial resolution of 0.5°×0.5°, were used.

APPENDIX B : Monthly and annual time series of WB components averaged over the Sakarya and Cyprus basins

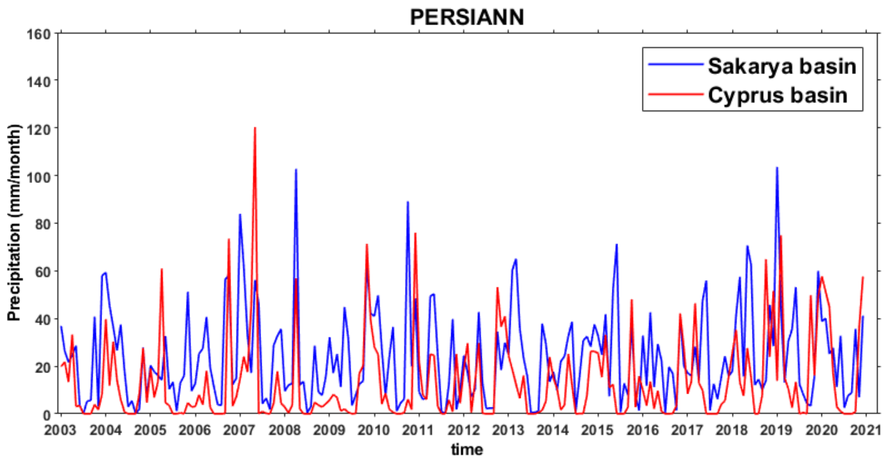

Figure B.1 : Monthly PERSIANN *P* time series over the Sakarya and Cyprus basins.

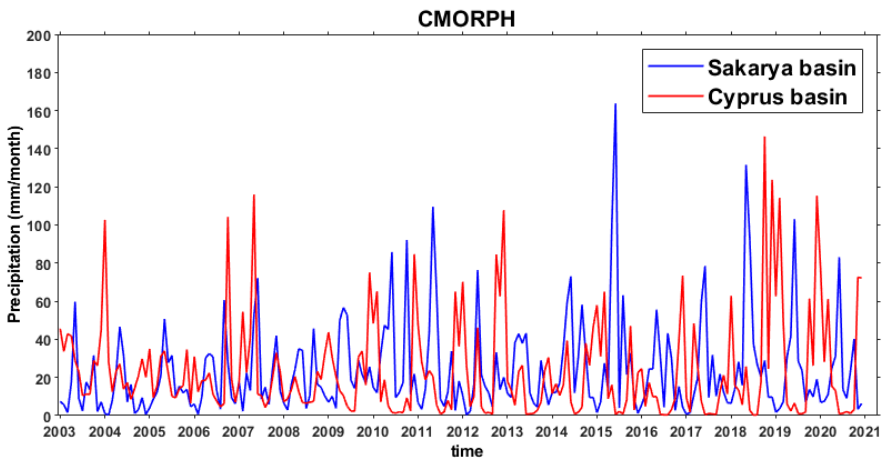

Figure B.2 : Monthly CMORPH *P* time series over the Sakarya and Cyprus basins.

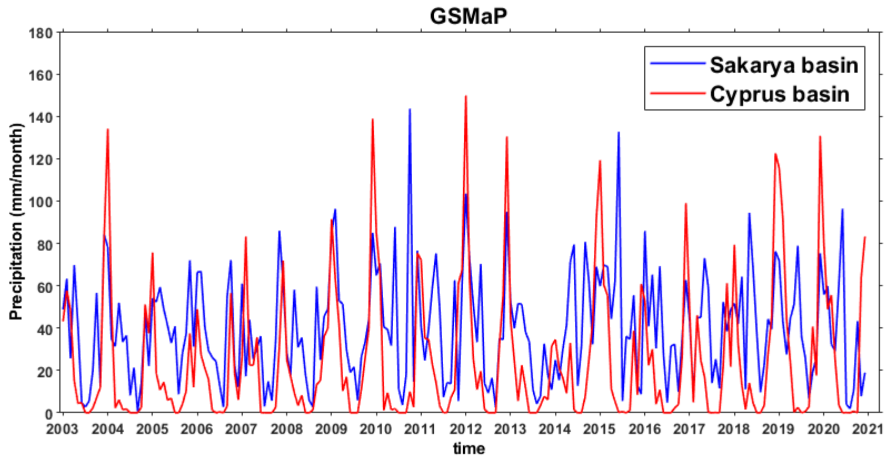

Figure B.3 : Monthly GSMaP P time series over the Sakarya and Cyprus basins.

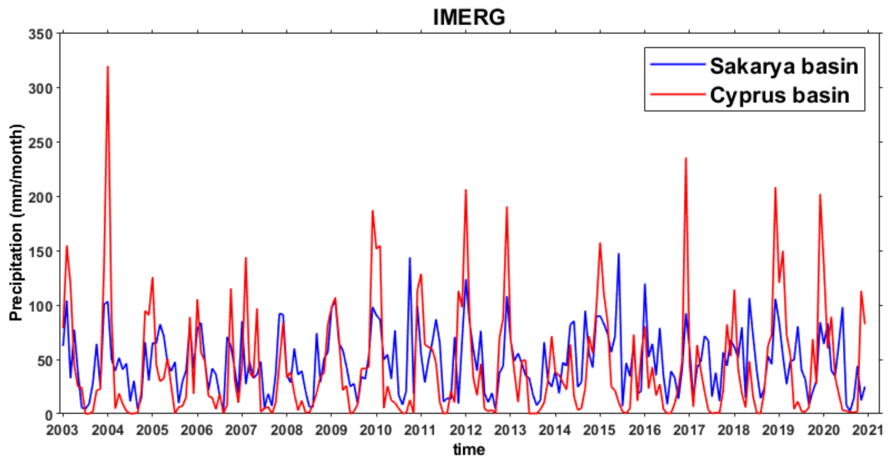

Figure B.4 : Monthly IMERG P time series over the Sakarya and Cyprus basins.

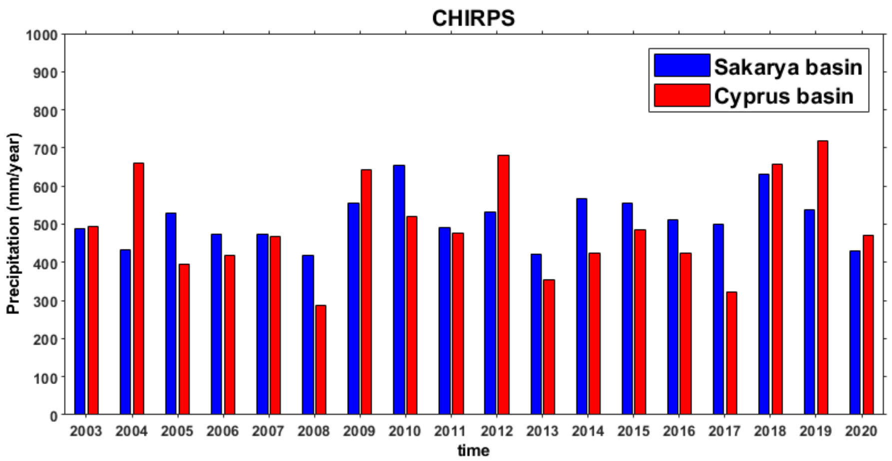

Figure B.5 : Annual CHIRPS P time series over the Sakarya and Cyprus basins.

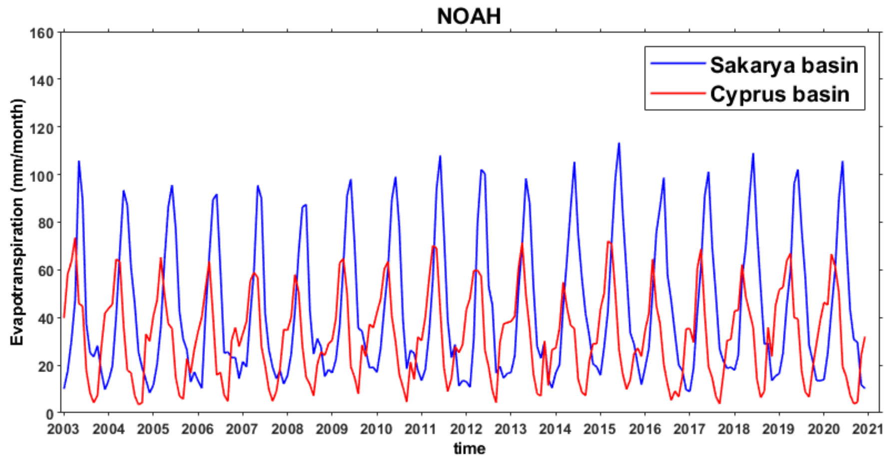

Figure B.6 : Monthly NOAH ET time series over the Sakarya and Cyprus basins.

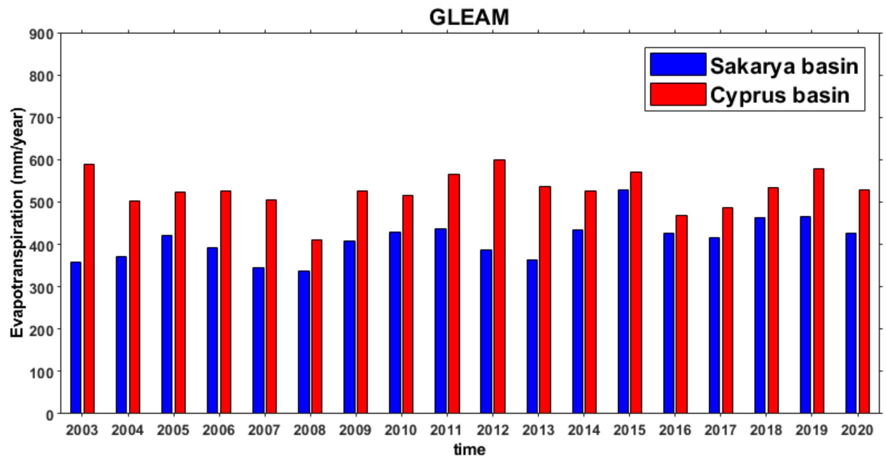

Figure B.7 : Annual GLEAM ET time series over the Sakarya and Cyprus basins.

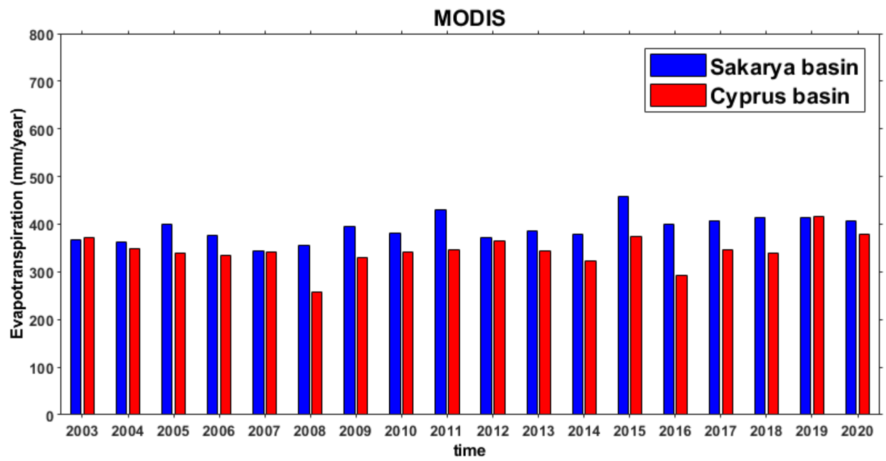

Figure B.8 : Annual MODIS ET time series over the Sakarya and Cyprus basins.

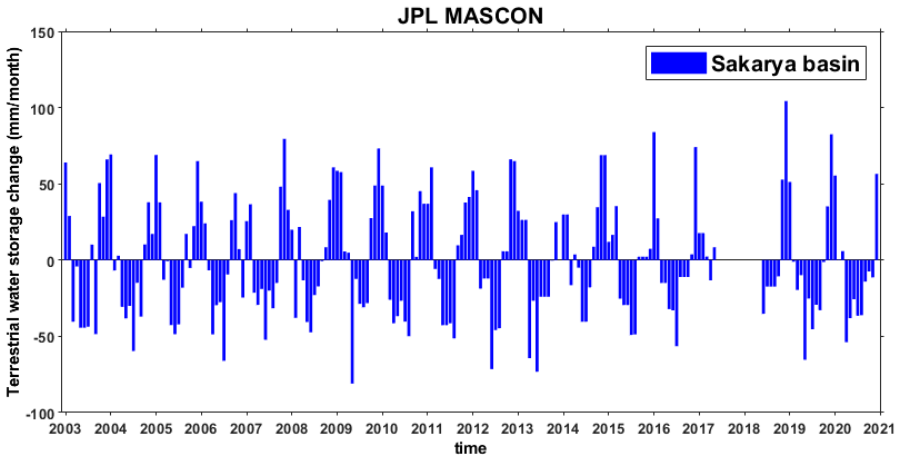

Figure B.9 : Monthly JPL MASCON ΔS time series over the Sakarya basin.

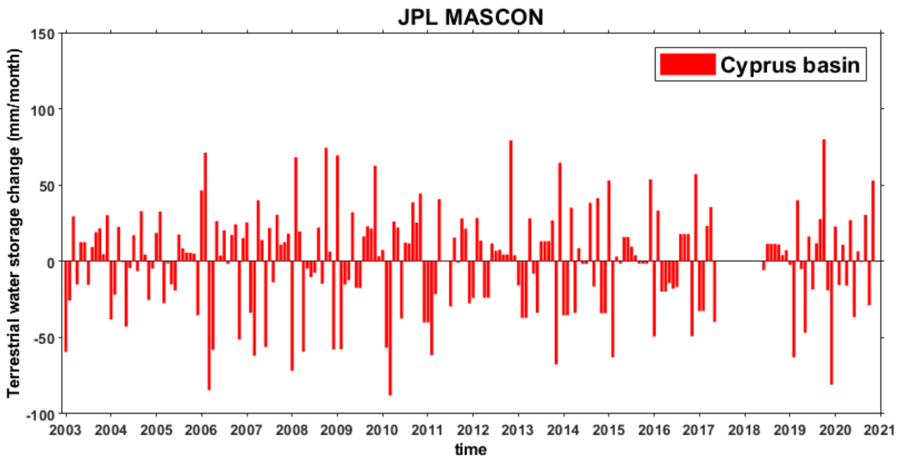

Figure B.10 : Monthly JPL MASCON ΔS time series over the Cyprus basin.

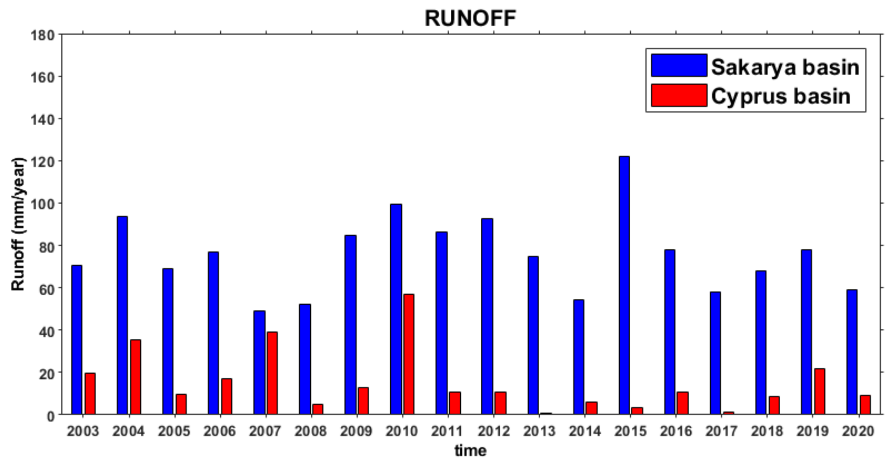

Figure B.11 : Annual Q time series over the Sakarya and Cyprus basins.

CURRICULUM VITAE

Name SURNAME: Gökhan KAYAN

EDUCATION:

- **B.Sc.:** 2012, Istanbul Technical University, Faculty of Civil Engineering, Department of Civil Engineering
- **M.Sc.:** 2015, Istanbul Technical University, Faculty of Civil Engineering, Hydraulic and Water Resources Engineering Programme

PUBLICATIONS, PRESENTATIONS AND PATENTS ON THE THESIS:

- **Kayan G.**, Erten, E., Mercan, H., Ozcan, O. (2017). Understanding of Cyprus total water storage under climate change. In 2017 *IEEE international geoscience and remote sensing symposium (IGARSS)*(pp. 5591-5594). IEEE. (Conference Paper)
- **Kayan G.**, Riazi, A., Erten, E., Türker, U. (2021). Peak unit discharge estimation based on ungauged watershed parameters. *Environmental Earth Sciences*, 80(1), 1-10. (Article)
- **Kayan G.**, Türker, U., Erten, E. (2022). Uncertainty quantification of multi-source hydrological data products for the improvement of water budget estimations in small-scale Sakarya basin, Turkey. *Hydrological Sciences Journal*, DOI: 10.1080/02626667.2022.2093642. (Article)
- **Kayan G.**, Türker, U., Erten, E. (2022). A fuzzy logic framework to handle uncertainty in remote sensing-based hydrological data for water budget improvement across mid- and small-scale basins. *Hydrological Processes*, HYP-22-0013. (Article-Under Review)